Periodically, quasiperiodically, and randomly driven conformal field theories

Xueda Wen,[1] Ruihua Fan,[2] Ashvin Vishwanath,[2] and Yingfei Gu[2]
[1]Department of Physics, Massachusetts Institute of Technology, Cambridge, Massachusetts 02139, USA
[2]Department of Physics, Harvard University, Cambridge, Massachusetts 02138, USA

(Received 28 June 2020; revised 18 January 2021; accepted 22 January 2021; published 14 April 2021)

In this paper and its upcoming sequel, we study nonequilibrium dynamics in driven $(1+1)$-dimensional conformal field theories (CFTs) with periodic, quasiperiodic, and random driving. We study a soluble family of drives in which the Hamiltonian only involves the energy-momentum density spatially modulated at a single wavelength. The resulting time evolution is then captured by a Möbius coordinate transformation. In this paper, we establish the general framework and focus on the first two classes. In periodically driven CFTs, we generalize earlier work and study the generic features of entanglement and energy evolution in different phases, i.e., the heating and nonheating phases and the phase transition between them. In quasiperiodically driven CFTs, we mainly focus on the case of driving with a Fibonacci sequence. We find that (i) the nonheating phases form a Cantor set of measure zero; (ii) in the heating phase, the Lyapunov exponents (which characterize the growth rate of the entanglement entropy and energy) exhibit self-similarity, and can be arbitrarily small; (iii) the heating phase exhibits periodicity in the location of spatial structures at the Fibonacci times; (iv) one can find exactly the nonheating fixed point, where the entanglement entropy and energy oscillate at the Fibonacci numbers, but grow logarithmically and polynomially at the non-Fibonacci numbers; (v) for certain choices of driving Hamiltonians, the nonheating phases of the Fibonacci driving CFT can be mapped to the energy spectrum of electrons propagating in a Fibonacci quasicrystal. In addition, another quasiperiodically driven CFT with an Aubry-André–type sequence is also studied. We compare the CFT results to lattice calculations and find remarkable agreement.

DOI: 10.1103/PhysRevResearch.3.023044

I. INTRODUCTION

Nonequilibrium dynamics in time-dependent driven quantum many-body systems has received extensive recent attention. A time-dependent drive, such as a periodic drive, creates a new stage in the search for novel systems that may not have an equilibrium analog, e.g., Floquet topological phases [1–14] and time crystals [15–23]. It is also one of the basic protocols to study nonequilibrium phenomena, such as localization-thermalization transitions, prethermalization, dynamical localization, dynamical Casimir effect, etc. [24–36].

Despite the rich phenomena and applications in the time-dependent driving physics, exactly solvable setups are, in general, very rare. Usually, we have to resort to numerical methods limited to small system size. In this work, we are interested in a quantum $(1+1)$-dimensional [$(1+1)$D] conformal field theory (CFT), which may be viewed as the low-energy effective field theory of a many-body system at the critical point. The property of conformal invariance at the critical point can be exploited to constrain the operator content of the critical theory [37,38]. In particular, for $(1+1)$D CFTs, the conformal symmetry is enlarged to the full Virasoro symmetry, which makes tractable the study of nonequilibrium dynamics, such as the quantum quench problems [39,40]. For a time-dependent driven CFT, however, relatively little is known.

Most recently, an analytically solvable setup on the periodically driven CFT was proposed in Ref. [41]. The authors implement the periodic driving with two noncommuting Hamiltonians H_0 and H_1 for time durations T_0 and T_1, respectively, where $H_0 = \int_0^L h(x)\,dx$ is the uniform CFT Hamiltonian on a line of length L, and H_1 is obtained from H_0 by deforming the Hamiltonian density $h(x)$ as $H_1(x) = \int_0^L 2\sin^2\frac{\pi x}{L}\,h(x)dx$, which is also called sine-square deformation (SSD) in literature [42–55]. Interestingly, it was found that different phases can emerge during the driving, depending on duration of the two time evolutions. As depicted in Fig. 1, there exits a heating phase with the entanglement entropy growing linearly in time, and a nonheating phase with the entanglement entropy simply oscillating in time. At the phase transition, the entanglement entropy grows logarithmically in time. Later in Ref. [56], these emergent phases and the phase diagram were further confirmed by studying how the system absorbs energy. More explicitly, the total energy of the system grows exponentially in time in the heating phase, oscillates in the nonheating phase, and grows polynomially at the phase transition. Furthermore, the system develops interesting

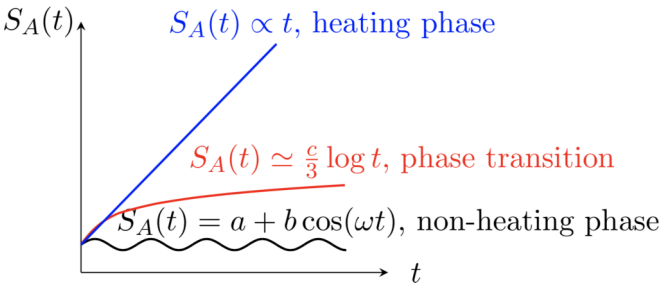

FIG. 1. Typical features of the time evolution of entanglement entropy in different phases of a periodically driven CFT. The entanglement entropy grows linearly in time in the heating phase, grows logarithmically at the phase transition, and simply oscillates in the nonheating phase.

spatial structures in the heating phase. The energy density forms an array of peaks[1] with simple patterns of entanglement as shown in Fig. 2.

In this work and its upcoming sequel, we introduce and study a general class of soluble models of driven CFTs with a variety of driving protocols. We determine their dynamical phase diagrams of heating versus nonheating behavior, particularly when the periodicity of the drive is absent. We extend the previous study on periodic driving to quasiperiodic[2] and random drivings, and make a connection to the familiar concepts of crystal, quasicrystal, and disordered systems. The connection is based on the coincidence of the group structures underlying the two problems:

(1) The driving protocol we considered for the CFTs involves SL_2 deformed Hamiltonians. These are generalizations of the SSD Hamiltonian protocols, where the deformed Hamiltonians H_q are chosen as $H_q = \int_0^L [f_q(x)\, h(x) + g_q(x)\, p(x)]dx$. Here $h(x)$ and $p(x)$ are the energy and momentum densities, and $f_q(x)$ $[g_q(x)]$ are real functions of the form $a + b\cos\frac{2\pi qx}{L} + c\sin\frac{2\pi qx}{L}$, with $q \in \mathbb{Z}$. The remarkable aspect of these protocols, which is the key to their solubility, is that the time evolution of many physical quantities after a prescribed time is captured simply by a 2×2 matrix transformation, i.e., a SL_2 or Möbius transformation. This simplification occurs despite the fact that we are discussing a spatially extended system. In this case, the operator evolution can be recast into a sequence of Möbius transformations on a suitable Riemann surface (see Fig. 3)

$$z_n = (M_1 M_2 \ldots M_n)\, z, \quad M_j \in \mathrm{SU}(1,1). \tag{1}$$

(2) The hopping problem in tight-binding model can be solved using transfer matrix method, namely, reformulating the discrete Schrödinger equation $E\psi_j = [H\psi]_j = \psi_{j+1} + \psi_{j-1} + V_j\psi_j$ by product of the transfer matrices

$$\Psi_n = (T_n \ldots T_2 T_1)\Psi_0, \quad T_j = \begin{pmatrix} E - V_j & -1 \\ 1 & 0 \end{pmatrix} \in \mathrm{SL}(2,\mathbb{R}), \tag{2}$$

where $\Psi_n = (\psi_{n+1}, \psi_n)^T$ represents the corresponding wave function.

Both problems are now solved by analyzing products of $\mathrm{SU}(1,1) \simeq \mathrm{SL}(2,\mathbb{R})$ matrices, creating intriguing analogies. In fact, the main part of the paper is to dive into the analogies and examine whether the rich phenomena in solids can reassemble in the time domain.

Outline and main results of this paper

(i) In Sec. II we explain the details of the general setup of our study, which is a time-dependent driven $(1+1)$ CFT with arbitrary SL_2 deformations. As mentioned in the Introduction, the physical consequence of such driving is encoded in the product

$$\Pi_n = M_1 M_2 \ldots M_n, \quad \text{where} \quad M_j \in \mathrm{SU}(1,1) \tag{3}$$

of a sequence of $\mathrm{SU}(1,1)$ matrices that correspond to the driving steps.

(ii) In Sec. III, we introduce the main diagnostics of our driven CFT: the Lyapunov exponent and group walking. The former is a useful characterization to quantify the growth of Π_n with respect to the number of driving step n, i.e.,

$$\lambda_L := \lim_{n\to\infty} \frac{\log \|M_1 M_2 \ldots M_n\|}{n}, \tag{4}$$

where $\|\cdot\|$ is a matrix norm. Applying to our driven system, the Lyapunov exponent has the meaning of the heating rate and serves as a good "order parameter" in carving the phase diagram. For example, $\lambda_L > 0$ represents a heating phase, and we show that total energy of the system grows exponentially as $E(n) \propto e^{2\lambda_L \cdot n}$ and the entanglement entropy of the subsystem that includes the energy-momentum density peaks grows linearly in time as $S(n) \propto \lambda_L n$. One interesting universal phenomenon here is that the total energy and the entanglement are not distributed evenly in the system, instead the driven state will develop an array of peaks of energy-momentum density in the real space. This phenomenon has been reported in Ref. [56] for special setups; now we verify the universality in a larger class.

For $\lambda_L = 0$, the system is either in the nonheating phase where total energy and the entanglement entropy oscillate or at the phase transition where the total energy grows polynomially and the entanglement grows logarithmically.

The second diagnostic we introduce is the notion of group walking, which is particularly useful in analyzing and visualizing the details of the spatial structures. This tool is necessary in the cases such as quasiperiodic and random driving when we need to resort to the numerics to identify the universal features.

(iii) In Sec. IV, we study the properties of the periodic driving, providing criteria of the heating phase, nonheating phase, and the phase transition. We discuss the generic features in each phase. This section generalizes the minimal setup in Refs. [41,56], and also provides the necessary tools for the discussions in quasiperiodic driving where technically we approach the quasiperiodic limit via a family of periodic driving.

[1]See also Ref. [57] for a related study on the emergent spatial structure of the energy-momentum density.

[2]See also Refs. [58–60] for studies on quasiperiodically driven quantum systems.

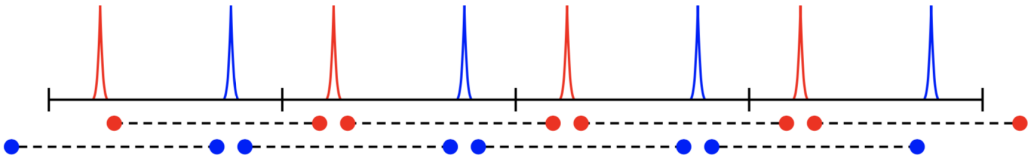

FIG. 2. A cartoon of the entanglement pattern and the energy-momentum density distribution in real space in the heating phase of a periodically driven CFT, where we drive the system with $H_0(x) = \int_0^L h(x)dx$ and $H_1(x) = \int_0^L 2\,\sin^2\frac{q\pi x}{L}\,h(x)\,dx$ with $q = 4$ here. Red and blue colors stand for two different chiralities. Each peak is entangled with its nearest neighbor with the same chirality and color. Periodic boundary conditions are assumed here.

(iv) In Sec. V, we consider the quasiperiodic driving using two examples: Fibonacci type and Aubry-André type. The Fibonacci driving is the main focus.

In the Fibonacci driving, we use the Fibonacci bit string or word (see Appendix B) $X_{j=1,2,3,\ldots} = 10110101\ldots$ and two distinct unitary operators $U_A = e^{-iH_AT_A}$, $U_B = e^{-iH_BT_B}$ to generate a quasiperiodic driving sequence $U_j = X_jU_A + (1 - X_j)U_B$. The simplest way to generate the Fibonacci bit string is through the following substitution rule: Begin with a single bit 1, and apply the substitution rule $1 \to 10$, $0 \to 1$ at each step, then we will generate the following sequence $1 \to 10 \to 101 \to 10110 \to 10110101 \to \ldots$, which approaches the Fibonacci bit string in the infinite step limit. Denoting the nth Fibonacci number as F_n, namely, $F_n = F_{n-1} + F_{n-2}$ with $F_0 = F_1 = 1$, the Fibonacci bit string or word satisfies $X_{j+F_n} = X_j$, where $n \geqslant 2$ and $1 \leqslant j < F_n$. In the Fibonacci driving, we find the following features:

(1) In the heating phase, the distribution of Lyapunov exponents (heating rates) exhibits self-similarity in the parameter space (see Fig. 19). This also implies there exist heating phases with arbitrarily small positive Lyapunov exponents. At these points, the growth of entanglement entropy and energy can be arbitrarily slow. In addition, there are very rich patterns in the time evolution of entanglement and energy in the heating phase. In particular, the locations of the energy-momentum density peaks exhibit even and odd effects at those driving steps that correspond to the Fibonacci numbers.

(2) Exact nonheating fixed points. We find that there always exist *exact* nonheating fixed points in the phase diagram, as long as both of the two driving Hamiltonians are elliptic [see the definition in Eq. (17)]. At the nonheating fixed point, the time evolution of the entanglement entropy and the total energy can be analytically obtained at the Fibonacci numbers F_n. They exhibit an oscillating feature of period 6, i.e., $S_A(F_n) = S_A(F_{n+6})$ and $E(F_n) = E(F_{n+6})$. At the driving steps that are not Fibonacci numbers, the envelope of the entanglement entropy grows logarithmically in time, and the total energy grows in a power law.

(3) We find an exact mapping between the phase diagram of a Fibonacci driving CFT and the energy spectrum of a Fibonacci quasicrystal. More precisely, the nonheating phase in the parameter space of a Fibonacci driving CFT corresponds to the energy spectrum of a Fibonacci quasicrystal. Both form a Cantor set of measure zero.

As a complement, we also investigate the quasiperiodic driving with an Aubry-André–type sequence, where the phase diagram has a nested structure that resembles the famous Hofstadter butterfly found in the Landau level problem [61]. We also examine the measure of the nonheating phase and show it vanishes similar to the Fibonacci driving.

(v) In Sec. VI we conclude with discussions. We also provide several appendices with details of calculations and examples.

II. TIME-DEPENDENT DRIVEN CFT WITH SL_2 DEFORMATIONS

In this section, we introduce the general setup and basic properties of a time-dependent driven CFT with SL_2 deformations. The formalism in this section is general, i.e., suitable for arbitrary driving sequence. In the end of this section, we will explain the three classes of driving that we will focus on in this paper and its upcoming sequel [62]: the periodically, quasiperiodically, and randomly driven CFTs as advertised in the Introduction. More technical details can be found in Appendix A (see also Refs. [41,48,56]).

We are mainly interested in the time-dependent driven CFT with discrete time steps. That is, we drive the CFT with H_1 for a time interval T_1, then with H_2 for a time interval T_2, and so on, where $H_{1,2,\ldots}$ are SL_2 deformed CFT Hamiltonians that we will explain momentarily. Starting from an initial state $|\Psi_0\rangle$, the wave function after n steps of driving has the form

$$|\Psi_n\rangle = U_n \ldots U_2U_1|\Psi_0\rangle, \quad \text{with} \quad U_j = e^{-iH_jT_j}. \tag{5}$$

The initial state here is not limited to a ground state. For instance, it can be chosen as a highly excited pure state or a thermal ensemble at finite temperature, as will be studied in detail in Ref. [63]. It is found that the emergent phase diagram of the time-dependent driven CFT is independent of the choices of the initial state, and only depends on the concrete protocols of driving, namely, the driving sequences $\{U_j\}$ here. For simplicity, throughout this work we will choose the initial state $|\Psi_0\rangle$ as the ground state of a "uniform CFT,"

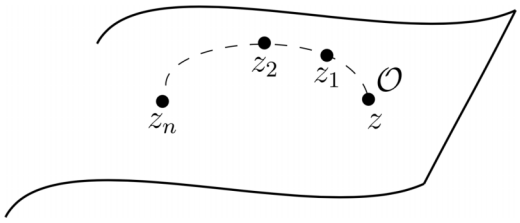

FIG. 3. A local view of the operator evolution on a Riemann surface. By choosing suitable coordinates, each step of the driving can be characterized by a Möbius transformation that is determined by the SL_2 deformed Hamiltonian.

i.e., with uniform Hamiltonian density

$$H_0 = \frac{1}{2\pi}\int_0^L [T(x) + \overline{T}(x)]dx, \tag{6}$$

where $T(x)$ $[\overline{T}(x)]$ are the chiral (antichrial) energy-momentum tensor with translation symmetry, L is the total length of the system.

Now let us specify the choices of the Hamiltonians $\{H_j\}$ in Eq. (5), we require them to be generated by a deformation $\{(f_j, g_j)\}$ as follows:

$$H_j = \frac{1}{2\pi}\int_0^L [f_j(x)\,T(x) + g_j(x)\overline{T}(x)]dx, \tag{7}$$

where $f_j(x)$ and $g_j(x)$ are two independent real functions with periodic boundary conditions.[3] That is to say, in general we can deform the chiral and antichiral modes independently in a system with periodic boundary conditions.

An alternative way to view the deformation in (7) is to rewrite (7) using energy density $T_{00}(x) = \frac{1}{2\pi}[T(x) + \overline{T}(x)]$ and the momentum density $T_{01}(x) = \frac{1}{2\pi}[T(x) - \overline{T}(x)]$ as follows:

$$H_j = \int_0^L \left[\frac{f_j(x) + g_j(x)}{2}T_{00}(x) + \frac{f_j(x) - g_j(x)}{2}T_{01}(x)\right]dx. \tag{8}$$

Although the formulas and results we obtain in the this work hold for the general case, in many places of this paper we will choose $f_j(x) = g_j(x)$ such that the deformed Hamiltonian takes the simple form

$$H_j = \int_0^L f_j(x)\,T_{00}(x)dx\,. \tag{9}$$

The study of the energy spectrum of such Hamiltonian can be found in [49]. In particular, the so-called sine-square deformation (SSD) with $f_j(x) = \sin^2(\frac{\pi x}{L})$ in Eq. (9) has received extensive study in both condensed matter physics and string theory recently [42–55]. In fact, the initial study of the Floquet CFT in Refs. [41,56] is also based on SSD.

A. SL_2 deformation

A convenient parametrization of the deformed Hamiltonian H_j in Eq. (7) is to use the Fourier components of $T(x)$ and $\overline{T}(x)$ denoted as L_n and $\overline{L}_n$:

$$L_n := \frac{c}{24}\delta_{n,0} + \frac{L}{2\pi}\int_0^L \frac{dx}{2\pi}\,e^{i\frac{2\pi n}{L}x}\,T(x)\,,$$
$$\overline{L}_n := \frac{c}{24}\delta_{n,0} + \frac{L}{2\pi}\int_0^L \frac{dx}{2\pi}\,e^{-i\frac{2\pi n}{L}x}\,\overline{T}(x)\,, \quad n \in \mathbb{Z}\,. \tag{10}$$

The operators L_n $(\overline{L}_n)$ form a Virasoro algebra

$$[L_m,\, L_n] = (m-n)L_{m+n} + \frac{c}{12}(m^3 - m)\delta_{m+n,0}, \quad n, m \in \mathbb{Z} \tag{11}$$

with c being the central charge of the underlying CFT. For example, the uniform Hamiltonian H_0 defined in (6) can be expressed as

$$H_0 = \frac{2\pi}{L}(L_0 + \overline{L}_0) - \frac{\pi c}{6L}, \tag{12}$$

and what we will call a "SL_2 deformed" Hamiltonian corresponds to the following enveloping function:

$$f_j(x) = \sigma_j^0 + \sigma_j^+\cos\frac{2\pi qx}{L} + \sigma_j^-\sin\frac{2\pi qx}{L},$$
$$\sigma_j^0, \sigma_j^+, \sigma_j^- \in \mathbb{R}, \quad q \in \mathbb{Z} \tag{13}$$

and similarly for $g_j(x)$. In this case, the corresponding H_j is a linear superposition of $\{L_0, L_{\pm q}\}$ and $\{\overline{L}_0, \overline{L}_{\pm q}\}$, which are the generators of the $SL^{(q)}(2,\mathbb{R})$ subgroup.[4] To be concrete, we have $H_j = H_{j,\text{chiral}} + H_{j,\text{antichrial}}$, with

$$H_{j,\text{chiral}} = \frac{2\pi}{L}\left(\sigma_j^0 L_0 + \sigma_j^+ L_{q,+} + \sigma_j^- L_{q,-}\right) - \frac{\pi c}{12L}, \tag{14}$$

where we have defined $L_{q,+} := \frac{1}{2}(L_q + L_{-q})$ and $L_{q,-} := \frac{1}{2i}(L_q - L_{-q})$. Note the SSD deformation mentioned above corresponds to the special case when

$$q = 1, \quad \sigma^0 = \tfrac{1}{2}, \quad \sigma^+ = -\tfrac{1}{2}, \quad \sigma^- = 0 \quad \text{(SSD)}. \tag{15}$$

Therefore, the SL_2 deformation can be thought as a generalization of the SSD deformation, while retaining the analytic tractability.[5]

In general, by defining the quadratic Casimir

$$c^{(2)} := -(\sigma^0)^2 + (\sigma^+)^2 + (\sigma^-)^2, \tag{16}$$

the (chiral and antichiral) SL_2 deformed Hamiltonians can be classified into three types as follows [45,46,65,66]:

$$c^{(2)} < 0: \quad \text{elliptic Hamiltonian},$$
$$c^{(2)} = 0: \quad \text{parabolic Hamiltonian}, \tag{17}$$
$$c^{(2)} > 0: \quad \text{hyperbolic Hamiltonian}.$$

Different types of Hamiltonians will determine the operator evolution in different ways (see Appendix A 1).

With the SL_2 deformation, many physical properties of the driven system including the phase diagram, the time dependence of the entanglement entropy [41,48], and the energy-momentum density [56,57] have been obtained in a *periodically* driven CFT system. Here we generalize the driving to an arbitrary sequence $\{U_j\}$ as shown in Eq. (5). In the following, we will derive general formulas based on the SL_2 deformation sequence, and later apply to the periodically, quasiperiodically, and randomly driven CFTs.

[3] One can of course choose open boundary conditions at the two ends. Then, $f_j(x)$ and $g_j(x)$ should satisfy the constraint $f_j(x)T(x) = g_j(x)\overline{T}(x)$ at $x = 0, L$, which implies that there is no momentum flow across the boundary. Since we already have $T(x) = \overline{T}(x)$ at $x = 0,\ L$ in the uniform case, this indicates $f_j(x) = g_j(x)$ at $x = 0,\ L$ in the case of open boundary conditions.

[4] More precisely, $SL^{(q)}(2,\mathbb{R})$ is isomorphic to a q-fold cover of $SL(2,\mathbb{R})$ (see, e.g., Ref. [64]).

[5] Solving the nonequilibrium dynamics with the most general deformations that correspond to the infinite-dimensional Virasoro algebra is more challenging and will not be discussed in this paper.

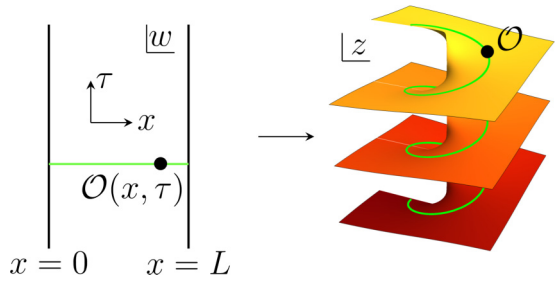

FIG. 4. Conformal map $z = e^{\frac{2\pi q w}{L}}$ from the w cylinder (where $w = \tau + ix$, and $x = L$ and 0 are identified) to the q-sheet Riemann surface z.

B. Operator evolution

For SL_2 driven quantum states, it is convenient to compute observables via Heisenberg picture, namely, the correlation functions are given by $\langle\Psi_0|\mathcal{O}_1(x_1,t_1)\ldots\mathcal{O}_n(x_n,t_n)|\Psi_0\rangle$, where the Heisenberg operators $\mathcal{O}(x,t)$ are defined by discrete time evolution

$$\mathcal{O}(x,t) := U^\dagger(t)O(x)U(t), \quad \text{with} \quad U(t) = U_m\ldots U_2U_1. \tag{18}$$

For each step, $U_j = e^{-iH_jT_j}$ is generated by the SL_2 deformed Hamiltonian and $t = \sum_{j=1}^m T_j$ is only defined for a discrete set of times in our setting.

The virtue of the driving Hamiltonian in (7) is that the operator evolution can be represented by a conformal mapping $(z,\bar z)\to(z',\bar z')$, under which the primary operator $\mathcal{O}(z,\bar z)$ transforms as

$$U_j^\dagger\,\mathcal{O}(z,\bar z)\,U_j = \left(\frac{\partial z'}{\partial z}\right)^h\left(\frac{\partial\bar z'}{\partial\bar z}\right)^{\bar h}\mathcal{O}(z',\bar z'), \tag{19}$$

where h ($\bar h$) are conformal dimensions of $\mathcal{O}$. Then, the full unitary $U(t)$ is a composition of a sequence of conformal mappings. For the special type of enveloping function (13), a convenient coordinate is given as follows (see Fig. 4 for an illustration):

$$z = \exp\frac{2\pi q w}{L}, \quad w = \tau + ix, \tag{20}$$

under which the evolution generated by U_j can be expressed as a Möbius transformation:[6]

$$z' = \frac{a_jz + b_j}{c_jz + d_j}, \quad \text{where} \underbrace{\begin{pmatrix} a_j & b_j \\ c_j & d_j\end{pmatrix}}_{\text{denoted as } M_j} \in \mathrm{SL}(2,\mathbb{C}). \tag{21}$$

The explicit form of M_j is determined by the Hamiltonian H_j and the time interval T_j. An important observation is that the driving protocol (13) we use in fact generates M_j matrix in the specific form

$$M_j = \begin{pmatrix} a_j & b_j \\ b_j^* & a_j^*\end{pmatrix} \quad \text{where} \quad a_j,\, b_j\in\mathbb{C}, \quad |a_j|^2 - |b_j|^2 = 1, \tag{22}$$

which is a SU(1, 1) matrix. Note $\mathrm{SU}(1,1)\cong\mathrm{SL}(2,\mathbb{R})$; both are subgroups of $\mathrm{SL}(2,\mathbb{C})$. The isomorphism is expected since we start from a $\mathrm{SL}(2,\mathbb{R})$ action on the states.

Thus, the net effect of the full evolution $U = U_n\ldots U_2U_1$ is given by the product of n SU(1, 1) matrices

$$\Pi_n = M_1\ldots M_{n-1}M_n = \begin{pmatrix} a_1 & b_1 \\ c_1 & d_1\end{pmatrix}\ldots \begin{pmatrix} a_{n-1} & b_{n-1} \\ c_{n-1} & d_{n-1}\end{pmatrix}\begin{pmatrix} a_n & b_n \\ c_n & d_n\end{pmatrix}. \tag{23}$$

Note that the later matrix acts on the right since we are using the Heisenberg picture of evolution. To summarize, the operator evolution under a sequence of driving $\{U_j\}$ is given by the formula

$$U_1^\dagger U_2^\dagger\ldots U_n^\dagger\,\mathcal{O}(z,\bar z)\,U_n\ldots U_2U_1 = \left(\frac{\partial z_n}{\partial z}\right)^h\left(\frac{\partial\bar z_n}{\partial\bar z}\right)^{\bar h}\mathcal{O}(z_n,\bar z_n), \tag{24}$$

where z_n is related to z through the Möbius transformation in (21) with the matrix $\Pi_n\in\mathrm{SU}(1,1)$:

$$\Pi_n = \begin{pmatrix} \alpha_n & \beta_n \\ \beta_n^* & \alpha_n^*\end{pmatrix} \quad \text{where} \quad \alpha_n,\,\beta_n\in\mathbb{C}, \quad |\alpha_n|^2 - |\beta_n|^2 = 1. \tag{25}$$

C. Time evolution of entanglement and energy-momentum density

To characterize the possible emergent phases, we study the time evolution of the entanglement entropy and the energy-momentum density of the system. In terms of correlation functions, the former is determined by the two-point function of twist operator, while the latter is determined by the one-point function of energy-momentum tensor. One can also consider two-point functions of general operators, which are discussed in Appendix A 2.

For example, the mth Renyi entropy of the subsystem $A = [x_1,\, x_2]$ can be obtained by the formula

$$S_A^{(m)}(n) = \frac{1}{1-m}\log\langle\Psi_n|\mathcal{T}_m(x_1)\overline{\mathcal{T}}_m(x_2)|\Psi_n\rangle, \tag{26}$$

where $|\Psi_n\rangle$ is the time-dependent wave function in Eq. (5), and $\mathcal{T}_m$ ($\overline{\mathcal{T}}_m$) are twist (antitwist) operators that are primary, with conformal dimensions $h = \bar h = \frac{c}{24}(m - \frac{1}{m})$. For initial state $|\Psi_0\rangle$ being the ground state of H_0 with periodic boundary conditions, the time evolution of the entanglement entropy for the subsystem $A = [(k-1/2)l, (k+1/2)l]$ where $k\in\mathbb{Z}$ and $l = L/q$ is given as[7]

$$S_A(n) - S_A(0) = \frac{c}{3}(\log|\alpha_n - \beta_n| + \log|\alpha_n' - \beta_n'|). \tag{27}$$

[6] More details can be found in Appendix A. See also Refs. [41,48,56].

[7] For a general choice of single-interval subsystem $A = [x_1,\, x_2]$, the exact expression of the entanglement entropy under a time-dependent driving will be quite involved. See, e.g., the Appendix of Ref. [41]. However, if the CFT is in a heating phase, one can obtain an approximated expression of the entanglement entropy of $A = [x_1,\, x_2]$ by keeping the leading order [56].

Here α_n and β_n are the matrix elements appearing in the operator evolution in Eq. (25). α'_n and β'_n are the corresponding matrix elements for the antichiral part.

One can also study the time evolution of energy-momentum tensors based on the operator evolution as discussed in the previous subsection. However, since $T(x)$ is not a primary field, the operator evolution in Eq. (19) should be modified as

$$U_j^\dagger T(z) U_j = \left(\frac{\partial z'}{\partial z}\right)^2 T(z') + \frac{c}{12}\mathrm{Sch}(z', z), \tag{28}$$

where the last term represents the Schwarzian derivative. The expectation value of the chiral energy-momentum tensor density is [56][8]

$$\frac{1}{2\pi}\langle T(x,n)\rangle = -\frac{q^2\pi c}{12L^2} + \frac{\pi c}{12L^2}(q^2-1) \times \frac{1}{|\alpha_n e^{\frac{2\pi i x}{l}} + \beta_n|^4}, \quad \text{where } l = L/q. \tag{29}$$

For the antichiral component $\frac{1}{2\pi}\langle \overline{T}(x,n)\rangle$, the expression is the same as above by replacing α_n $(\beta_n) \to \alpha'_n$ (β'_n) and $e^{\frac{2\pi i x}{l}} \to e^{-\frac{2\pi i x}{l}}$. The total energy and momentum of the system are $E(n) = \frac{1}{2\pi}\int_0^L \langle T(x,n) + \overline{T}(x,n)\rangle dx$ and $P(n) = \frac{1}{2\pi}\int_0^L \langle T(x,n) - \overline{T}(x,n)\rangle dx$, with the expressions

$$E(n) = -\frac{q^2\pi c}{6L} + \frac{\pi c}{12L}(q^2-1)(|\alpha_n|^2 + |\beta_n|^2 + |\alpha'_n|^2 + |\beta'_n|^2),$$
$$P(n) = \frac{\pi c}{12L}(q^2-1)(|\alpha_n|^2 + |\beta_n|^2 - |\alpha'_n|^2 - |\beta'_n|^2). \tag{30}$$

We would like to make a few remarks here:

(1) For the periodic boundary conditions we considered here, the time evolution with $q = 1$ deformations are trivial as H_j also annihilates the ground state of H_0.[9] In contrast, if we consider an open boundary condition, the ground state of H_0 will no longer be the eigenstate of the deformed Hamiltonian H_i. Then one can have a nontrivial time evolution, as studied in Refs. [41,56].

(2) If there is no driving, i.e., $\alpha_n = \alpha'_n = 1$ and $\beta_n = \beta'_n = 0$, one can find $E(n) = -\frac{\pi c}{6L}$, which is the Casimir energy with periodic boundary conditions.

(3) If we only deform the Hamiltonian density in Eq. (8), i.e., let $f_j(x) = g_j(x)$, one can find that $\alpha_n = \alpha'_n$ and $\beta_n = \beta'_n$ [41], and therefore $P(n) = 0$, i.e., the total momentum stays zero. In this case, both the left movers and right movers are excited, but they carry opposite momentum and the total momentum are canceled to be zero.

(4) In later sections, we will compare the CFT calculations with the lattice calculations. An efficient way to perform numerical calculations on the lattice is to consider $q = 1$ with an open boundary condition since for larger q, the length of the wavelength of deformation $l := L/q$ is effectively suppressed for a fixed L. In this case, by deforming the Hamiltonian in Eq. (9), where only the Hamiltonian density is deformed, one can find the time evolution of the entanglement entropy as follows [41]:

$$S_A(n) - S_A(0) = \frac{c}{3}\log|\alpha_n - \beta_n|, \quad \text{where} \quad A = [0, L/2]. \tag{31}$$

The expectation value of the chiral energy-momentum density is [56]

$$\frac{1}{2\pi}\langle T(x,n)\rangle = -\frac{\pi c}{12L^2} + \frac{\pi c}{16L^2}\frac{1}{|\alpha_n e^{\frac{2\pi x}{L}} + \beta_n|^4}. \tag{32}$$

The antichiral part has the same expression as above with the replacing $e^{\frac{2\pi i x}{L}} \to e^{\frac{-2\pi i x}{L}}$. Then one can find $\frac{1}{2\pi}\int_0^L \langle T(x,n)\rangle = \frac{1}{2\pi}\int_0^L \langle \overline{T}(x,n)\rangle = -\frac{\pi c}{12L} + \frac{\pi c}{16L}(|\alpha_n|^2 + |\beta_n|^2)$, based on which one can obtain the total energy as

$$E(n) = \frac{\pi c}{8L}(|\alpha_n|^2 + |\beta_n|^2) - \frac{\pi c}{6L}. \tag{33}$$

One can find the similarity and difference by comparing with the case with periodic boundary conditions. For example, in the ground state with $\alpha_n = 1$, $\beta_n = 0$ in (33), one can obtain the Casimir energy $E = -\frac{\pi c}{24L}$, which is different from that in periodic boundary conditions. Nevertheless, the dependence of the entanglement entropy and energy-momentum density on the matrix elements α_n (β_n) in the Π_n in Eq. (25) are similar.

There is rich information contained in the formula discussed above. As will be seen later, if the CFT is in a heating phase, there will be energy-momentum density peaks emerging in the real space. The locations of these peaks are determined by β_n/α_n. It turns out that both the quantities $S_A(n)$ and $E(n)$ can serve as "order parameters" to distinguish different emergent phases in the time-dependent driven CFTs. For example, for the periodically driven CFT as studied in Ref. [41], it is found there are two different phases with a heating phase and a nonheating phase, where the time evolution of entanglement entropy exhibits qualitatively different features as shown in Fig. 1. Also, it is found n Ref. [56] that the total energy grows exponentially fast as a function of driving cycles n in the heating phase and simply oscillates in the nonheating phase.

As a short summary, once we know the operator evolution in Eq. (24) or equivalently the matrix form in Eq. (25), one can study the entanglement and energy-momentum evolution based on Eqs. (27) and (30) or Eqs. (31) and (33).

D. Periodic, quasiperiodic, and random driving CFTs

In general, the sequence of unitary operators $\{U_j\}$ in Eq. (5) can be chosen in an arbitrary form. In this work, we are interested in three classes: periodic, quasiperiodic, and random drivings.

(1) *Periodical driving*: the sequence of unitary operators $\{U_j\}$ in (5) are chosen with a "period" p ($p \in \mathbb{Z}_+$) such that

[8]Hereafter, for convenience of writing, we write $T(x, t = \sum_{j=1}^n T_j)$ as $T(x,n)$.

[9]This can be seen by considering $q = 1$ in Eq. (30), but may be not obvious by looking at the expression of $S_A(n)$ in Eq. (27). For $q = 1$, the choice of the subsystem A in (27) fails because $A = [-L/2, L/2]$ corresponds to the total system. In our calculation of $S_A(n)$ in Eq. (27), we have assumed explicitly that the two entanglement cuts do not coincide, or equivalently A is not the total system.

$U_j = U_{j+p}$, $\forall\, j \in \mathbb{Z}$. Then the time evolution of wave function in (5) can be written as

$$|\Psi_{np}\rangle = (\underbrace{U_p \dots U_2 \cdot U_1}_{\text{one driving period}})^n |\Psi_0\rangle, \quad \text{with} \quad U_j = e^{-iH_j T_j}. \tag{34}$$

To obtain the physical properties of the system under periodic driving, we only need to analyze the corresponding transformation matrix $M_1 M_2 \dots M_p \in \mathrm{SU}(1,1)$ within a period.

(2) *Quasiperiodic driving*: $\{U_j\}$ form a quasiperiodic sequence. Quasiperiodicity is the property of a system that displays irregular periodicity, where the sequence exhibits recurrence with a component of unpredictability. (For example, see the review [67] for a more rigorous mathematical definition of quasiperiodic sequence.) In this paper, we will focus on the following two protocols of quasiperiodical driving:

(a) Fibonacci type. This is the type of quasiperiodic driving we will study in detail in Sec. V A. We use the Fibonacci bit string or word (see Appendix B)

$$X_{j=1,2,3\dots} = 10110101\dots \tag{35}$$

and two distinct unitaries U_A, U_B to generate a quasiperiodic driving sequence $U_j = X_j U_A + (1 - X_j) U_B$, i.e., we apply U_A (U_B) if the bit is 1 (0).

(b) Aubry-André type. In this case, we generate the quasiperiodic driving sequence as follows:

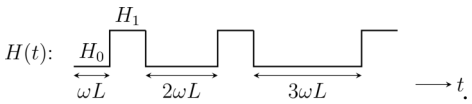

That is to say, we consider two Hamiltonians H_0 and H_1 and fix the driving period T_1 for H_1 while let the driving period of H_0 increase with driving cycle $T_0 = n\omega L$ where ω is an irrational number and L is the total length of the system. Note in terms of the unitary $U = \exp(-iH_0 T_0)$, its action on the operator only depends on T_0 mod L.

(3) *Random driving*: $\{U_j\}$ form a random sequence. More concretely, each U_j is drawn independently from the ensemble $\{(u_k, p_k)\}_{k=1\dots m}$, where $u_k = e^{-iH_k T_k}$ is the unitary matrix and p_k is the corresponding probability, with the normalization $\sum_k p_k = 1$.

In brief, for all the three kinds of time-dependent drivings, our goal is to describe the behavior of the physical properties of the CFT in the long-time driving limit $n \to \infty$, where n is the number of driving cycles.

As a remark, one can find that the types of driving sequence are similar to those in the potentials in crystals, quasicrystals, and disordered systems. One can find interesting relations between different phases of time-dependent driven CFTs and different types of wave functions in a lattice, as briefly discussed in the Introduction. Furthermore, both types of quasiperiodicities we mentioned above have been discussed in the quasicrystal literature, e.g., see Refs. [68–70].

III. DIAGNOSTICS

The previous section explains how the physical properties of an SL_2 driven CFT state can be extracted from the conformal mapping generated by the driving sequence. The mapping is further encoded in an SU(1, 1) matrix, denoted as Π_n in (25), which itself is a product of n SU(1, 1) matrices.

Mathematically, the long-time asymptotics of the driven state now can be understood by the n dependence of Π_n. In this section, we will introduce two useful diagnostics to characterize such dependence: (1) Lyapunov exponent; (2) group walking. The former is a simple scalar quantifying the growth of Π_n, while the latter is more refined and uses two points on the unit disk to track the trajectory of Π_n. Although not independent, both of them will be useful and used in the later sections.

A. Lyapunov exponent and heating phase

For all the three classes of drivings we introduced in the previous subsection, the problem is reduced to the study of the product Π_n [defined in (23)] of a sequence of SU(1,1) matrices that encode the conformal mappings. One useful and simple characterization for the growth rate of this matrix product is the so-called Lyapunov exponent (for a review of the subject see, e.g., [71]). Generally, we can consider a product of n matrices $\Pi_n = M_1 M_2 \dots M_n$, where $M_j \in \mathrm{SL}(d, \mathbb{R})$. Then, the (upper) Lyapunov exponent is defined as

$$\lambda_L := \lim_{n\to\infty} \frac{1}{n} \log \|M_1 M_2 \dots M_n\|, \tag{36}$$

where $\|\dots\|$ is a matrix norm. We would like to make a few comments about the definition here:

(1) Here, the specific choice of norm $\|\dots\|$ is not essential. To be explicit, we will choose the Frobenius norm in this paper, i.e.,

$$\|M\|_F := \left(\sum_{j,k} |M_{jk}|^2\right)^{\frac{1}{2}}. \tag{37}$$

(2) The definition also applies to $\mathrm{SL}(d, \mathbb{C})$, as one can always embed $\mathrm{SL}(d, \mathbb{C})$ in $\mathrm{SL}(2d, \mathbb{R})$.

(3) In general, one can define d Lyapunov exponents for $\mathrm{SL}(d, \mathbb{R})$. For example, for $\mathrm{SL}(2, \mathbb{R})$, one can define two extremal Lyapunov exponents

$$\lambda_+ := \lim_{n\to\infty} \frac{1}{n} \log \|M_1 M_2 \dots M_n\|, \tag{38}$$

$$\lambda_- := \lim_{n\to\infty} \frac{1}{n} \log \|(M_1 M_2 \dots M_n)^{-1}\|^{-1}, \tag{39}$$

with the property $\lambda_+ \geqslant 0 \geqslant \lambda_-$ since $\|B\| \geqslant 1 \geqslant \|B^{-1}\|^{-1}$ for $B \in \mathrm{SL}(2, \mathbb{R})$.

Applying to the SU(1, 1) matrix Π_n,

$$\Pi_n = \begin{pmatrix} \alpha_n & \beta_n \\ \beta_n^* & \alpha_n^* \end{pmatrix} \quad \text{where} \quad \alpha_n,\ \beta_n \in \mathbb{C}, \quad |\alpha_n|^2 - |\beta_n|^2 = 1, \tag{40}$$

a positive Lyapunov exponent $\lambda_L > 0$ implies that the matrix elements have the following asymptotics:

$$|\alpha_n| \sim |\beta_n| \sim \tfrac{1}{2} e^{\lambda_L n} \quad \text{at} \quad n \to \infty. \tag{41}$$

Following Eqs. (27) and (30), we find the asymptotics in long-time limit

$$S_A(n) - S_A(0) \sim \frac{c}{3}\lambda_L n, \quad E(n) \sim \frac{\pi c}{24L}(q^2-1)e^{2\lambda_L n}, \quad (42)$$

where we have neglected the contribution from the antichiral mode for the moment.[10] From this perspective, we may interpret the Lyapunov exponent λ_L as the heating rate in the heating phase. If $\lambda_L > 0$, then the time-dependent driven CFT must be in a heating phase, with the total energy exponentially growing in time. We will also explain in detail momentarily that since the norm of the ratio β_n/α_n approaches 1 in the long-time limit when $\lambda_L > 0$, an array of energy-momentum peaks will emerge in real space whose exact locations will be determined by the phase of the ratio β_n/α_n.

On the other hand, if $\lambda_L = 0$, the system is either in a nonheating phase or at the phase transition. We emphasize here that the vanishing of Lyapunov exponential allows a subexponential growth of the matrix norm $||\Pi_n||$ as a function of n, e.g., this could happen at the phase transition or boundary.

To summarize, using the Lyapunov exponent λ_L, we can classify the phases as follows:

$\lambda_L > 0$: heating phase (with exponentially growing energy),

$\lambda_L = 0$: nonheating phase or phase transition.

To further identify the detailed properties of entanglement and energy evolution in the nonheating phase and at the phase transition, one needs to study the finer structure of the matrix Π_n, which we will pursue in the next subsection.

The Lyapunov exponent works for general matrices. When specialized to SU(1, 1) or SL(2, $\mathbb{C}$), another commonly used classifier is the trace of the matrix. Namely, $|\operatorname{Tr} M| > 2$, $|\operatorname{Tr} M| = 2$, and $|\operatorname{Tr} M| < 2$ correspond to the hyperbolic, parabolic, and elliptic types of matrix, respectively. This criterion was used to identity different phases for the Floquet driving CFT studied in previous works [41,56].

For periodic driving, it follows from the definition of matrix norm that this trace classifier is equivalent to the Lyapunov exponent. We have $|\operatorname{Tr} M| > 2$ if and only if $\lambda_L > 0$, $|\operatorname{Tr} M| \leqslant 2$ if and only if $\lambda_L = 0$. One can also extend it to the quasiperiodic driving as follows. As will be detailed discussed later, any quasiperiodic driving corresponding to an irrational number w can be considered as the limit of a sequence of periodic driving, which is generated by the continued fractions of ω. For each element in the sequence, we can apply the trace classifier to obtain a sequence of phase diagram, with its limit being the true phase diagram for the quasiperiodic driving system.

For the random driving, the Lyapunov exponent will become a more appropriate definition, which we use exclusively in the corresponding discussion.

B. Group walking: Fine structures of the time-dependent driving

The Lyapunov exponent defined in the previous subsection is a single number. To view the "internal structure" in the matrix product Π_n in Eq. (25), it is helpful to study how the matrix elements evolve in time, which determines the time evolution of the entanglement entropy and the energy-momentum density.

A convenient parametrization of the SU(1, 1) matrices such as M_j and Π_n in (23) is given as follows:

$$\Pi(\rho,\zeta) = \frac{1}{N_\rho}\begin{pmatrix} \sqrt{\zeta} & -\rho^* \frac{1}{\sqrt{\zeta}} \\ -\rho\sqrt{\zeta} & \frac{1}{\sqrt{\zeta}} \end{pmatrix} \quad \text{where} \quad \rho \in \mathbb{D}, \quad \zeta \in \partial\mathbb{D}, \quad (43)$$

and $N_\rho = \sqrt{1-|\rho|^2}$ is the normalization factor.[11] The unit disk $\mathbb{D} := \{z \in \mathbb{C}, |z| < 1\}$, the boundary(or edge) of the disk $\partial\mathbb{D} := \{z \in \mathbb{C}, |z| = 1\}$, and the complex numbers ρ and ζ are depicted as follows:

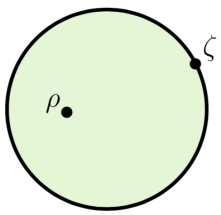

$\rho \in \mathbb{D}$
$\zeta \in \partial\mathbb{D}$. (44)

Thus, the evolution of matrix Π_n as a function of step n can be captured by the evolution of a pair of points (ρ_n, ζ_n) on the unit disk. We will call this process "group walking" for brevity. An equivalent but more convenient parametrization of the trajectory (ρ_n, ζ_n) is to use $(\rho_n, \rho_n\zeta_n)$. For example, the total energy (30), locations of the energy-momentum density peaks (29) and entanglement entropy (27) are expressible using $(\rho_n, \rho_n\zeta_n)$:

(1) The energy formula in Eq. (30) only depends on ρ_n,

$$E(n) = -\frac{q^2\pi c}{12L} + \frac{\pi c}{12L}(q^2-1)\frac{1+|\rho_n|^2}{1-|\rho_n|^2} + \text{antichiral part}, \quad (45)$$

and increases monotonically with respect to $|\rho_n|$.

In the heating phase, the exponential growth of $E(n)$ as a function of n is tied to the phenomenon that $|\rho_n|$ approaches exponentially close to the boundary $\partial\mathbb{D}$. On the other hand, if the total energy simply oscillates in n, e.g., in the nonheating phase of a periodically driven CFT, then $|\rho_n|$ should follow

[10] More precisely, the formula on $S_A(n) - S_A(0)$ holds when the chiral or antichiral energy-momentum density peaks are in the interior of A (see Sec. IV C). When the entanglement cuts lie on the centers of the energy-momentum density peaks, $S_A(n)$ could even decrease in time (see Appendix A 3 b).

[11] More precisely, the above parametrization ($\rho \in \mathbb{D}, \zeta \in \partial\mathbb{D}$) of matrix Π only covers the SU(1, 1)/$\mathbb{Z}_2$, to obtain the full SU(1, 1) group, one needs to let ζ live on the double cover of the boundary circle. However, our physical quantities are obtained from the Möbius transformation rather than the SU(1, 1) matrix directly, the former is indeed isomorphic to the $\mathbb{Z}_2$ quotient of the latter, namely, SU(1, 1)/$\mathbb{Z}_2$, and agrees with our parametrization.

the same oscillation pattern. In-between, as a we approach the phase transition, the orbit of ρ should be closer and closer to the boundary. As a summary, the behaviors of ρ described above can be visualized by the following cartoon:

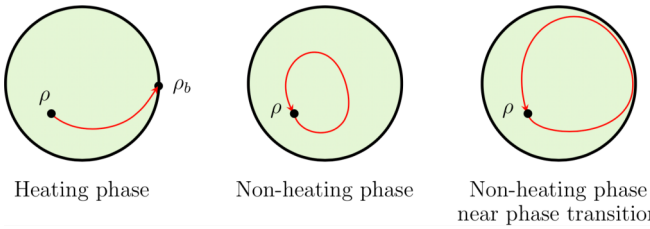

(46)

Here we sketch the rough features of the group walking of ρ_n; this cartoon is not meant to be exact. As we will see in Sec. V on the quasiperiodically driven CFT, in general there are many rich fine structures on the orbit of ρ.

(2) The locations of the energy-momentum density peaks are determined by $(\rho_n\zeta_n)$ only. Recall that the poles of the (chiral) energy-momentum density (29)

$$\frac{1}{2\pi}\langle T(x,n)\rangle = -\frac{q^2\pi c}{12L^2} + \frac{\pi c}{12L^2}(q^2-1)\frac{1}{|\alpha_n e^{\frac{2\pi i x}{l}} + \beta_n|^4}, \quad \text{where } l = L/q \tag{47}$$

locate at $-\frac{\beta_n}{\alpha_n} = (\rho_n\zeta_n)^*$, which determines the locations of peaks if $|\frac{\beta_n}{\alpha_n}| = |\rho_n\zeta_n| = |\rho_n| \to 1$, with

$$e^{\frac{2\pi i x_{\text{peak}}}{l}} = -(\rho_n\zeta_n)^* \quad \text{if } |\rho_n| \to 1, \tag{48}$$

i.e., $x_{\text{peak}} = \frac{l}{2\pi i}\log[-(\rho_n\zeta_n)^*] + kl$ with $k = 0,\ldots,q-1$. For x away from x_{peak}, the energy-momentum density will be greatly suppressed. The same conclusion also holds for the antichiral component $\langle\overline{T}(x,n)\rangle$.

(3) The entanglement entropy in Eq. (27) depends on both ρ_n and $\rho_n\zeta_n$,

$$S_A(n) - S_A(0) = \frac{c}{3}\log\frac{|1+(\rho_n\zeta_n)^*|}{\sqrt{1-|\rho_n|^2}}, \tag{49}$$

where we have neglected the contribution of the antichiral mode.

In summary, the group walking of ρ_n and $(\rho_n\zeta_n)$ on a unit disk $\mathbb{D}$ determine the behaviors of the energy-momentum and entanglement evolution as follows:

(1) $|\rho_n|$ determines the growth of total energy.

(2) In the heating phase, $(\rho_n\zeta_n)$ in the long driving limit ($n \gg 1$) determines the location of peaks of the energy-momentum density.

(3) $|\rho_n|$ and $(\rho_n\zeta_n)$ together determine the time evolution of the entanglement entropy $S_A(n)$.

IV. PERIODIC DRIVING

This section is a generalization of previous works in Refs. [41,56] by considering a more general setup of periodic drivings. Apart from its own interesting features, this generalized setup can be used to analyze the quasiperiodically driven CFTs in Sec. V.

In Refs. [41,56], a minimal setup of a periodic driving with two driving steps within one driving period was considered. The two different driving Hamiltonians are chosen as H_0 and $H_1 = H_{\text{SSD}}$ being the sine-square deformed Hamiltonian. Here we generalize this minimal setup in two aspects: one is to consider arbitrary SL_2 deformed Hamiltonians, and the other is to consider more general periodic sequences (see Fig. 5). In general, as the number of driving steps within a driving period increases, the phase diagram will become quite rich.[12]

A. General protocol for periodic driving

For a periodical driving with period $p \in \mathbb{Z}^+$, we have $U_j = U_{j+p}$ for all $j \in \mathbb{Z}_+$. Then the time evolution of wave function after np driving steps is determined by the unitary operators $(U_p\ldots U_2U_1)$ as follows:

$$|\Psi_{np}\rangle = (\underbrace{U_p\ldots U_2U_1}_{\text{one driving period}})^n|\Psi_0\rangle, \quad \text{with} \quad U_j = e^{-iH_jT_j}. \tag{50}$$

In terms of conformal mapping, the operator evolution after np driving steps only depends on the the matrix product

$$\Pi_p := M_1M_2\ldots M_p \in \text{SU}(1,1). \tag{51}$$

Let us denote the matrix elements of Π_p and $(\Pi_p)^n$ as follows:

$$\Pi_p = \begin{pmatrix}\alpha_p & \beta_p\\ \beta_p^* & \alpha_p^*\end{pmatrix}, \quad (\Pi_p)^n = \begin{pmatrix}\alpha_{np} & \beta_{np}\\ \beta_{np}^* & \alpha_{np}^*\end{pmatrix} \coloneqq \begin{pmatrix}\alpha_p & \beta_p\\ \beta_p^* & \alpha_p^*\end{pmatrix}^n. \tag{52}$$

Next, we will determine the phase diagrams and relevant physical quantities based on the operator evolution given by Π_p, or equivalently the following Möbius transformation

$$z' = \Pi_p z = \begin{pmatrix}\alpha_p & \beta_p\\ \beta_p^* & \alpha_p^*\end{pmatrix} z = \frac{\alpha_p z + \beta_p}{\beta_p^* z + \alpha_p^*} \tag{53}$$

and similarly for $\bar{z}$.

1. Phase diagram and Lyapunov exponents

The matrix $\Pi_{np} = (\Pi_p)^n$ has three distinct asymptotics depending on the trace of Π_p, for convenience, let us classify the types of SU(1, 1) matrices in parallel to the classification of Möbius transformation we used in Ref. [56] (also see Fig. 6 for an illustration).

[12] See, e.g., Fig. 14 in the next section where we use increasingly long periodic drivings to approach the quasiperiodic driving.

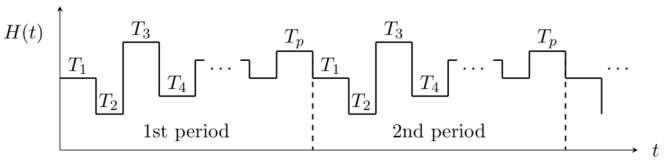

FIG. 5. A general protocol for a periodically driven CFT. There are p steps of driving within each driving period. In the ith step of driving, we consider the driving with (H_i, T_i), where H_i is a SL_2 deformed Hamiltonian in Eq. (7) and T_i is the corresponding time interval of driving.

Let $M \in SU(1,1)$ not be the central elements $\pm\mathbb{I}$, then we call the matrix M the following:

(1) Elliptic if $|\operatorname{Tr}(M)| < 2$. M has two distinct eigenvalues λ_1, λ_2 with $\lambda_2 = \lambda_1^*$ and $|\lambda_1| = |\lambda_2| = 1$. The corresponding Möbius transformation has two distinct fixed points, one inside the unit circle and the other outside.

(2) Parabolic if $|\operatorname{Tr}(M)| = 2$. M has a single eigenvalue at $+1$ or -1. The corresponding fixed points become degenerate (i.e., only one single point) and stay on the circle.

(3) Hyperbolic if $|\operatorname{Tr}(M)| > 2$. M has two distinct real eigenvalues λ_1, λ_2, $|\lambda_1| > 1 > |\lambda_2|$ and $\lambda_2 = \lambda_1^{-1}$. The two fixed points are distinct and staying on the circle.

As a reminder, the fixed points of the Möbius transformation are a convenient way to characterize the transformation when we repeat it multiple times.[13] We rewrite the Möbius transformation into the form

$$\frac{z'-\gamma_1}{z'-\gamma_2} = \eta \frac{z-\gamma_1}{z-\gamma_2}, \tag{54}$$

where $\gamma_{1,2}$ are the fixed points we mentioned, and η is the multiplier. For Π_p parametrized in (52), we have the following explicit formulas:

$$\gamma_{1,2} = \frac{1}{2\beta_p^*}[(\alpha_p - \alpha_p^* \mp \sqrt{(\alpha_p + \alpha_p^*)^2 - 4})], \tag{55}$$

$$\eta = \frac{\operatorname{Tr}(\Pi_p) + \sqrt{[\operatorname{Tr}(\Pi_p)]^2 - 4}}{\operatorname{Tr}(\Pi_p) - \sqrt{[\operatorname{Tr}(\Pi_p)]^2 - 4}},$$

$$\text{where } \operatorname{Tr}(\Pi_p) = \alpha_p + \alpha_p^*. \tag{56}$$

Note the sign of the discriminant depends on the trace of Π_p, which can be used to categorize the Möbius transform (54) (see Fig. 6 for an illustration). For parabolic class when $|\operatorname{Tr}(\Pi_p)| = 2$, we have $\gamma_1 = \gamma_2$, the transformation (54) becomes trivial and we need to invoke

$$\frac{1}{z'-\gamma} = \frac{1}{z-\gamma} + \beta_p^*, \quad \text{where} \quad \gamma = \frac{\alpha_p - \alpha_p^*}{2\beta_p^*}. \tag{57}$$

When repeating n times, we only need to modify $\eta \to \eta^n$ for $|\operatorname{Tr}(\Pi_p)| \neq 2$ case and $\beta_p^* \to n\beta_p^*$ for $|\operatorname{Tr}(\Pi_p)| = 2$. And, therefore, we have a simple expression for the matrix elements of $(\Pi_p)^n$ defined in (52):

$$\alpha_{np} = \frac{\eta^{-\frac{n}{2}}\gamma_1 - \eta^{\frac{n}{2}}\gamma_2}{\gamma_1 - \gamma_2}, \quad \beta_{np} = \frac{(\eta^{\frac{n}{2}} - \eta^{-\frac{n}{2}})\gamma_1\gamma_2}{\gamma_1 - \gamma_2}$$
$$\text{when} \quad |\operatorname{Tr}(\Pi_p)| \neq 2, \tag{58}$$

$$\alpha_{np} = 1 + n\gamma\beta_p^*, \quad \beta_{np} = -n\gamma^2\beta_p^* \quad \text{when} \quad |\operatorname{Tr}(\Pi_p)| = 2. \tag{59}$$

Another advantage of the representation using fixed points $\gamma_{1,2}$ and multiplier η is that the Lyapunov exponent now only depends on η as follows:

$$\lambda_L = \frac{1}{2p}\log(\max\{|\eta|, |\eta|^{-1}\})$$
$$= \frac{1}{p}\log\left|\frac{|\operatorname{Tr}(\Pi_p)| + \sqrt{|\operatorname{Tr}(\Pi_p)|^2 - 4}}{2}\right|. \tag{60}$$

That is to say, the hyperbolic Π_p with $|\operatorname{Tr}(\Pi_p)| > 2$ implies a positive Lyapunov exponent and therefore heating phase, while the elliptic and parabolic classes both have $\lambda_L = 0$. By analyzing the corresponding group walk in the next subsection we will confirm that $|\operatorname{Tr}(\Pi_p)| < 2$ corresponds to nonheating phase while $|\operatorname{Tr}(\Pi_p)| = 2$ is the phase transition as expected.

B. Group walking

The group walking $(\rho_{np}, \rho_{np}\zeta_{np})$ of $(\Pi_p)^n$ defined in (43) can be straightforwardly obtained by comparing with (58) for $|\operatorname{Tr}(\Pi_p)| \neq 2$,

$$\rho_{np} = -\frac{1}{\gamma_2} + \frac{1}{\gamma_2}\frac{\gamma_1 - \gamma_2}{\gamma_1 - \eta^n\gamma_2},$$
$$(\rho_{np}\zeta_{np}) = \frac{1}{\gamma_1} + \frac{1}{\gamma_1}\frac{\gamma_2 - \gamma_1}{\eta^n\gamma_1 - \gamma_2}, \tag{61}$$

or comparing with (59) for $|\operatorname{Tr}(\Pi_p)| = 2$,

$$\rho_{np} = -\frac{n\beta^*}{1 + n\gamma\beta^*}, \quad (\rho_{np}\zeta_{np}) = -\frac{n\beta^*}{1 - n\gamma\beta^*}. \tag{62}$$

Now we are ready to discuss the trajectories of $(\rho_{np}, \rho_{np}\zeta_{np})$ with increasing n:

(1) For $|\operatorname{Tr}(\Pi_p)| < 2$, the multiplier $\eta \in U(1)$ is a pure phase and implies that both ρ_{np} and $(\rho_{np}\zeta_{np})$ will form a closed loop in the unit disk.

(2) For $|\operatorname{Tr}(\Pi_p)| > 2$, the multiplier $|\eta| \neq 1$ and we have the following limit at $n \to \infty$:

$$\lim_{n\to\infty}\rho_{np} = \begin{cases} -\gamma_2^*, & \eta > 1 \\ -\gamma_1^*, & \eta < 1 \end{cases} \quad \lim_{n\to\infty}(\rho_{np}\zeta_{np}) = \begin{cases} \gamma_1^*, & \eta > 1 \\ \gamma_2^*, & \eta < 1. \end{cases} \tag{63}$$

Recall that both γ_1 and γ_2 live on $\partial\mathbb{D}$ as shown in Fig. 6. Therefore, in this case, both ρ_n and $(\rho_{np}\zeta_{np})$ will approach exponentially close to the boundary of the unit disk $\partial\mathbb{D}$.

(3) For $|\operatorname{Tr}(\Pi_p)| = 2$, we have the limit

$$\lim_{n\to\infty}\rho_{np} = -\gamma^*, \quad \lim_{n\to\infty}(\rho\zeta)_{np} = \gamma^*, \tag{64}$$

where $\gamma^* \in \mathbb{D}$ as shown in Fig. 6. From Eq. (62), we notice that in this case, both ρ_{np} and $(\rho_{np}\zeta_{np})$ will approach $\partial\mathbb{D}$ polynomially (in n) close.

[13] Therefore, this is the main tool we used in the previous study [56] to visualize the effects of periodic driving.

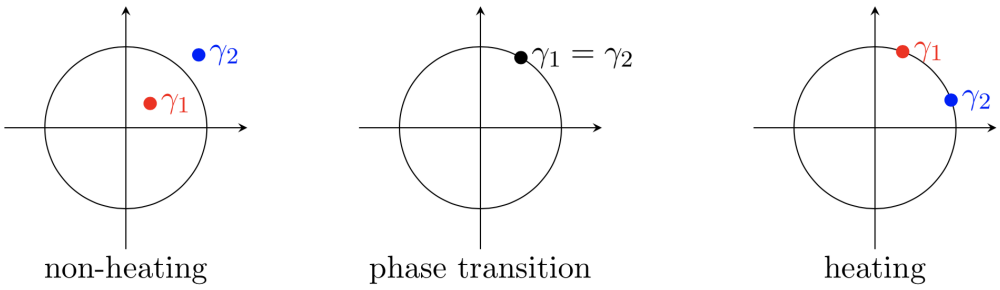

FIG. 6. Illustration for the locations of fixed points of Möbius transformation in the three phases. In the nonheating phase, the two fixed points are inside and outside the unit circle, respectively. They will merge at the same point on the unit circle at the phase transition. Then, the two fixed points will split but still sit on the unit circle in the heating phase.

The above behavior confirms that $|\mathrm{Tr}(\Pi_p)| < 2$, $|\mathrm{Tr}(\Pi_p)| > 2$, and $|\mathrm{Tr}(\Pi_p)| = 2$ correspond to nonheating, heating, and phase transition respectively.

C. Entanglement and energy evolution

Given the explicit expressions of the matrix elements of $\Pi_{np} = (\Pi_p)^n$ in (58) and (59), we can further obtain the time evolution of the entanglement entropy $S_A(N = np)$ and the total energy $E(N = np)$ based on formulas (27) and (30), respectively. For the total energy, it grows exponentially in the heating phase

$$E(N) \simeq \frac{\pi c}{24L}(q^2 - 1)e^{2\lambda_L N}, \quad \text{where } N = np, \tag{65}$$

and the exponent is exactly twice the Lyapunov exponent, the latter is given in (60). In the nonheating phase and the phase transition, the total energy oscillates and grows polynomially. Here we only consider the contribution of the chiral modes, the antichiral modes follow parallel discussions.

As noted in Ref. [56], the energy-momentum density has interesting spatial structures. In fact, as mentioned in Sec. III A, a positive Lyapunov exponent λ_L indicates there is an array of peaks in the energy-momentum density $\langle T(x, n)\rangle$ in real space. The same spatial structure, namely, the array of peaks, is also present at the phase transition with $\lambda_L = 0$, although the growth is polynomial in n, significantly slower than the heating phase.

Following Eqs. (29), (58), and (59), we find the locations of the (chiral) energy-momentum peaks are given as follows:

$$\begin{aligned} &\exp\left(\frac{2\pi i x_{\text{peak}}}{l}\right) = -\lim_{n\to\infty}\frac{\beta_{np}}{\alpha_{np}} = \gamma_2, \quad \text{in the heating phase} \\ &\exp\left(\frac{2\pi i x_{\text{peak}}}{l}\right) = -\lim_{n\to\infty}\frac{\beta_{np}}{\alpha_{np}} = \gamma, \quad \text{at the phase transition} \end{aligned} \tag{66}$$

where we have assumed $0 < \eta < 1$ in the above formula, for $\eta > 1$, we need to replace γ_2 by γ_1. Here γ_2 corresponds to the unstable fixed point in the Möbius transformation in the heating phase, and γ is the unique fixed point at the phase transition. A cartoon plot of the energy-momentum density distribution in real space is shown as follows:

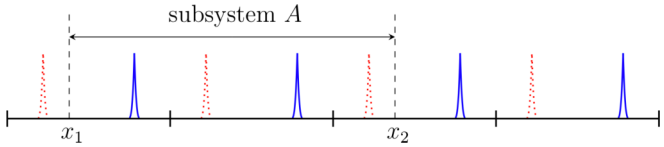

, (67)

where different colors represent different chiralities. For simplicity, let us keep the antichiral part (red) undeformed, and only deform the chiral part (blue). Then the entanglement entropy in the heating phase depends on the choice of subsystem A as follows [56]:

$$S_A(N = np) - S_A(0) \simeq \begin{cases} \mathcal{O}(1), & [x_1, x_2] \text{ does not include peaks} \\ \frac{c}{3}\lambda_L N, & [x_1, x_2] \text{ includes peak(s).} \end{cases} \tag{68}$$

If one also deforms the antichiral part and let it live in heating phase with Layapunov exponent λ_L', then we need to add up two contributions when A also includes any antichiral peaks. Note in general $\lambda_L \neq \lambda_L'$ as they can be deformed independently in the CFT with periodic boundary condition. One can further check the entanglement pattern by looking into the mutual information as studied in [56], and find each peak is mainly entangled with the two peaks of its nearest neighbor with the same chirality, as schematically shown in Fig. 2.

At the phase transition, similar to the energy, the spatial structure of the entanglement persists, while the growth is slower

$$S_A(N = np) - S_A(0) \simeq \begin{cases} \mathcal{O}(1), & [x_1, x_2] \text{ does not include peaks} \\ \frac{c}{3}\log n, & [x_1, x_2] \text{ includes peak(s).} \end{cases} \tag{69}$$

One final remark is that in the above discussions, the entanglement cuts are chosen to avoid the centers of the energy-momentum density peaks. In Appendix A 3 b, we also consider the cases when the entanglement cuts are located at the center(s) of the energy-momentum density peaks. Then,

TABLE I. Correspondence of the phase diagram in a *periodically* driven CFT and other quantities.

Phases	Möbius transf.	$\lvert\mathrm{tr}\,\Pi_p\rvert$	λ_L	EE growth	Energy growth
Heating	Hyperbolic	>2	$\lambda_L > 0$	Linear	Exponential
Nonheating	Elliptic	<2	$\lambda_L = 0$	Logarithmic	Power law
Phase transition	Parabolic	$=2$	$\lambda_L = 0$	Oscillating	Oscillating

some interesting features in the entanglement entropy could arise. To summarize, we put the phase diagrams and related quantities in the periodically driven CFT in Table I.

D. A minimal setup

Now we consider a minimal setup of the periodically driven CFT to demonstrate the main features in the previous discussions. In this setup, we consider only $p = 2$ driving steps within one period

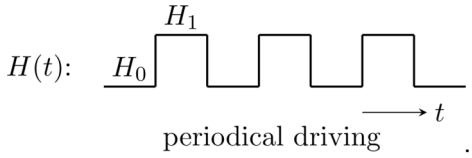

(70)

That is, we drive the CFT with (H_0, T_0) and (H_1, T_1), where T_0 and T_1 are the time intervals. We consider a SL_2 deformed Hamiltonian with $q = 1$ with open boundary conditions:[14]

$$H_\theta = \int_0^L \left(1 - \tanh(2\theta)\cos\frac{2\pi qx}{L}\right) T_{00}(x)dx, \quad q = 1,\ \theta > 0. \tag{71}$$

We choose H_0 and H_1 as $H_{\theta=0}$ and $H_{\theta\neq 0}$, and T_0 and T_1 as $T_{\theta=0}$ and $T_{\theta\neq 0}$, respectively. Note that $H_{\theta=0}$ corresponds to the uniform Hamiltonian, and $H_{\theta=\infty}$ corresponds to the SSD Hamlitonian in Eq. (15) up to an overall factor 2. Denoting the time interval of driving as T_θ, then the corresponding Möbius transformation $M(H_\theta, T_\theta)$ has the form

$$M(H_\theta, T_\theta) = \begin{pmatrix} \alpha & \beta \\ \beta^* & \alpha^* \end{pmatrix} \quad \text{with} \quad \begin{cases} \alpha = \cos\left(\frac{\pi T_\theta}{L_{\text{eff}}}\right) + i\cosh(2\theta)\sin\left(\frac{\pi T_\theta}{L_{\text{eff}}}\right), \\ \beta = -i\sinh(2\theta)\sin\left(\frac{\pi T_\theta}{L_{\text{eff}}}\right). \end{cases} \tag{72}$$

Here $L_{\text{eff}} = L\cosh(2\theta)$ denotes the effective length of the total system. Physically, it characterizes the effective distance that the quasiparticle needs to travel to return to its original location [48].

1. Phase diagram and Lyapunov exponent

The Lyapunov exponent λ_L is determined by the trace of the transformation matrix Π_p as shown in (60). In our setting $p = 2$ and

$$\begin{aligned} |\mathrm{Tr}(\Pi_{p=2})| &= |\mathrm{Tr}(M_0M_1)| \\ &= 2|\cosh(2\theta)\sin x_1 \sin x_0 - \cos x_1 \cos x_0|, \end{aligned} \tag{73}$$

where $x_0 = \frac{\pi T_0}{L}$ and $x_1 = \frac{\pi T_1}{L_{\text{eff}}}$, with $L_{\text{eff}} = L\cosh(2\theta)$. Therefore, inserting into

$$\lambda_L = \frac{1}{p}\log\left|\frac{|\mathrm{Tr}(\Pi_p)| + \sqrt{|\mathrm{Tr}(\Pi_p)|^2 - 4}}{2}\right|, \tag{74}$$

we obtain the result shown in Fig. 7. From the figure, we can also read out the phase diagram straightforwardly, namely, the regime with $\lambda_L > 0$ corresponds to the heating phase, while the dark blue regime with $\lambda_L = 0$ corresponds to nonheating phase, and the boundary between them is the phase transition.

[14]We choose open boundary condition here for the purpose of providing a comparison with the lattice simulation that will be shown momentarily, where it is natural to take open boundary condition.

We also show in Fig. 8 the group walking pictures for $\theta = 0.2$ with different choices of T_1/L.

To gain some analytical understanding of the formula for Lyapunov exponent, let us consider a simple example when $\theta = \infty$, namely, $H_1 = H_{\text{SSD}}$. Along the line $T_0 = L/2$, (73) simplifies to $|\mathrm{Tr}(\Pi_{p=2})| = \frac{2\pi T_1}{L}$. And, therefore, the Lyapunov exponent is a function of T_1 given as follows:

$$\lambda_L(T_1) = \frac{1}{2}\log\left(\frac{\pi T_1 + \sqrt{(\pi T_1)^2 - L^2}}{L}\right), \quad \text{where} \quad \theta = \infty,\ T_0 = L/2. \tag{75}$$

In particular, in the limit $T_1 \gg L$, we have

$$\lambda_L(T_1) \simeq \frac{1}{2}\log\left(\frac{\pi T_1}{L}\right). \tag{76}$$

That is to say, along the line $T_0 = L/2$, the Lyapunov exponent grows logarithmically with T_1/L in the large T_1 limit ($T_1/L \gg 1$). In fact, for $\theta = \infty$, the result in (76) holds for arbitrary $T_0/L \neq n\pi$ ($n \in \mathbb{Z}$) in the large T_1/L limit.

Now we would like to make a few comments on Fig. 7:

(1) The area of regime with larger Lyapunov exponent grows when we increase the parameter θ in Hamiltonian. The heuristic argument is that when the "difference" between H_0 and H_θ is greater, the driving protocol is easier to heat the system.

(2) When we push $\theta \to 0$, the area of heating phase, namely the regime with $\lambda_L > 0$, decreases to zero. How-

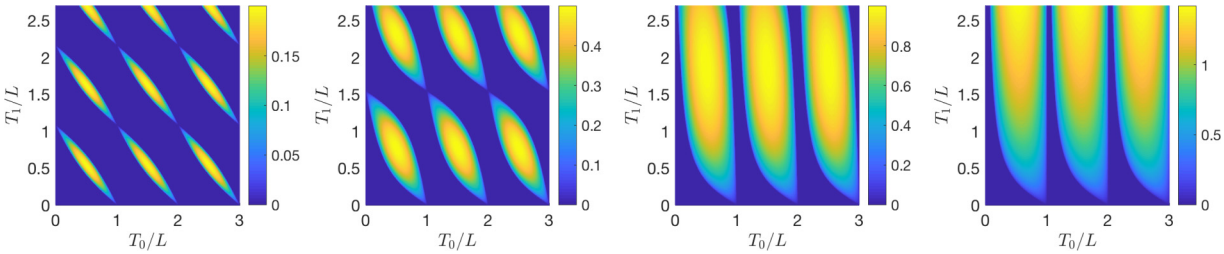

FIG. 7. Lyapunov exponent with (from left to right) $\theta = 0.2, 0.5, 1$, and ∞. The regime with $\lambda_L > 0$ corresponds to the heating phase, while the dark blue regime with $\lambda_L = 0$ corresponds to nonheating phase, and boundary between them is the phase transition.

ever, there is always at least a point $(T_0/L, T_1/L_{\text{eff}}) = (\frac{1}{2}, \frac{1}{2})$ staying in the heating phase for arbitrary $\theta \neq 0$. This point corresponds to $x_0 = x_1 = \frac{\pi}{2}$ in Eq. (73) where we find $|\text{Tr}(M_0 M_1)| = 2\cosh(2\theta) > 2$ for arbitrary $\theta \neq 0$.

Now, let us take a closer look at the special point $(T_0/L, T_1/L_{\text{eff}}) = (\frac{1}{2}, \frac{1}{2})$ in the heating phase. In terms of the transformation matrix M_0 and M_1 given in (72), we have

$$M_0 = \begin{pmatrix} i & 0 \\ 0 & -i \end{pmatrix}, \quad M_1 = \begin{pmatrix} i\cosh(2\theta) & -i\sinh(2\theta) \\ i\sinh(2\theta) & -i\cosh(2\theta) \end{pmatrix}. \tag{77}$$

These two matrices are actually special examples of a larger class of SU(1, 1) matrix defined below.

Reflection. Let M be an SU(1, 1) matrix parametrized as (43), namely,

$$M(\rho, \zeta) = \frac{1}{\sqrt{1-|\rho|^2}} \begin{pmatrix} \sqrt{\zeta} & -\rho^* \frac{1}{\sqrt{\zeta}} \\ -\rho\sqrt{\zeta} & \frac{1}{\sqrt{\zeta}} \end{pmatrix}, \tag{78}$$

we call M a reflection if $\zeta = -1$, i.e.,

$$M(\rho, \zeta = -1) = \frac{1}{\sqrt{1-|\rho|^2}} \begin{pmatrix} i & i\rho^* \\ -i\rho & -i \end{pmatrix} \tag{79}$$

is a reflection. This condition is equivalent to demanding matrix M is traceless $\text{Tr}[M(\rho, \zeta)] = 0$. One important property of the reflection matrix is that it squares to -1, i.e.,

$$M(\rho, -1)^2 = -1. \tag{80}$$

Apparently, a reflection matrix is elliptic since its trace is smaller than 2. But the product of two distinct reflection matrices is hyperbolic, i.e, $|\text{Tr}[M(\rho_1, -1)M(\rho_2, -1)]| > 2$. The reflection matrix will also play an important role in later discussions on both the quasiperiodically driven and the randomly driven CFTs [62].

Applying to our case where we have two distinct reflection matrix M_0 and M_1, we conclude that $\Pi_2 = M_0 M_1$ is hyperbolic and therefore induces a heating phase for $(T_0, T_1) = (L/2, L_{\text{eff}}(\theta)/2)$.[15] Indeed, we can explicitly check that the Lyapunov exponent has a simple form (assuming $\theta > 0$)

$$\lambda_L = \theta. \tag{81}$$

In addition, we have

$$\Pi_{np} = (\Pi_p)^n = (M_0 M_1)^n = (-1)^n \begin{pmatrix} \cosh(2n\theta) & -\sinh(2n\theta) \\ -\sinh(2n\theta) & \cosh(2n\theta) \end{pmatrix}, \tag{82}$$

which further fixes the location of the energy-momentum peak to be at $x = 0$ ($x = L$) for the chiral (antichiral) mode [cf. Eq. (32) for the open boundary condition discussed here]. In fact, the chiral and antichiral peaks switch positions after each driving period.

The total energy and entanglement entropy are also expressible using θ [cf. (31) and (33)]:

$$E(N = np) = \frac{\pi c}{8L}\cosh(4n\theta) - \frac{\pi c}{6L}, \tag{83}$$

$$S_A(N = np) - S_A(0) = \frac{c}{3} 2n\theta, \tag{84}$$

where $p = 2$ and we consider $A = [0, L/2]$ here. We will compare this CFT result with the numerical calculation on a lattice model in the next subsection.

2. *Numerical simulation on lattice*

In Ref. [41], the authors compare the CFT and lattice calculations on the entanglement entropy evolution in a periodically driven CFT. It was found that the comparison agrees very well in the nonheating phases, but deviates in the heating phase. The heuristic reason is that the two driving Hamiltonians in [41] are chosen as H_0 and $H_{\theta=\infty}$, which result in a large Layapunov exponent in the heating phase (see Fig. 7). Then, the system can be easily heated up with only a few driving steps. It is noted that the higher-energy modes in a lattice system are no longer well described by the CFT, which results in a deviation between the lattice and CFT calculations. Now, by considering the general H_θ, we can tune the system to have a small heating rate by choosing a small θ.

The lattice model we consider is a free-fermion lattice, which has finite sites L with open boundary conditions. We prepare the initial state as the ground state of

$$H_0 = \frac{1}{2}\sum_{j=1}^{L-1} c_j^\dagger c_{j+1} + \text{H.c.} \tag{85}$$

[15] Here we comment that for two arbitrary elliptic and noncommuting Hamiltonians H_0 and H_1, the corresponding SU(1, 1) matrices can be tuned to *reflection* matrices by choosing appropriate T_0 and T_1 (see Appendix A). At this point, the system will always be in a heating phase.

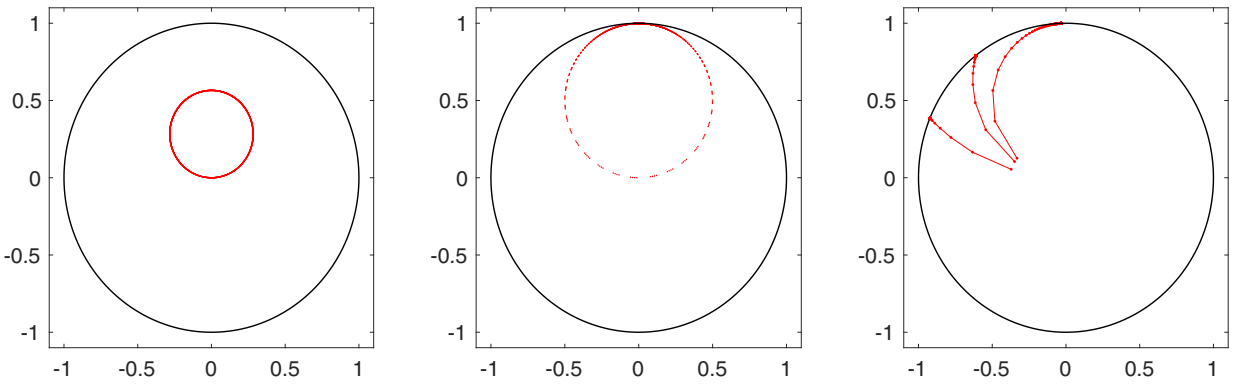

FIG. 8. Trajectories of $(\rho_{np}\zeta_{np})$ on the unit disk $\mathbb{D}$ in a periodically driven CFT driven with H_0 and $H_1 = H_\theta$ in Eq. (71). Here we choose $\theta = 0.2$, $T_0 = L/2$, and $T_1/[L\cosh(2\theta)] = 0.3$ in the nonheating phase (left), $T_1/[L\cosh(2\theta)] = 0.3758$ in the nonheating phase near the phase transition (middle, the phase transition happens at $\frac{1}{\pi}\arcsin[1/\cosh(2\theta)] \simeq 0.3759$), and $T_1/[L\cosh(2\theta)] = 0.376,\ 0.4$, and 0.45 (in the counterclockwise order) in the heating phase (right).

with half-filling. The SL_2 deformed Hamiltonian has the form

$$H_1 = \frac{1}{2}\sum_{j=1}^{L-1} f(j)c_j^\dagger c_{j+1} + \text{H.c.}, \tag{86}$$

where $f(j) = 1 - \tanh(2\theta)\cos\frac{2\pi j}{L}$, c_j are fermionic operators satisfying the anticommutation relations $\{c_j, c_k\} = \{c_j^\dagger, c_k^\dagger\} = 0$, and $\{c_j, c_k^\dagger\} = \delta_{jk}$. One can refer to the Appendix in Ref. [41] for the details of calculation of the entanglement entropy and correlation functions. The comparison of the numerical and CFT calculations on both the entanglement and energy time evolution can be found in Fig. 9. The agreement is remarkable.

One can also refer to Appendix A 3 c for the interesting case that when the entanglement cut lie at the center of both the chiral and antichiral energy-momentum density peaks, the entanglement entropy can decrease linearly in time.

V. QUASIPERIODIC DRIVING

In this section, we will study the nonequilibrium dynamics in a quasiperiodically driven CFT with SL_2 deformed Hamiltonians. We would like to understand the following two questions in this section:

(1) How does the phase diagram change as we shift the periodic driving protocol to the quasiperiodic driving?

(2) What is the generic feature of the entanglement and energy evolution in the quasiperiodically driven CFT?

As an initial effort to answer these questions, we will mainly focus on the case of quasiperiodical driving with a Fibonacci sequence, which is simpler to handle compared to a more general quasiperiodic sequence. Our setup is closely related to the Fibonacci quasicrystal, which was proposed in the early 1980s by Kohmoto, Kadanoff, and Tang [68], and Ostlund, Pandit, Rand, Schellnhuber, and Siggia [69]. It was observed and later proved that the spectrum of

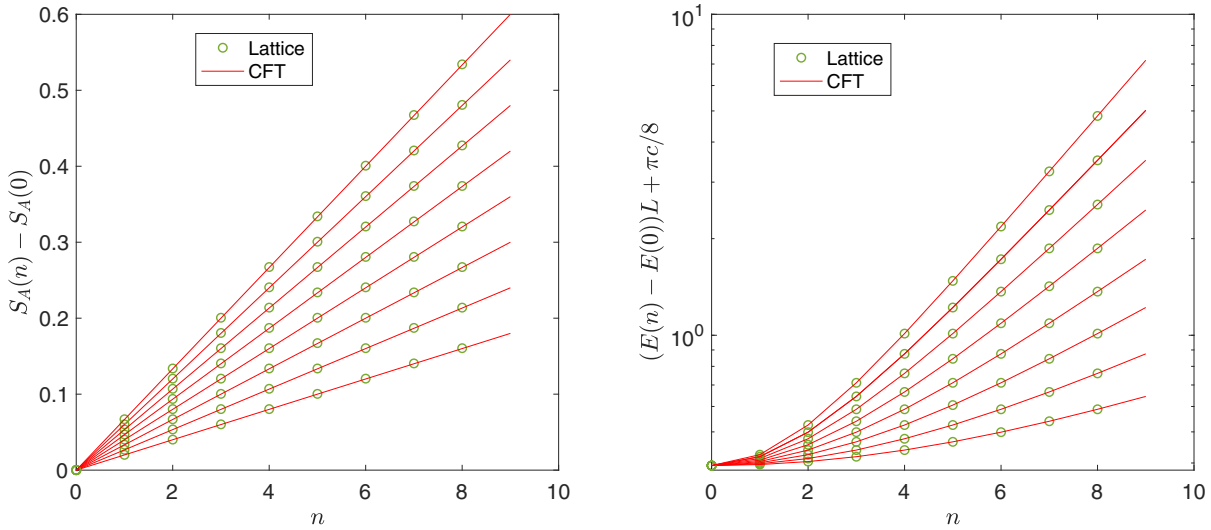

FIG. 9. Comparison of the CFT and lattice calculations on the entanglement entropy (left) and the total energy (right) evolution in the heating phase of a periodically driven CFT. The CFT is periodical driving with H_0 and H_θ with time intervals $T_0 = L/2$ and $T_1 = L_{\text{eff}}(\theta)/2$, respectively. From bottom to top, we choose $\theta = 0.03$, 0.04, 0.05, 0.06, 0.07, 0.08, 0.09, and 0.1. The CFT results are plotted according to Eq. (83).

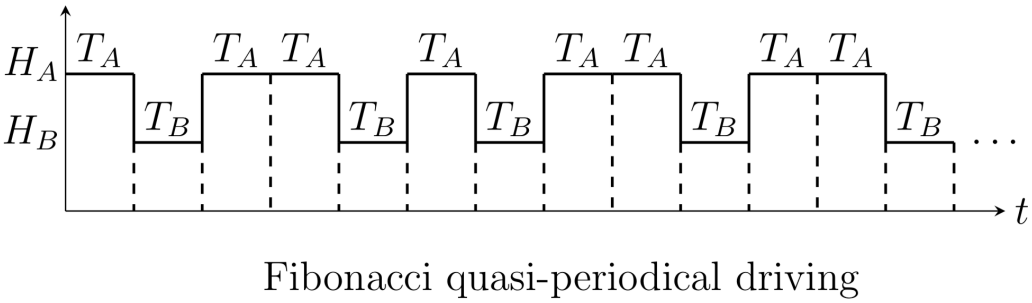

FIG. 10. A Fibonacci driving is generated by two unitaries $U_A = e^{-iH_A T_A}$ and $U_B = e^{-iH_B T_B}$ following the pattern of the Fibonacci bitstring 10110101 . . . .

Fibonacci Hamiltonian is a Cantor set of zero Lebesgue measure [68–70]. Since then, the Fibonacci dynamics has been extensively studied in both physics and mathematics. See, e.g., Ref. [72] for a recent review. For simplicity, in the following we may call the quasiperiodically driven CFT with a Fibonacci sequence as a Fibonacci driven CFT.

In the end of this section, we also discuss another kind of quasiperiodic driving with Aubry-André–type sequence by focusing on the properties of its phase diagram.

A. Fibonacci driving and relation to quasicrystal

We start with an introduction to the setup and tools we use to analyze the Fibonacci driving, many of which are borrowed from the rich literature of Fibonacci quasicrystals.

1. Setup and trace map

A Fibonacci driving in this paper is generated by two unitaries $U_A = e^{-iH_A T_A}$ and $U_B = e^{-iH_B T_B}$ following the pattern of the Fibonacci bitstring $\{X_j\}$ defined in Appendix B (see Fig. 10):

$$X_{j=1,2,3\ldots} = 10110101\ldots. \tag{87}$$

The Hamiltonians H_A, H_B are chosen to be the SL_2 deformed Hamiltonian same as the ones used in the previous sections. Therefore, each unitary $U_{A(B)}$ corresponds to a conformal map $M_{A(B)} \in SU(1,1)$ and the final conformal map Π_n that determines the operator evolution is given as a product

$$\Pi_n = \prod_{j=1}^{n} M_j, \quad M_j = X_j M_A + (1 - X_j) M_B. \tag{88}$$

For example, the first few matrices

$$\Pi_n = M_A M_B M_A M_A M_B M_A M_B M_A \ldots. \tag{89}$$

A useful property of the Fibonacci driving Π_n is that for n being a Fibonacci number[16] F_k with $k \geqslant 3$ there is a recurrence relation for its trace

$$\begin{aligned} x_{F_{k+1}} &= 2x_{F_k} x_{F_{k-1}} - x_{F_{k-2}}, \quad \text{where} \quad x_{F_k} = \tfrac{1}{2}\operatorname{Tr}(\Pi_{F_k}) \\ &= \tfrac{1}{2}\operatorname{Tr}\left(\Pi_{F_k}^{-1}\right). \end{aligned} \tag{90}$$

[16]Our convention for the Fibonacci number is that $F_k = F_{k-1} + F_{k-2}$, $F_1 = F_0 = 1$.

This relation was used in quasicrystal literature, e.g., see Ref. [68]. Also see Appendix B for a derivation following the substitution rule of the Fibonacci bit string and the property that $\det \Pi_n = 1$.

The initial conditions for this recurrence relation can be taken as

$$\begin{aligned} x_{F_1} &= \tfrac{1}{2}\operatorname{Tr}(M_A), \quad x_{F_2} = \tfrac{1}{2}\operatorname{Tr}(M_A M_B), \\ x_{F_3} &= \tfrac{1}{2}\operatorname{Tr}(M_A M_B M_A). \end{aligned} \tag{91}$$

It is sometime convenient to define an auxiliary $x_{F_0} = \frac{1}{2}\operatorname{Tr}(M_B)$ regarded as a different element from x_{F_1} although $F_0 = F_1 = 1$. The auxiliary element x_{F_0} is defined such that the recurrence relation (90) also holds for $k = 2$.

For SU(1,1) matrices, we have $x_{F_k} \in \mathbb{R}$. To visualize the trace map, let us introduce a three-dimensional vector $(x_{F_k}, y_{F_k}, z_{F_k}) := (x_{F_k}, x_{F_{k-1}}, x_{F_{k-2}})$, then the trace map in (90) can be expressed as the following mapping between points in three dimensional space:

$$\boxed{T : \mathbb{R}^3 \to \mathbb{R}^3, \; T(x_{F_k}, y_{F_k}, z_{F_k}) = (2x_{F_k} y_{F_k} - z_{F_k}, x_{F_k}, y_{F_k}),} \tag{92}$$

with the initial condition $l = (x_{F_3}, x_{F_2}, x_{F_1})$ given in Eq. (91) or, alternatively, we can use $(x_{F_2}, x_{F_1}, x_{F_0})$ with the auxiliary element x_{F_0}. Remarkably, the trace map has a constant of motion [68]

$$\boxed{I = -1 + x_{F_k}^2 + y_{F_k}^2 + z_{F_k}^2 - 2x_{F_k} y_{F_k} z_{F_k}} \tag{93}$$

(see Appendix B for an explicit check that I is independent of k).

2. Example with H_θ and fixed point

Let us now take the explicit example of SL_2 deformed driving Hamiltonians. Consider $(H_A, T_A) = (H_\theta, T_1)$ and $(H_B, T_B) = (H_0, T_0)$, where H_0 is taken as the CFT Hamiltonian with a uniform Hamiltonian density, and H_θ is taken as the SL_2 deformed one in Eq. (71):

$$H_\theta = \int_0^L \left(1 - \tanh(2\theta)\cos\frac{2\pi x}{L}\right) T_{00}(x)\,dx, \quad \theta > 0. \tag{94}$$

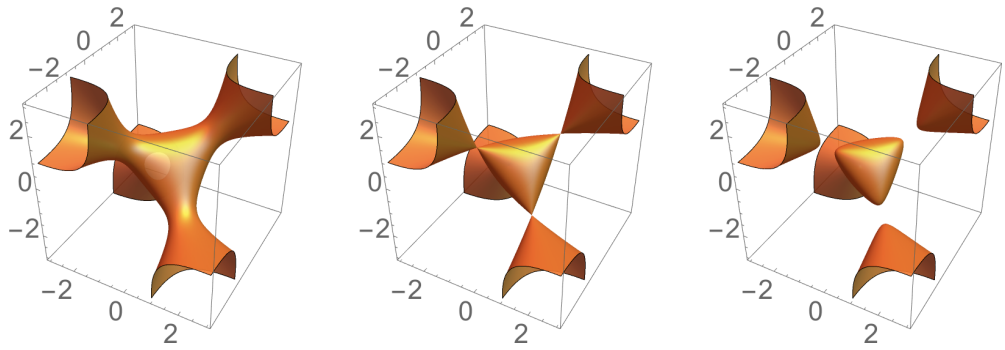

FIG. 11. Two-dimensional manifolds $\mathcal{M}$ determined by Eq. (93), with $I = 0.5$, 0, and -0.1, respectively. The manifold with $I = 0$ is called the Cayley cubic.

The corresponding conformal transformation M_A and M_B has been computed in (72) and copied here:

$$M(H_\theta, T_\theta) = \begin{pmatrix} \alpha & \beta \\ \beta^* & \alpha^* \end{pmatrix} \quad \text{with} \quad \times \begin{cases} \alpha = \cos\left(\frac{\pi T_\theta}{L_{\text{eff}}}\right) + i\cosh(2\theta)\sin\left(\frac{\pi T_\theta}{L_{\text{eff}}}\right), \\ \beta = -i\sinh(2\theta)\sin\left(\frac{\pi T_\theta}{L_{\text{eff}}}\right). \end{cases} \tag{95}$$

And $L_{\text{eff}} = L\cosh(2\theta)$ denotes the effective length of the system under H_θ. Therefore, the initial condition for the trace map is given as follows:

$$\begin{aligned} x_{F_0} &= \cos\left(\frac{\pi T_0}{L}\right), \quad x_{F_1} = \cos\left(\frac{\pi T_1}{L_{\text{eff}}}\right), \\ x_{F_2} &= \cos\left(\frac{\pi T_1}{L_{\text{eff}}}\right)\cos\left(\frac{\pi T_0}{L}\right) \\ &\quad - \cosh(2\theta)\sin\left(\frac{\pi T_1}{L_{\text{eff}}}\right)\sin\left(\frac{\pi T_0}{L}\right). \end{aligned} \tag{96}$$

The invariant I defined in (93) is

$$\begin{aligned} I &= [\cosh^2(2\theta) - 1]\sin^2\left(\frac{\pi T_0}{L}\right)\sin^2\left(\frac{\pi T_1}{L_{\text{eff}}}\right) \\ &\in [0, \cosh^2(2\theta) - 1]. \end{aligned} \tag{97}$$

Generally speaking, the invariant I constrains the motion of $(x_{F_k}, y_{F_k}, z_{F_k})$ on a two-dimensional manifold $\mathcal{M}$. For $I \in \mathbb{R}$, there are three topologically distinct scenario as shown in Fig. 11:

(1) $I = 0$: The manifold $\mathcal{M}$ can be decomposed into five parts. The central part is the curvilinear tetrahedral ("island"), with the vertices and singularities at $A\,(1, 1, 1)$, $B\,(1, -1, -1)$, $C\,(-1, 1, -1)$, and $D\,(-1, -1, 1)$. The tetrahedral is parametrized by θ_1 and θ_2 with $x = \cos(\theta_1 + \theta_2)$, $y = \cos\theta_1$, $z = \cos\theta_2$. The left four parts are funnels. The first funnel is parametrized by $x = \cosh(\theta_1 + \theta_2)$, $y = \cosh\theta_1$, and $z = \cosh\theta_2$, with its vertex at the point A. The other three funnels are similar defined with the vertices at B, C, and D. In the Fibonacci driven CFT, this case corresponds to $T_0/L \in \mathbb{Z}$ or $T_1/L_{\text{eff}} \in \mathbb{Z}$. Physically, this corresponds to a single quantum quench which is not our focus here.

(2) $I > 0$: The four vertices A, B, C, and D are replaced with four necks, which connect the central part ("island") of the manifold to the four funnels. The whole manifold is therefore noncompact. This case corresponds to all the nontrivial choices of (T_0, T_1) in our setting (97). It turns out that for almost all the initial points on the manifold, they will flow to infinity under the trace map in (90) [67].

(3) $I < 0$: The central part ("island") becomes disconnected to the outside funnels and therefore compacted. This case is absent in our setting for the Fibonacci driving. Nevertheless, this case may be related to some non-Hermitian Hamiltonian or nonunitary time evolution and deserves a careful study in the future.

For a fixed $I > 0$, one can tune two of the three parameters (θ, T_0, T_1) to move the initial point $(x_{F_3}, x_{F_2}, x_{F_1})$ on the surface $\mathcal{M}$, then the orbit under the trace map

$$T\left(x_{F_k},\, y_{F_k},\, z_{F_k}\right) = \left(2x_{F_k}y_{F_k} - z_{F_k},\, x_{F_k},\, y_{F_k}\right) \tag{98}$$

is completely determined. As we will show in the following sections, most of the orbits will escape to the infinity and resulting heating phase. However, there still exists returning orbit, e.g., when we have two zeros in the initial condition $(x_{F_3}, x_{F_2}, x_{F_1})$, we will end up with a period-6 orbits

$$\begin{aligned} (0, 0, a) \to (-a, 0, 0) \to (0, -a, 0) \to (0, 0, -a) \to (a, 0, 0) \\ \to (0, a, 0) \to (0, 0, a) \to \cdots \end{aligned} \tag{99}$$

with $a = (1 + I)^{1/2}$ (see Fig. 12 for an illustration). We will call such initial points that correspond to the nonheating point as "fixed point," in the sense that those points are fixed under T^6 action.

3. Phase diagram: From periodic to quasiperiodical driving

In this section, we show the shape of the phase diagram of a Fibonacci driven CFT via numerically approaching the Fibonacci bit string by its finite truncation. This strategy has been proven useful in the analysis of the energy spectrum of a Fibonacci quasicrystal [68]. In the quasicrystal case, the energy spectrum forms a Cantor set of zero Lebesque measure. In this section, we will show numerical evidence of such "fractal" structure, while in the next section we will map our phase diagram to the energy spectrum of quasicrystal and establish the claim.

Recall that (in Appendix B) we generate the Fibonacci driving using the Fibonacci bit string

$$X_j = \chi((j-1)\omega), \quad j = 1, 2, 3\ldots, \tag{100}$$

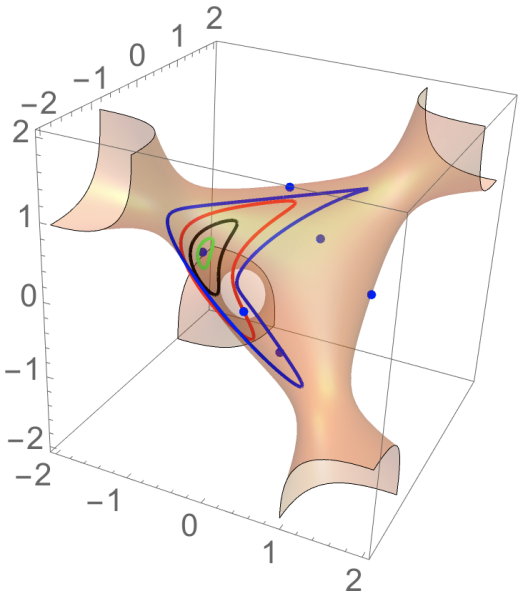

FIG. 12. Return orbits and initial conditions: here we plot $\mathcal{M}$ with $I = \frac{1}{4}$ fixed. The right plot is the same as the left one with a different angle of view. The six blue solid dots correspond to the period-6 returning orbit or equivalently speaking the fixed points of T^6 action. This orbit can be viewed as the limit of a family of initial conditions: for each fixed θ, the allowed initial condition forms a line [two parameters T_0, T_1 with one constraint (97)]. In the figure, we set $\theta = 1$, 0.4, 0.27, and 0.245 for four loops from big to small. Then, if we further decrease θ to a critical value θ^* such that $I = \cosh^2(2\theta^*) - 1$, then we have essentially only one possible initial condition $T_0 = L/2$ and $T_1 = L_{\text{eff}}/2$ which will generate the fixed points.

where $\chi(t) = \chi(t+1)$ is a period-1 characteristic function

$$\chi(t) = \begin{cases} 1, & -\omega^3 \leqslant t < \omega^2 \\ 0, & \omega^2 \leqslant t < 1 - \omega^3 \end{cases} \tag{101}$$

and $\omega = \frac{\sqrt{5}-1}{2}$ is an irrational number with a simple continued fraction representation

$$\omega = \frac{1}{1 + \frac{1}{1 + \frac{1}{1+\cdots}}}. \tag{102}$$

Now, to approach the Fibonacci bit string from a periodic string, we can truncate the continued fraction of ω at finite order n and obtain a rational number (principal convergent) $\omega_n = F_{n-1}/F_n$, namely, the ratio of two nearby Fibonacci numbers. The corresponding bit string $\{X_j\}$ now has periodicity F_n and therefore produces a periodic driving. We can now use the tools introduced in Sec. IV to obtain a phase diagram for each ω_n.

In Fig. 13, we show the evolution of phase diagrams of periodically driven CFTs with protocol $(H_A, T_A) = (H_{\theta=\infty}, T_1)$ and $(H_B, T_B) = (H_0, T_0)$. The phase diagram is periodic in T_0 direction with period L; we only show the phase diagram within one unit cell $0 \leqslant T_0 \leqslant L$. As we increase n, there are two notable features:

(1) The number of regions of the nonheating phases increases with n, and tends to infinity as $n \to \infty$.

(2) The measure of the nonheating phases decreases with n, and tends to zero as $n \to \infty$.

These two features suggest that the nonheating phases in the quasiperiodical driving limit may form a Cantor set of measure zero, analogous to the feature of the energy spectrum in a Fibonacci quasicrystal. In fact, this is indeed the case, as we will discuss in detail in the next subsection.

We also present the evolution of phase diagrams by the Hamiltonians H_0 and H_θ with finite θ. See Fig. 14 for $\theta = 0.5$, and Fig. 39 in the Appendix for $\theta = 0.2$. The two features mentioned above are also observed in these cases. It is noted that for a finite θ in $H_1(\theta)$, the phase diagram is also periodic in the T_1 direction, with the period $L\cosh(2\theta)$.

4. Exact mapping from a Fibonacci driven CFT to a Fibonacci quasicrystal

The features in the phase diagrams in Figs. 13 and 14 suggest that the nonheating phases in the quasiperiodical driving limit may form a Cantor set of measure zero. In this section, we verify this by performing an exact mapping between the phase diagram of a Fibonacci driven CFT and the energy spectrum of a Fibonacci quasicrystal. The latter has been proved mathematically that the energy spectrum is indeed a Cantor set [70] (see also Ref. [67] for a review).

Before introducing the mapping, let us first briefly review the background of the Fibonacci quasicrystal. We consider the discrete Schrödinger operators of the form

$$[H\psi]_j = \psi_{j+1} + \psi_{j-1} + V_j\psi_j, \quad j \in \mathbb{Z} \tag{103}$$

where $\psi_j := \langle j|\psi\rangle$ is the position-space wave function, with j labeling the jth site, and V_j is the onsite potential. For eigenvalue problem $H\psi = E\psi$, it is useful to consider the transfer matrix

$$T_j = \begin{pmatrix} E - V_j & -1 \\ 1 & 0 \end{pmatrix} \in \text{SL}(2, \mathbb{R}). \tag{104}$$

Denoting $\Psi_j = (\psi_{j+1}, \psi_j)^T$, we have[17]

$$\Psi_n = (T_n \ldots T_2 T_1)\Psi_0. \tag{105}$$

In the Fibonacci quasicrystal, the potential V_j can also be generated by the Fibonacci bit string $\{X_j\}$ (B1) as follows:

$$V_j = X_j V_A + (1 - X_j)V_B. \tag{106}$$

The allowed energy spectrum E is determined by requiring that

$$\lambda_L := \lim_{n\to\infty} \frac{1}{n} ||T_n \ldots T_1|| = 0. \tag{107}$$

Defining $\widetilde{T}_{F_n} := T_{F_n} T_{F_n-1} \ldots T_1$, and $x_{F_n} := \frac{1}{2}\text{Tr}(\widetilde{T}_{F_n})$, it turns out the traces $\{x_{F_n}\}$ satisfy the same recurrence relation in Eq. (90). The only difference between the Fibonacci driving CFTs and the Fibonacci quasicrystals is the initial conditions, which we will specify now. By taking $V_B = -V_A = V$, one can

[17] It is helpful to compare this equation with Eqs. (5) and (23) in the time-dependent driving CFT. In Eq. (23), the $\text{SU}(1,1) \simeq \text{SL}(2,\mathbb{R})$ matrix M_j may be considered as a transfer matrix in time direction.

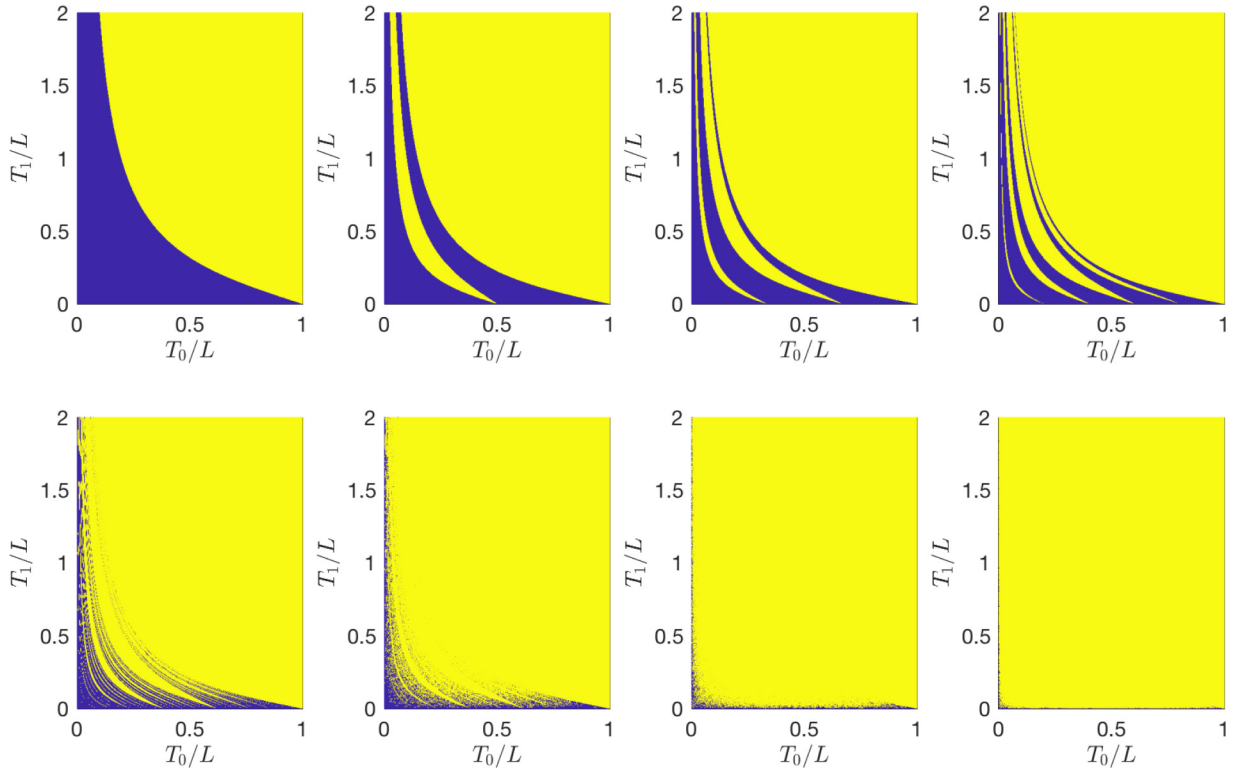

FIG. 13. Phase diagrams in a periodically driven CFT with the sequence generated by finitely truncated Fibonacci bit string, i.e., $\{X_j\}$ with $\omega_n = F_{n-1}/F_n$. Here we choose $n = 2$, 4, 5, 6, 10, 20, 100, and 1000 for eight plots, respectively. The two Hamiltonians we use are $H_0(\theta = 0)$ and $H_1(\theta = \infty)$ in (71). The blue (yellow) regions correspond to the heating (nonheating) phases.

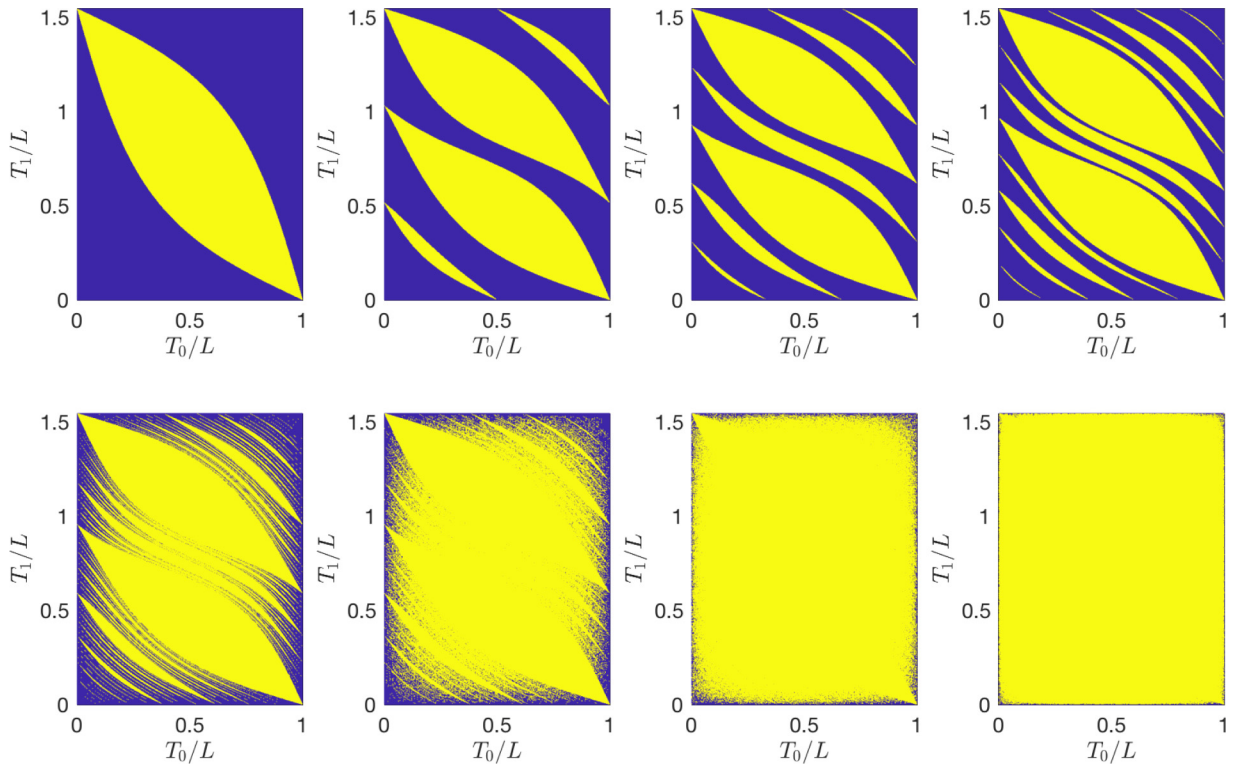

FIG. 14. Phase diagrams in a periodically driven CFT with the sequence generated by finitely truncated Fibonacci bit string, i.e., $\{X_j\}$ with $\omega_n = F_{n-1}/F_n$. Here we choose $n = 2$, 4, 5, 6, 10, 20, 100, and 1000 for eight plots, respectively. The two Hamiltonians we use are $H_0(\theta = 0)$ and $H_1(\theta = 0.5)$ in (71). The phase diagram is periodic in the T_0 direction with period L and in the T_1 direction with period $L\cosh(2\theta) \simeq 1.54L$. The blue (yellow) regions correspond to the heating (nonheating) phases.

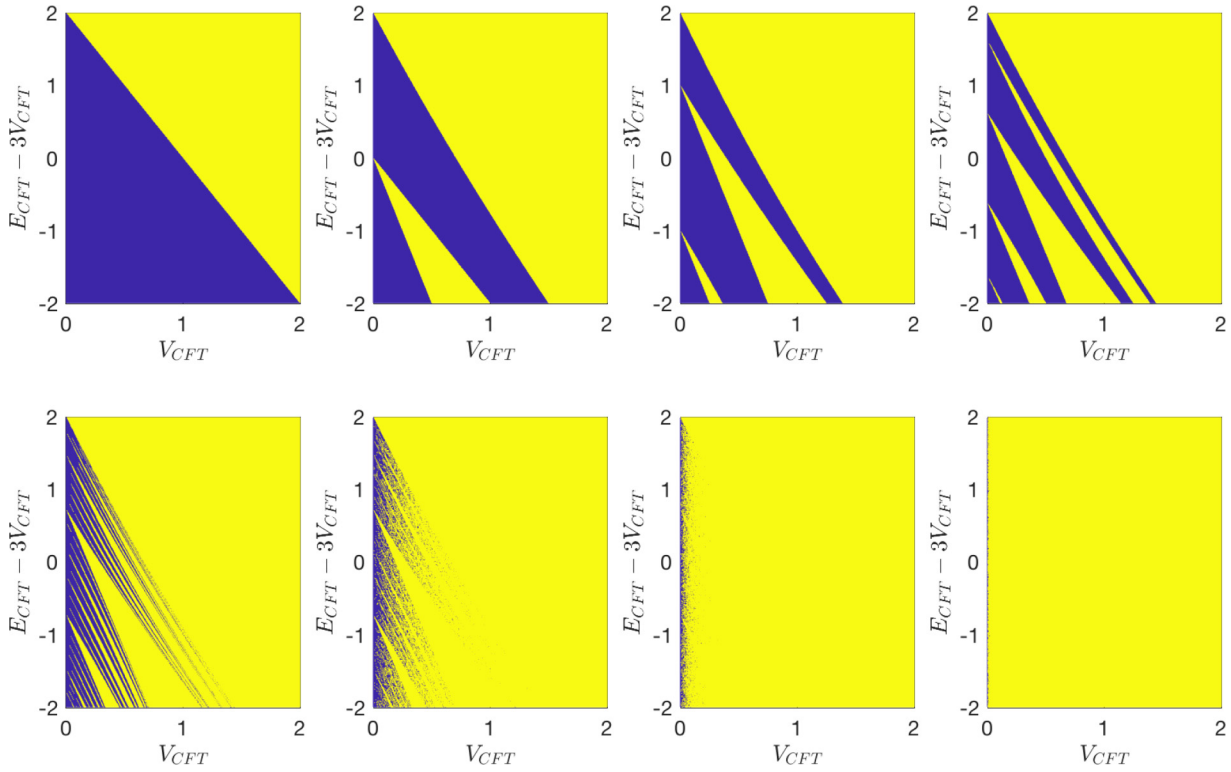

FIG. 15. Phase diagrams in a periodically driven CFT with the sequence chosen in (101) where $\omega_n = F_{n-1}/F_n$. The parameters are the same as those in Fig. 13 except that now we change the variables to $V_{\rm CFT}$ and $E_{\rm CFT}$ [see Eq. (112)]. The blue (yellow) regions correspond to the heating (nonheating) phases.

find the initial conditions for the Fibonacci quasicrystal are[18]

$$l_{(E;I)} := (x_{F_1}, x_{F_0}, x_{F_{-1}})_{\rm quasicrystal} = \left(\frac{E+V}{2}, \frac{E-V}{2}, 1\right), \quad \text{where} \quad E \in \mathbb{R}. \tag{108}$$

The invariant I in the constant of motion in Eq. (93) becomes $I = V^2$. In a quasicrystal, the potential V is fixed, and therefore each E specifies an initial condition, which may flow to infinity by iterating the trace map (E is in the gap) or is bounded (E is in the spectrum).

Next, let us compare the initial conditions in the Fibonacci driven CFT. We consider the phase diagrams in Fig. 13, which correspond to $H_0(\theta = 0)$ and $H_1(\theta = \infty)$. By taking the limit $\theta \to \infty$, the initial conditions in Eq. (96) become[19]

$$\left(x_{F_2}, x_{F_1}, x_{F_0}\right)_{\rm CFT} = \left(\cos\frac{\pi T_0}{L} - \frac{\pi T_1}{L}\sin\frac{\pi T_0}{L}, 1, \cos\frac{\pi T_0}{L}\right), \tag{109}$$

and the invariant I in Eq. (93) is

$$I = \left(\frac{\pi T_1}{L}\right)^2 \sin^2\left(\frac{\pi T_0}{L}\right). \tag{110}$$

To compare with the initial conditions of Fibonacci quasicrystal, here we choose $(x_{F_3}, x_{F_2}, x_{F_1})$ instead of $(x_{F_2}, x_{F_1}, x_{F_0})$ as the initial condition. Based on Eq. (90), one can obtain

$$\left(x_{F_3}, x_{F_2}, x_{F_1}\right)_{\rm CFT} = \left(\cos\frac{\pi T_0}{L} - 2\frac{\pi T_1}{L}\sin\frac{\pi T_0}{L}, \cos\frac{\pi T_0}{L} - \frac{\pi T_1}{L}\sin\frac{\pi T_0}{L}, 1\right). \tag{111}$$

Now by defining $E_{\rm CFT} := 2\cos\frac{\pi T_0}{L} + 3V_{\rm CFT}$, $V_{\rm CFT} := -\frac{\pi T_1}{L}\sin\frac{\pi T_0}{L}$, then the initial condition line can be written as

$$l_{(E_{\rm CFT};I)} := \left(x_{F_3}, x_{F_2}, x_{F_1}\right)_{\rm CFT} = \left(\frac{E_{\rm CFT}+V_{\rm CFT}}{2}, \frac{E_{\rm CFT}-V_{\rm CFT}}{2}, 1\right), \tag{112}$$

with the invariant I in Eq. (110) expressed as

$$I = V_{\rm CFT}^2. \tag{113}$$

That is, by redefining variables, we can find a map between the initial conditions in Eqs. (108) and (112). With this map, the allowed energy E in the spectrum of a Fibonacci quasicrystal is mapped to the nonheating phase in a Fibonacci driven CFT specified by $E_{\rm CFT}(T_0, T_1)$, and vice versa.

[18]Here we use the recurrence relation to infer the value of x_{F_0} and $x_{F_{-1}}$ from $(x_{F_3}, x_{F_2}, x_{F_1})$, the reason we choose to start with $x_{F_{-1}} = 1$ for quasicrystal is that we need a convenient base point to map to the CFT initial point, whose x_{F_1} happens to be 1 as well. It should be clear later when we construct the mapping.

[19]Note that by taking the limit $\theta \to \infty$, we always consider finite T_0 and T_1 such that $T_0,\ T_1 \ll L\cosh(2\theta)$ when $\theta \to \infty$. In this case, the initial conditions $(x_{F_2}, x_{F_1}, x_{F_0})_{\rm CFT}$ form a straight line with $y = 1$, rather than a closed loop in Fig. 12. See Fig. 16 for the initial conditions $(x_{F_3}, x_{F_2}, x_{F_1})_{\rm CFT}$ with $\theta = \infty$.

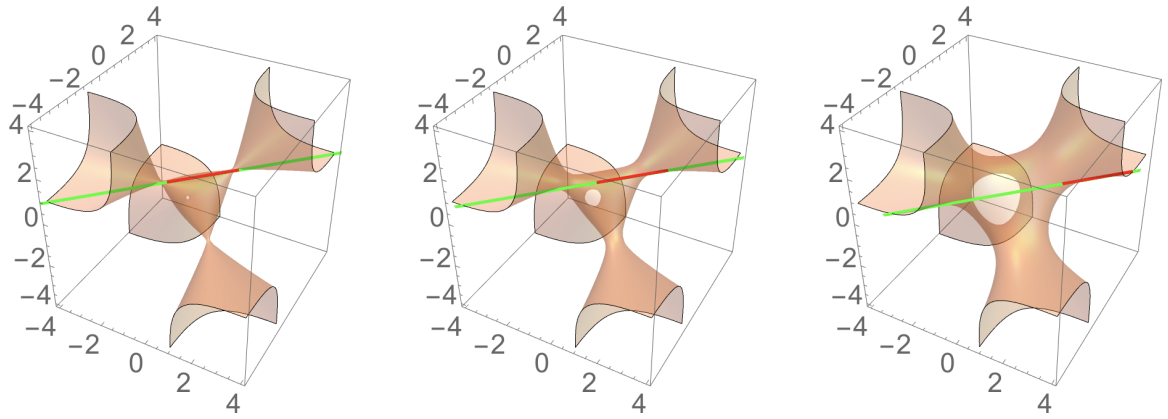

FIG. 16. Initial conditions in Eqs. (108) and (112) on the two-dimensional manifolds $\mathcal{M}$ determined by Eq. (93), with $I = V^2 = 0.1^2$, 0.5^2, and 1.5^2, respectively. The green solid lines correspond to the initial condition line $l_{(E,I)}$ in Eq. (108) for a quasicrystal, and the red solid lines correspond to $l_{(E_{\rm CFT};I)}$ of a fixed length 2 in Eq. (112) for a quasiperiodically driven CFT. For smaller I, $l_{(E_{\rm CFT};I)}$ overlaps with $l_{(E,I)}$ mainly in the region with $|x|$, $|y| \leqslant 1$, $z = 1$. As I increases, $l_{(E_{\rm CFT};I)}$ overlaps with $l_{(E,I)}$ mainly in the region with $|x|$, $|y| > 1$, $z = 1$. That is, as I increases, $l_{(E_{\rm CFT};I)}$ moves from the middle "island" into the noncompact funnel. This behavior agrees with the feature of the phase diagram in Fig. 15 where the nonheating phases vanish for larger $V_{\rm CFT}$.

One should note that, however, on the CFT side, $(E_{\rm CFT} - 3V_{\rm CFT}) \in [-2, 2]$ always lives in a window of finite width. On the quasicrystal side, we have $(E - 3V) \in (-\infty, +\infty)$. This means the nonheating phases in a quasiperiodically driven CFT are only mapped to *part* of the energy spectrum in the Fibonacci quasicrystal. This can be intuitively seen by considering the initial condition lines in Eqs. (108) and (112) on the two-dimensional manifold $\mathcal{M}$ determined by Eq. (93). As shown in Fig. 16, the overlap of $l_{(E_{\rm CFT};I)}$ and $l_{(E;I)}$ is always a straight line of finite length 2. For smaller V or $V_{\rm CFT}$, $l_{(E_{\rm CFT};I)}$ overlaps with $l_{(E;I)}$ mainly in the region with $|x|$, $|y| \leqslant 1$, $|z| = 1$ in the middle island. For the initial conditions in this region, they are much easier to be bounded as we iterate the trace map [73]. As V or $V_{\rm CFT}$ increases, the overlap of $l_{(E_{\rm CFT};I)}$ and $l_{(E;I)}$ moves gradually from the island in the middle to the funnel outside. Then, it becomes more difficult for the initial conditions to stay bounded as we iterate the trace map. This analysis agrees with the fact that in the phase diagrams in Fig. 15, there are no nonheating phases observed for large $V_{\rm CFT}$.

This "inclusion map" for small $V_{\rm CFT}$ is totally fine for our goal: Since the energy spectrum of a Fibonacci quasicrystal forms a Cantor set of measure zero, then *part* of the energy spectrum (which is a connected and finite region in the parameter space) is also a Cantor set of measure zero. Then with the exact mapping discussed above, we conclude that the nonheating phases in the quasiperiodically driven CFT form a Cantor set of measure zero.

Furthermore, in Fig. 17, we also check explicitly the measure of the nonheating phases in the phase diagrams in Fig. 15 as we approach the quasiperiodic limit. The procedure of obtaining the measure is as follows: Fixing a $V_{\rm CFT}$ (or equiva-

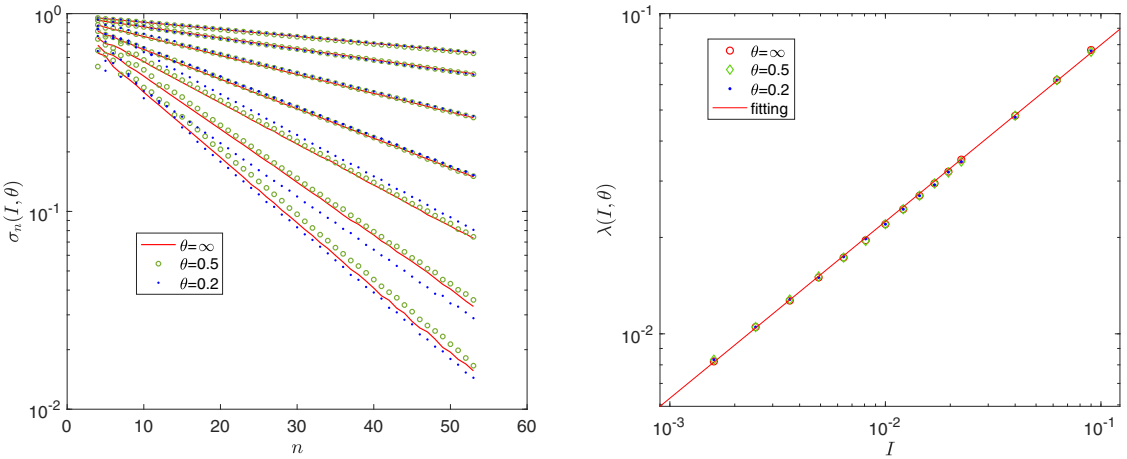

FIG. 17. Left: measure of the nonheating phases $\sigma_n(I, \theta)$ in the phase diagram in Figs. 15 ($\theta = \infty$), 18 ($\theta = 0.5$), and 40 ($\theta = 0.2$) as a function of n for different I. From top to bottom, we consider $I = 0.04^2$, 0.06^2, 0.1^2, 0.15^2, 0.2^2, 0.25^2, and 0.3^2, respectively. One can find that the measure is $\sigma_n(I) \propto e^{-\lambda(I,\theta)n}$, where n corresponds to the subscript in F_n. Right: the escape rate $\lambda(I, \theta)$ as a function of I. It is found that $\lambda(I, \theta)$ with different θ collapse to the same line described by $y = a\,x^b$, where $a \simeq 0.285$ and $b \simeq 0.552$.

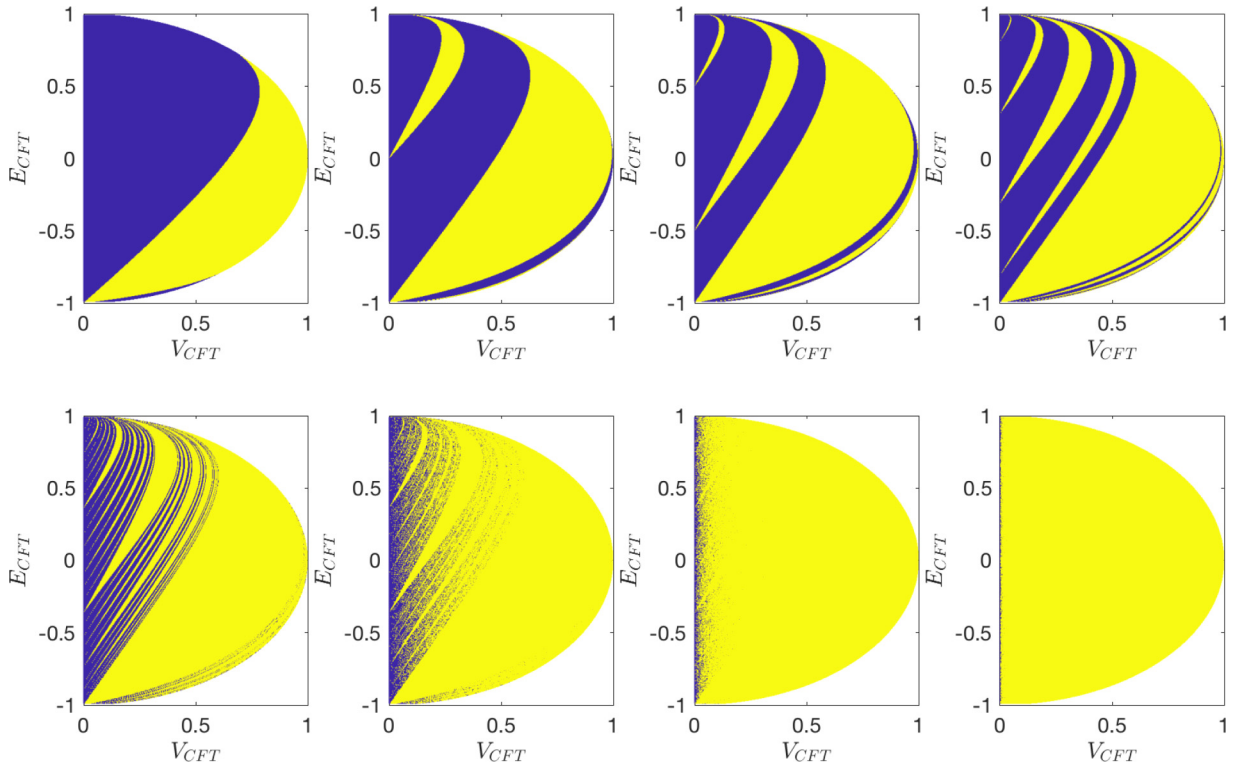

FIG. 18. Phase diagrams in a periodically driven CFT with the sequence generated by finitely truncated Fibonacci bit string, i.e., $\{X_j\}$ with $\omega_n = F_{n-1}/F_n$. The parameters are the same as those in Fig. 14 except that now we change the variables to $V_{\rm CFT}$ and $E_{\rm CFT}$ [see Eq. (112)]. The blue (yellow) regions correspond to the heating (nonheating) phases.

lently the invariant I) in Fig. 15, for each $\omega_n = F_{n-1}/F_n$, there are many "energy bands" of nonheating phases. Denoting the bandwidth of the jth band as $d_j(n)$, this bandwidth depends on both I and θ (which is ∞ here). Then the measure of nonheating phases with $\omega_n = F_{n-1}/F_n$ is defined as

$$\sigma_n(I,\theta) = \frac{\sum_j d_j(n,I,\theta)}{E_{\max}(n,I,\theta) - E_{\min}(n,I,\theta)}, \tag{114}$$

where $E_{\max}(n,I,\theta) - E_{\min}(n,I,\theta)$ is the total width of the energy window, which is 4 for $\theta = \infty$. As seen in Fig. 17 (left), it is found that $\sigma_n(I,\theta)$ depends on n as

$$\sigma_n(I,\theta) \propto e^{-\lambda(I,\theta)n}. \tag{115}$$

That is, the measure of the nonheating phases decreases exponentially as a function of n, and tends to become 0 in the limit $n \to \infty$. This agrees with the fact that the nonheating phases in the quasiperiodical driving limit form a Cantor set of *measure zero*. The decaying rate $\lambda(I,\theta)$ may also be interpreted as the escape rate since it describes the rate of initial conditions in Fig. 12 escaping into the infinity. Also, we remind here that the real driving steps are F_n rather than n. And $F_n \sim \omega^{-n}$ at $n \to \infty$, the measure of nonheating phases depends on F_n as $\sigma_n(I,\theta) \propto F_n^{\lambda(I,\theta)/\log\omega}$ for large n. That is, $\sigma_n(I,\theta)$ decays polynomially as a function of the driving steps F_n. In addition, we check how the decaying rate $\lambda(I,\theta)$ depends on the invariant I. As shown in Fig. 17 (right), it is found that $\lambda(I,\theta)$ depends on I as $\lambda(I,\theta=\infty) = aI^b$, with $a \simeq 0.285$ and $b \simeq 0.552$. This monotonic dependence is reasonable in the sense that a smaller I corresponds to a narrower neck connecting the island and "funnel" (see Figs. 11 and 16), which may suppress the escape rate from the island to the funnel.

5. *Cases that cannot be mapped to Fibonacci quasicrystal*

The exact mapping studied in the previous subsection applies for the case of $\theta \to \infty$ in $H_1(\theta)$. For a finite θ, we do not have such an exact mapping. Here we hope to study the common features among the phase diagrams with different θ (see, e.g., the phase diagrams in Figs. 13 and 14, and 39 in the Appendix).

As analyzed in the previous subsections, to study the measure of the nonheating phases or the escape rate of initial conditions to infinity on the manifold $\mathcal{M}$ (see Fig. 12), it is more appropriate to fix the invariant I in Eq. (93). This is because the trace map in Eqs. (90) or (92) holds for a fixed invariant I. In other words, the points $(x_{F_n}, y_{F_n}, z_{F_n})$ in Eq. (92) move on the manifold $\mathcal{M}$ with a fixed geometry. For this reason, we can replot the phase diagram in Fig. 14 by changing variables in the initial conditions in Eq. (96) as follows:

$$V_{\rm CFT} := \sin\left(\frac{\pi T_1}{L_{\rm eff}}\right)\sin\left(\frac{\pi T_0}{L}\right), \quad E_{\rm CFT} = \cos\frac{\pi T_0}{L}, \tag{116}$$

where $L_{\rm eff} = L\cosh(2\theta)$ with the invariant

$$I = [\cosh^2(2\theta) - 1]V_{\rm CFT}^2. \tag{117}$$

With the above procedure, now we map the phase diagram in the region $\{(T_0, T_1)|0 \leqslant T_0/L \leqslant 1, 0 \leqslant T_1/L_{\rm eff} < 1/2\}$ in

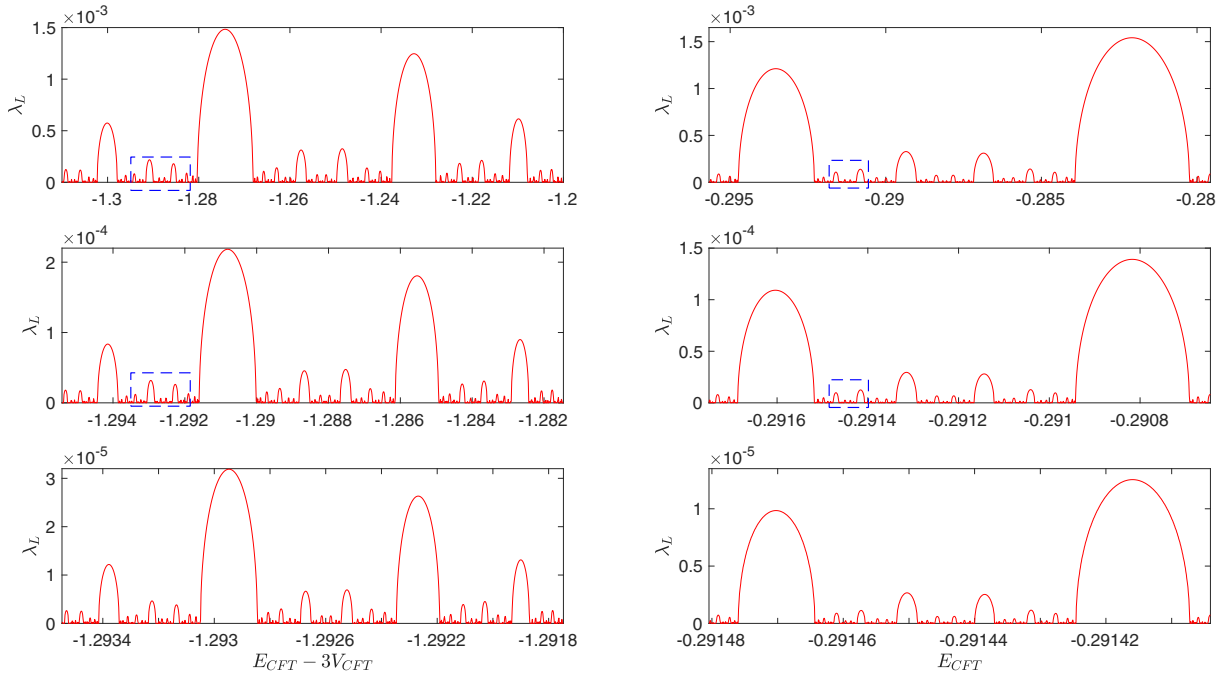

FIG. 19. Self-similarity in the distribution of Lyapunov exponents along E_{CFT} in Figs. 15 and 18. Left: the CFT is driven by H_0 and $H_{\theta=\infty}$. We fix $I = V_{\mathrm{CFT}}^2 = 0.3^2$, and scan the Lyapunov exponents along $E_{\mathrm{CFT}} - 3V_{\mathrm{CFT}}$. Right: the CFT is driven by H_0 and $H_{\theta=0.5}$. We fix $I = [\cosh^2(2\theta) - 1]V_{\mathrm{CFT}}^2 = 0.3^2$ and scan the Lyapunov exponents along E_{CFT}. Each curve in the lower panel is the zoom-in plot of the region in blue dashes in the upper panel. We choose $n = 1000$ in $\omega_n = F_{n-1}/F_n$ here.

Figs. 14 to 18. The merit of this mapping is that for each V_{CFT} in Fig. 18, the invariant I is fixed. Then we study the measure of the nonheating phases as defined in Eq. (114), with the result shown in Fig. 17. There are two interesting features:

(1) Similar to the case of $\theta = \infty$, the measure of the nonheating phases depends on n as $\sigma_n(I, \theta) \propto e^{-\lambda(I,\theta)n}$. That is, the measure of the nonheating phases decays exponentially (power law) as a function of n (F_n), indicating that the

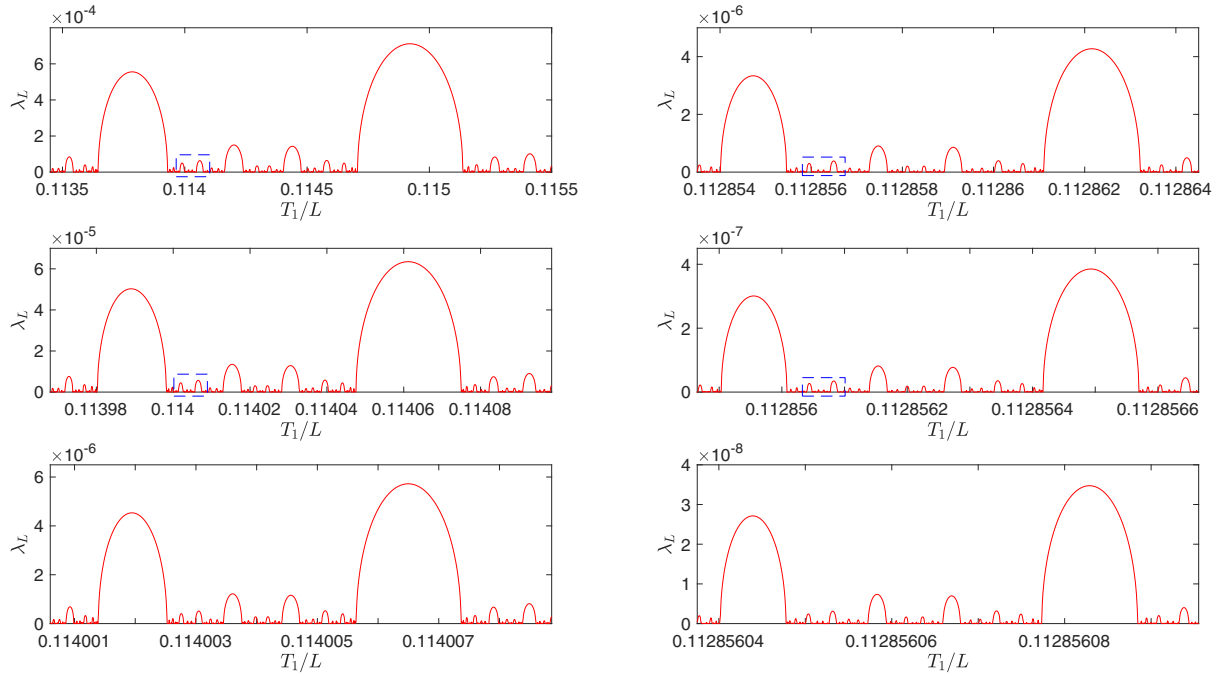

FIG. 20. Self-similarity in the distribution of Lyapunov exponents along T_1/L in Figs. 13 and 14. The CFT is driven by H_0 and $H_{\theta=\infty}$ (left), and H_0 and $H_{\theta=0.5}$ (right). Fixing $T_0/L = \frac{1}{2}$, we scan the Lyapunov exponents along T_1/L. Each curve in the lower panel is the zoom-in plot of the region in blue dashes in the upper panel. We choose $n = 1000$ in $\omega_n = F_{n-1}/F_n$ here.

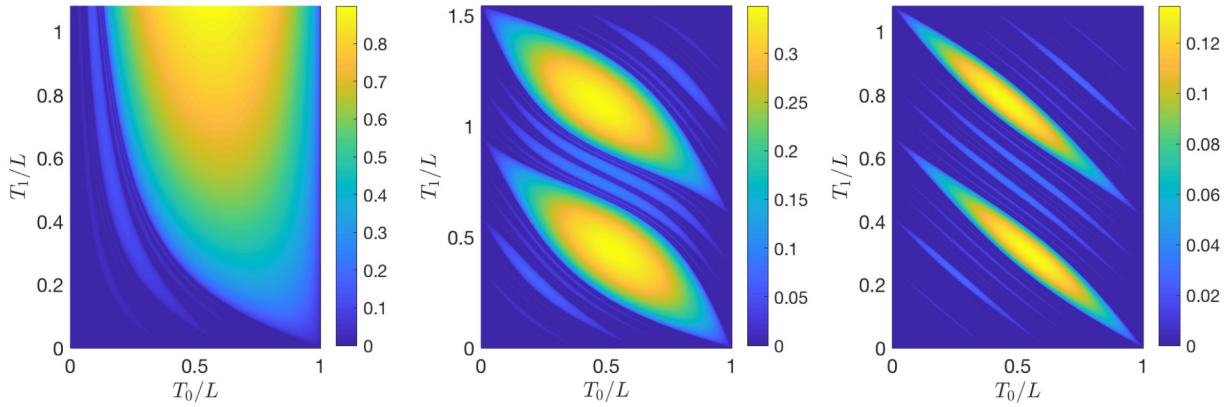

FIG. 21. Lyapunov exponents as a function of T_0/L and T_1/L for different choices of drivings (from left to right): H_0 and $H_{\theta=\infty}$, H_0 and $H_{\theta=0.5}$, H_0 and $H_{\theta=0.2}$. The Lyapunov exponents are obtained by choosing $\omega_n = F_{n-1}/F_n$ in Eq. (118), with $n = 1000$.

measure will become zero in the quasiperiodical driving limit $n = \infty$.

(2) Interestingly, the decay rate (or escape rate) $\lambda(I, \theta)$ for $\theta = 0.5$ and ∞ collapse to the same curve with $\lambda_I = aI^b$, where $b \simeq 0.552$ (see the right plot in Fig. 17). This means $\lambda(I, \theta)$ is only a function of I, and is independent of θ.

In addition, in Fig. 17, we also present the results for the measure of nonheating phases for the case of $\theta = 0.2$ (see Figs. 39 and 40 for the corresponding phase diagrams). The decaying rates $\lambda(I, \theta = 0.2)$ as a function of I again fall on the same curves as that of $\theta = 0.5$ and ∞, as seen in Fig. 17 (right plot). This means the decay rate $\lambda(I, \theta)$ is only a function of the invariant I, but is independent of θ which characterizes the concrete deformation of Hamiltonians.

6. *Lyapunov exponents in the quasiperiodical driving limit*

The phase diagrams as studied in the previous subsections simply tell us whether the CFT is in the heating or nonheating phases. As $n \to \infty$, the measure of the nonheating phases becomes zero, and one can only "see" the heating phase in the phase diagram. In this section, we will use Lyapunov exponents to further characterize the fine structures in the heating phases in the limit $n \to \infty$.

Let us first consider a periodical driving with $\omega = \omega_n = F_{n-1}/F_n$ in Eq. (101), where the period of driving is F_n. The Lyapunov exponent in the heating phase can be obtained via Eq. (60) as

$$\lambda_L(\omega_n) = \frac{1}{F_n} \log\left(|x_{F_n}| + \sqrt{|x_{F_n}|^2 - 1}\right), \qquad (118)$$

where $x_{F_n} = \frac{1}{2}\mathrm{Tr}(\Pi_{F_n})$ can be efficiently computed using the recurrence relation.

Now, we consider the distribution of Lyapunov exponents in Fig. 15 in the quasiperiodical driving limit. To be concrete, we fix V_{CFT} (or equivalently I) in Fig. 15, and scan the Lyapunov exponents along E_{CFT}. As shown in Fig. 19, it is found that the Lyapunov exponents exhibit self-similarity structures. That is, by zooming in the distribution of Lyapunov exponents, one can find the same distributions (in different scales). One can zoom in the distribution all the way and see the self-similarity structure, as long as a large enough n is taken. The self-similarity structure of Lyapunov exponents also indicates that the Lyapunov exponents can be arbitrarily small. In other words, in the heating phases of a Fibonacci quasiperiodic driving CFT, there exist some regions with arbitrary small heating rates for the entanglement and energy growth.

We also study the distribution of Lypunov exponents in the T_0/T_1 parameter space in Figs. 13 and 14. As shown in Fig. 20 are the distributions of λ_L along T_1/L with a fixed T_0/L. Interestingly, although the constant of motion I in Eq. (93) varies along T_1/L (with T_0/L fixed), the self-similarity structures in λ_L are still there.

At last, in Fig. 21, we give a color plot of the distribution of Lyapunov exponents in the parameter space $(T_0/L, T_1/L)$. One can find the patterns inherit some features of the periodically driven CFTs (see Fig. 7). It is also helpful to compare these three plots with the phase diagrams in Figs. 13, 14, and 39, respectively. We emphasize that although there are large areas of regions with almost zero Lyapunov exponents, they are actually in the heating phase (see Figs. 13, 14, and 39). If we zoom in these regions, one can observe the self-similarity structure (see, e.g., Figs. 19 and 20).

B. Fixed point in the nonheating phase: Entanglement and energy dynamics

From the previous discussions, we conclude that the measure of the nonheating phases shrinks to zero when we approach the quasiperiodical driving limit, i.e., without special guide it is hard to find the exact location of the nonheating point. Indeed, for the case with SSD deformation, namely the driving protocol given by H_0 and $H_{\theta=\infty}$, we are not able to locate such points. Fortunately, for finite θ, we can use the fixed point discussed in Sec. V A 2 to pin down the nonheating point. More explicit, in this section, we will show the following:

(1) If both the driving Hamiltonians are chosen as elliptic types,[20] one can always find *exact* nonheating phases point.

[20]For example, all the Hamiltonians of the form in Eq. (71) with a finite θ are elliptic. See Appendix A.

(2) At these nonheating points, both the entanglement entropy and the energy evolution are of period 6 in Fibonacci index, i.e., $S_A(F_n) = S_A(F_{n+6})$ and $E(F_n) = E(F_{n+6})$. It is noted that although the entanglement entropy and energy are periodic functions at the Fibonacci numbers, they are not periodic at the non-Fibonacci numbers. See the following statement.

(3) The envelopes of the entanglement entropy and total energy will grow logarithmically and in a power law as a function of the driving steps n (not the Fibonacci index), respectively.

We will first illustrate the above statements with simple examples in the following discussions, and then prove them in Sec. V B 4.

1. Entanglement and energy evolution at Fibonacci numbers

In the following, we will study the exact nonheating fixed point and its properties with the simple choice of $H_A = H_\theta$ and $H_B = H_{\theta=0}$, where the form of H_θ is given in Eq. (71). The initial conditions for the trace map have been given in Eq. (96). By considering

$$T_0/L = T_1/L_{\text{eff}} = 1/2, \quad \text{where} \quad L_{\text{eff}} = L\cosh(2\theta), \tag{119}$$

the initial condition has the form

$$\left(x_{F_2}, x_{F_1}, x_{F_0}\right) = (-\cosh(2\theta), 0, 0), \tag{120}$$

which will start a fixed point with constant of motion $I = \cosh^2(2\theta) - 1$ under the trace map (92), i.e.,

$$T : (-a,0,0) \to (0,-a,0) \to (0,0,-a) \to (a,0,0) \to (0,a,0) \to (0,0,a) \to (-a,0,0) \to \cdots, \tag{121}$$

where $a := \cosh(2\theta)$. In fact, for this fixed point, not only the traces [recall $x_{F_k} = \frac{1}{2}\operatorname{Tr}(\Pi_{F_k})$] have periodicity $x_{F_k} = x_{F_{k+6}}$, the corresponding matrices themselves are also returning periodically:

$$\begin{aligned}
\Pi_{F_{6k+1}} &= i\begin{pmatrix} \cosh(2\theta) & -\sinh(2\theta) \\ \sinh(2\theta) & -\cosh(2\theta) \end{pmatrix}, \quad \Pi_{F_{6k+2}} = -\begin{pmatrix} \cosh(2\theta) & \sinh(2\theta) \\ \sinh(2\theta) & \cosh(2\theta) \end{pmatrix}, \\
\Pi_{F_{6k+3}} &= i\begin{pmatrix} -\cosh(4\theta) & \sinh(4\theta) \\ -\sinh(4\theta) & \cosh(4\theta) \end{pmatrix}, \quad \Pi_{F_{6k+4}} = i\begin{pmatrix} \cosh(2\theta) & -\sinh(2\theta) \\ \sinh(2\theta) & -\cosh(2\theta) \end{pmatrix}, \\
\Pi_{F_{6k+5}} &= \begin{pmatrix} \cosh(2\theta) & -\sinh(2\theta) \\ -\sinh(2\theta) & \cosh(2\theta) \end{pmatrix}, \quad \Pi_{F_{6k+6}} = i\begin{pmatrix} 1 & 0 \\ 0 & -1 \end{pmatrix}.
\end{aligned} \tag{122}$$

Thus, the time evolution of entanglement entropy of the half-system $A = [0, L/2]$ and the total energy at the Fibonacci numbers are

$$S_A(F_j) - S_A(0) = \begin{cases} \frac{2\theta c}{3}, & j = 6k+1 \\ -\frac{2\theta c}{3}, & j = 6k+2 \\ \frac{4\theta c}{3}, & j = 6k+3 \\ \frac{2\theta c}{3}, & j = 6k+4 \\ \frac{2\theta c}{3}, & j = 6k+5 \\ 0, & j = 6k+6 \end{cases}$$

$$E(F_j) = \begin{cases} \frac{\pi c}{8L}\cosh(4\theta) - \frac{\pi c}{6L}, & j = 6k+1 \\ \frac{\pi c}{8L}\cosh(4\theta) - \frac{\pi c}{6L}, & j = 6k+2 \\ \frac{\pi c}{8L}\cosh(8\theta) - \frac{\pi c}{6L}, & j = 6k+3 \\ \frac{\pi c}{8L}\cosh(4\theta) - \frac{\pi c}{6L}, & j = 6k+4 \\ \frac{\pi c}{8L}\cosh(4\theta) - \frac{\pi c}{6L}, & j = 6k+5 \\ \frac{\pi c}{8L} - \frac{\pi c}{6L}, & i = 6k+6 \end{cases} \tag{123}$$

where $S_A(0)$ denotes the entanglement entropy in the initial state (which is the ground state of $H_{\theta=0}$ here), and $E_{F_{6k}} = -\frac{\pi c}{24L}$ corresponds to the Casimir energy. Also, see Figs. 22 and 23 for examples with $c = 1$ and $\theta = 0.5$ and 0.2.

An interesting remark is that the special initial condition we choose that forms the fixed point are conformal maps that correspond to the "reflection matrix" [since we require the initial traces to vanish, see discussions near (77)]. Note, the product of two distinct reflections is hyperbolic, i.e., if we drive the system with periodic driving we will end up heating the system. However, what we present just now is that if we drive it in a Fibonacci pattern, they happen to return and form a nonheating point in the quasiperiodic driving phase diagram.

2. Entanglement and energy evolution at non-Fibonacci numbers

As shown in Figs. 22 and 23, between the Fibonacci numbers, the numerical simulation shows that entanglement and energy still increase for initial condition at fixed point. In the context of Fibonacci quasicrystal, it was found that the wave-function amplitude in the energy spectrum and some physical observables (e.g., the resistance) have a power-law growth as a function of the lattice site n [43,74–76]. In our setup, at the driving steps that are non-Fibonacci numbers, we expect the entanglement entropy or total energy also grows in a certain subexponential way.

Now we provide analytic understanding using the property of the Fibonacci driving protocol. The idea is that, for any integer n which can be written as a sum of distinct Fibonacci numbers,

$$n = \sum_{j=1}^{m} F_{k_j} \quad \text{with} \quad k_1 > k_2 > \cdots k_m \tag{124}$$

the corresponding conformal transformation matrix Π_n can be written as

$$\Pi_n = \Pi_{F_{k_1}} \Pi_{F_{k_2}} \ldots \Pi_{F_{k_m}}, \tag{125}$$

where each Π_{F_k} with Fibonacci number has been obtained in Eq. (122). In particular, we can find some simple sequence:

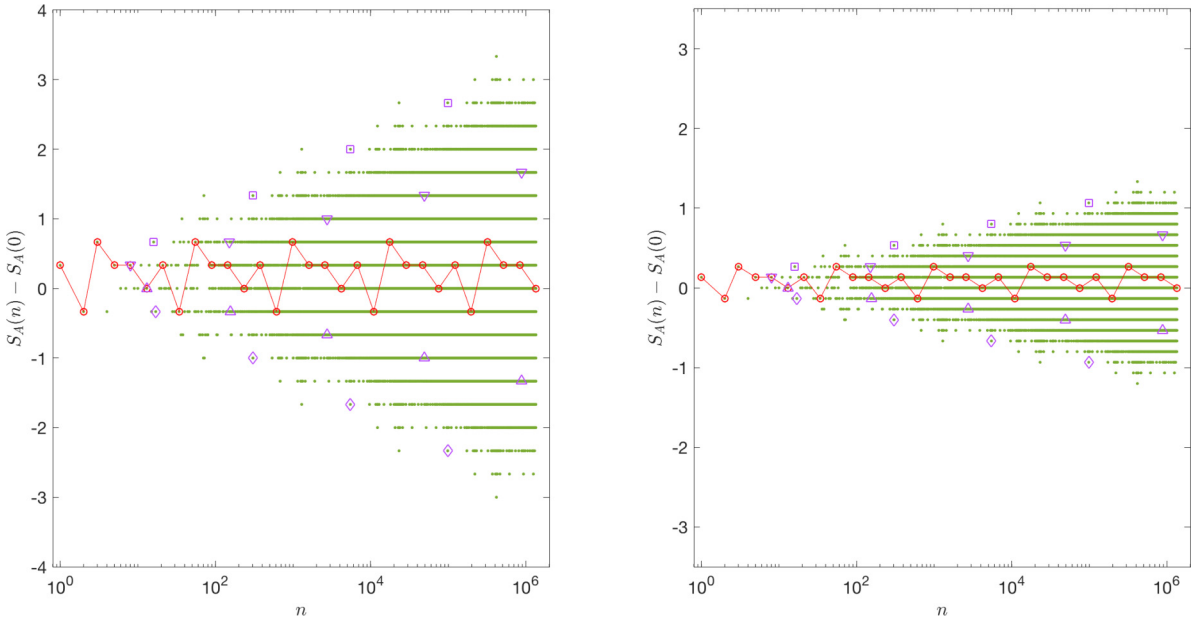

FIG. 22. Time evolution of the entanglement entropy of $A = [0,\ L/2]$ at the nonheating fixed point in Eq. (96) for $\theta = 0.5$ (left) and $\theta = 0.2$ (right). The red solid lines correspond to the entanglement entropy at the Fibonacci numbers $n = F_j$, with the expression given in Eq. (123), where we choose $c = 1$. The points in rectangles, downward triangles, upward triangles, and diamonds correspond to the entanglement entropy evolution at the non-Fibonacci numbers, with the expressions given in Eqs. (129), (133), (137), and (140), respectively.

(1) Let

$$n = F_{6m} + F_{6m-3} + F_{6m-6} + \cdots F_6 + F_3 \tag{126}$$

be an integer that increases with m. Correspondingly

$$\Pi_n = \Pi_{6m}\Pi_{6m-3}\ldots\Pi_6\Pi_3 = (\Pi_6\Pi_3)^m. \tag{127}$$

Recall from (122), the product $\Pi_6\Pi_3$ and Π_n can be evaluated explicitly

$$\Pi_6\Pi_3 = \begin{pmatrix} \cosh(4\theta) & -\sinh(4\theta) \\ -\sinh(4\theta) & \cosh(4\theta) \end{pmatrix},$$
$$\Pi_n = \begin{pmatrix} \cosh(4m\theta) & -\sinh(4m\theta) \\ -\sinh(4m\theta) & \cosh(4m\theta) \end{pmatrix}. \tag{128}$$

The corresponding entropy for the half-system $A = [0, L/2]$ and the total energy are

$$S_A(n) - S_A(0) = \frac{c}{3} 4m\theta, \quad E(n) = \frac{\pi c}{8L}\cosh(8m\theta) - \frac{\pi c}{6L}, \tag{129}$$

where we have constrained $\theta > 0$. The plot of Eq. (129) can be found in Figs. 22 and 23. Note that $S_A(n)$ and $E(n)$ grow linearly and exponentially, respectively, as a function of m for large m. However, m is not the actual driving step number. We need to convert to the actual step number $n \sim e^{6m\log\varphi}$, which grows exponential with m for large m, and $\varphi = \frac{\sqrt{5}+1}{2}$ is the

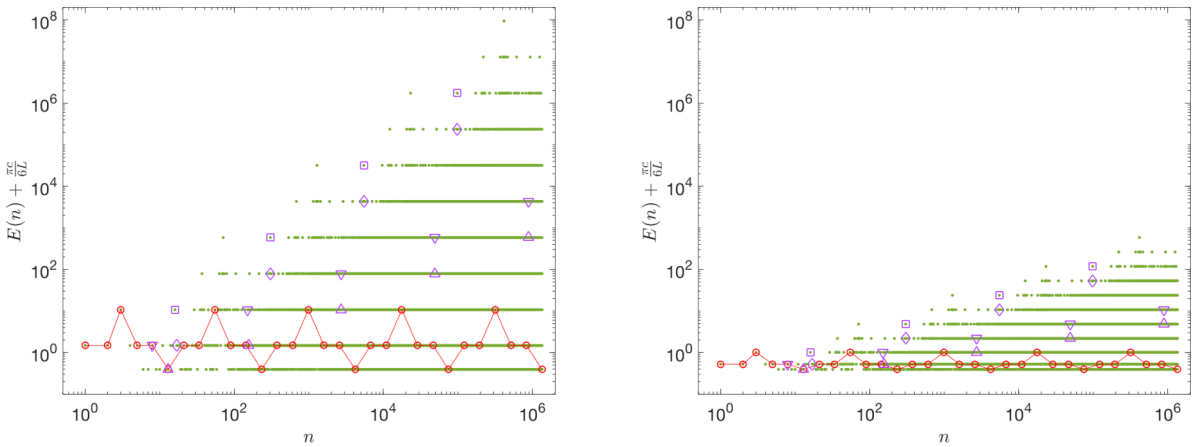

FIG. 23. Time evolution of the total energy at the nonheating fixed point in Eq. (96) for $\theta = 0.5$ (left) and $\theta = 0.2$ (right). The red solid lines are the total energy at the Fibonacci numbers $n = F_j$, with the expression given in Eq. (123), where we choose $c = 1$ and $L = 1$. The points in rectangles, downward triangles, upward triangles, and diamonds correspond to the entanglement entropy evolution at the non-Fibonacci numbers, with the expressions given in Eqs. (129), (133), (137), and (140), respectively.

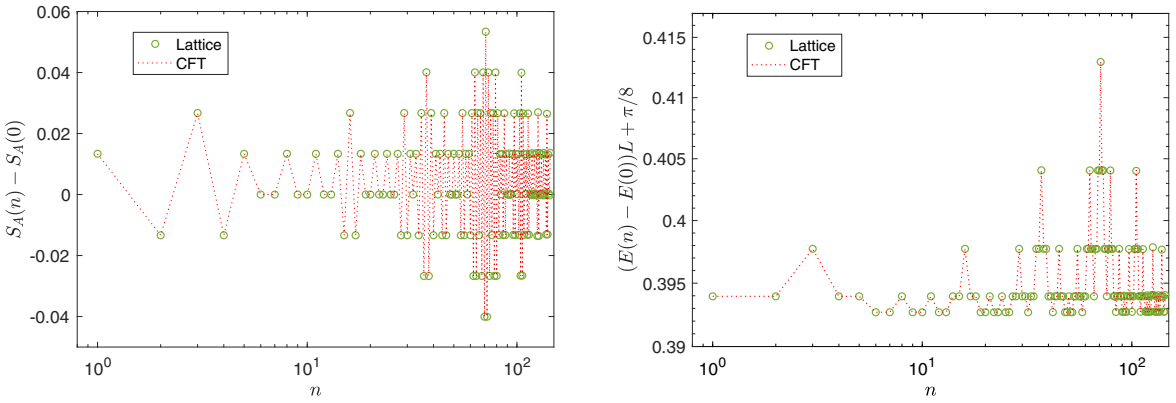

FIG. 24. Comparison of the lattice and CFT calculations at the nonheating fixed point for the entanglement entropy evolution (left) and the total energy evolution (right). Here we choose $c = 1$, $A = [0, L/2]$, $\theta = 0.02$, and $n_{\max} = F_{11} = 144$. In the lattice calculation we consider $L = 2000$. A plot of the entanglement entropy for a larger $n_{\max}$ can be found in Fig. 25.

golden ratio. Therefore,

$$S_A(n) - S_A(0) \simeq \frac{2\,c\theta}{9\,\log\phi}\log n, \quad E(n) \simeq \frac{\pi c}{16L} n^{\frac{4\theta}{3\log\phi}}. \tag{130}$$

That is to say, at the non-Fibonacci numbers n in Eq. (126), the entanglement entropy $S_A(n)$ grows logarithmically in time, and the total energy grows in a power law in time. This corresponds to the feature of phase transition (or critical phase) in the periodically driven CFT (see Table I).

(2) Now we choose a difference sequence to demonstrate that the growth rate at this fixed point depends on the sequence we pick when approaching the long-time limit. Let

$$n = F_{6m-1} + F_{6m-7} + \cdots + F_5 \tag{131}$$

and, correspondingly,

$$\Pi_n = \Pi_{6m-1}\Pi_{6m-7}\ldots\Pi_5 = (\Pi_{F_5})^m = \begin{pmatrix} \cosh(2m\theta) & -\sinh(2m\theta) \\ -\sinh(2m\theta) & \cosh(2m\theta) \end{pmatrix}. \tag{132}$$

The entropy and energy formulas are

$$S_A(n) - S_A(0) = \frac{c}{3}2m\theta \simeq \frac{c\theta}{9\,\log\phi}\log n, \tag{133}$$

$$E(n) = \frac{\pi c}{8L}\cosh(4m\theta) - \frac{\pi c}{6L} \simeq \frac{\pi c}{16L} n^{\frac{2\theta}{3\log\phi}}. \tag{134}$$

In the two examples above, the entanglement entropies all grow with n. One can observe in Fig. 22 that at certain points the entanglement entropy may decrease. We will investigate these points using the following examples:

(1) Let

$$n = F_{6m-1} + \cdots + F_{11} + F_5 + F_4. \tag{135}$$

Note the last element is important. The corresponding matrix is given as

$$\Pi_n = (\Pi_{F+5})^m\Pi_4 = i\begin{pmatrix} \cosh[(m-1)2\theta] & \sinh[(m-1)2\theta] \\ -\sinh[(m-1)2\theta] & -\cosh[(m-1)2\theta] \end{pmatrix}. \tag{136}$$

The corresponding entropy and energy formulas are

$$S_A(n) - S_A(0) = -\frac{c}{3}2(m-1)\theta, \quad E(n) = \frac{\pi c}{8L}\cosh[4(m-1)\theta] - \frac{\pi c}{6L}, \tag{137}$$

where $\theta > 0$. The results are similar to Eq. (133), with a minus sign difference in the entropy formula. In other words, we have a logarithmic decrease in the entanglement evolution and a power-law growth in the total energy evolution (see Figs. 22 and 23).

The entanglement decrease might look bizarre, but this could happen in a system with infinite entropy to start with, e.g., in the continuous field theories where a UV regulator is required in the entropy calculation, which itself is a manifestation of the large entanglement in the vacuum state.

Technically, we may explain the origin of the decreasing entropy as follows: the form of the conformal transformation in (136) indicates that the energy-momentum density [see (32)] locates exactly at $x = L/2$, which coincides with the entanglement cut we choose. As discussed in detail in Appendix A 3 b, in this case, the entanglement entropy will decrease in time. Physically, it is because the degrees of freedom that carry the entanglement between two regions are accumulated at the entanglement cut. We emphasize that the points with decreasing entanglement entropy are due to the coincidence of the energy-density peak and the entanglement cut, and therefore are not generic. In general, at the nonheating fixed points, the envelopes of the entanglement entropy and total energy will grow logarithmically and in a power law in time, respectively.

(2) Another example with decreasing entropy we present in Figs. 22 and 23 is that

$$n = F_{6m} + F_{6m-3}\ldots F_6 + F_3 + F_1 \tag{138}$$

with

$$\Pi_n = (\Pi_6\Pi_3)^m\Pi_1 \tag{139}$$

and the corresponding entropy and energy

$$S_A(n) - S_A(0) = -\frac{c}{3}(4m-2)\theta, \quad E(n) = \frac{\pi c}{8L}\cosh[(8m-4)\theta] - \frac{\pi c}{6L}. \tag{140}$$

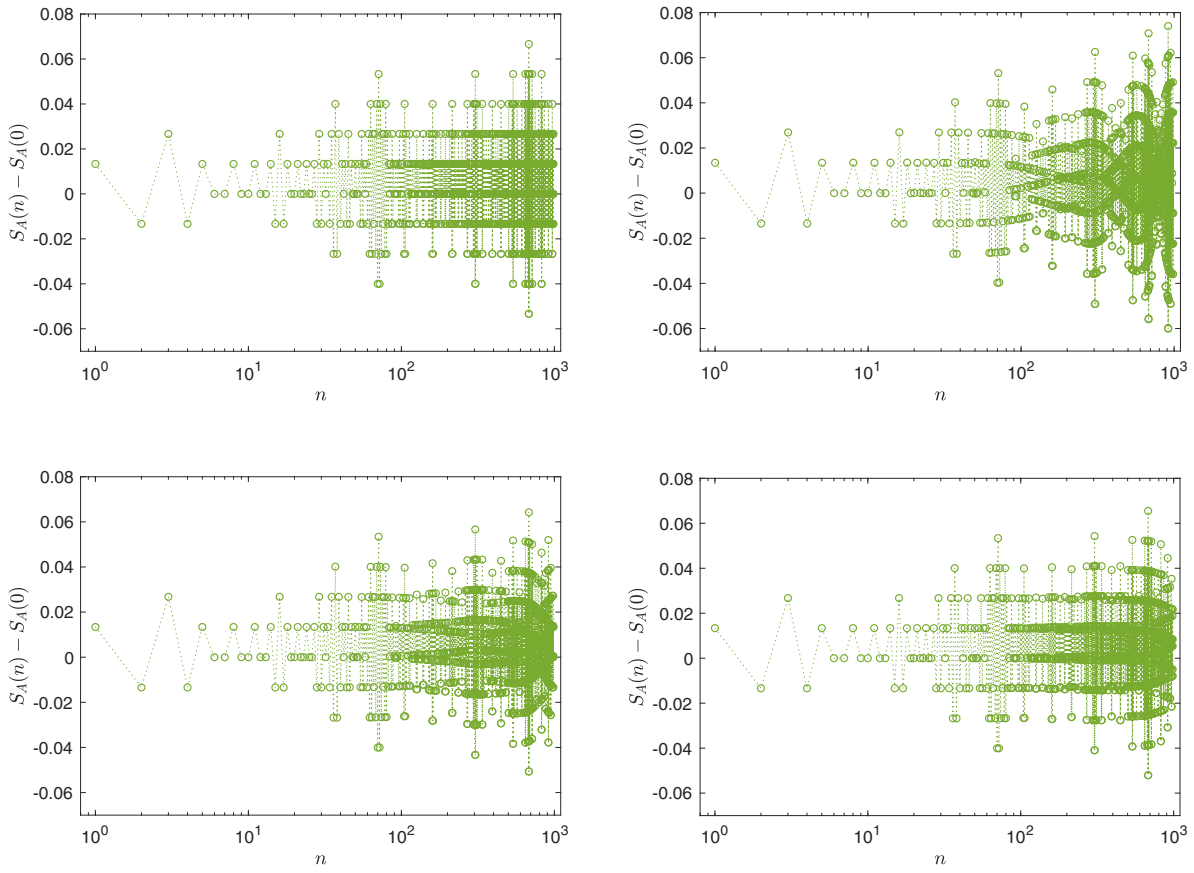

FIG. 25. Comparison of the CFT (top left) and lattice calculations on the entanglement entropy evolution $S_A(n)$ at the nonheating fixed point. Here we choose $c = 1$, $A = [0, L/2]$, $\theta = 0.02$, and $n_{\max} = F_{15} = 987$. In the lattice calculation, we consider $L = 500$ (top right), 1000 (bottom left), and 2000 (bottom right), respectively.

Using the same procedure above, one can find many other series of discrete points with different growing (and decreasing) rates in the entanglement and energy evolution in Figs. 22 and 23, these series together form the fan structure in the figures.

3. *Comparison of CFT and lattice calculations*

In this section, we compare the CFT and lattice calculations for the time evolution of entanglement entropy and energy at the nonheating fixed point as discussed in the previous subsections. The lattice model we use is the same as that studied in Sec. IV D 2. The two lattice Hamiltonians under consideration are

$$H_0 = \frac{1}{2}\sum_{j=1}^{L-1} c_j^\dagger c_{j+1} + \text{H.c.}, \quad H_\theta = \frac{1}{2}\sum_{j=1}^{L-1} f(j) c_j^\dagger c_{j+1} + \text{H.c.}, \tag{141}$$

where L is the total length of the lattice and $f(j) = 1 - \tanh(2\theta)\cos\frac{2\pi j}{L}$, with the initial state chosen as the ground state of H_0. The corresponding driving time intervals are $T_0 = L/2$ and $T_1(\theta) = L_{\text{eff}}/2$, where $L_{\text{eff}} = L\cosh(2\theta)$. Then, we drive the system with the Fibonacci sequence as introduced in Sec. V A 1.

Figure 24 presents the comparison of the lattice and CFT results on the entanglement and energy evolution. We find that the agreement is remarkable. A comparison on the entanglement entropy evolution with larger driving steps n can be found in Fig. 25. In general, the agreement will break down for a large enough n since more higher-energy modes will be involved as n increases (recall that the envelope of the total energy growth is power law in time at the nonheating fixed point). On the lattice model, the high-energy modes are no longer well described by a CFT, and therefore there must be a breakdown at certain n.[21]

[21]More precisely, let us denote n^* as the driving step at which the agreement between CFT and lattice calculations breaks down. From Fig. 24, one can observe that n^* is a monotonically increasing function of L. This dependence can be understood as follows: One may consider the wave function in the "Fock space" (which is Verma module here) of a CFT of finite length L. The initial state is the ground state $|0\rangle$. As we drive the system, higher-energy modes $|N\rangle$ ($N > 1$) will be involved. It is noted that N is independent of the length L of the CFT. Since the energy spacing is proportional to $1/L$, one can find the energy $E_N(L)$ corresponding to $|N\rangle$ is higher than $E_N(L')$ if $L < L'$. For a small L, $E_N(L)$ may be in the high-energy region which is no longer described by a CFT. However, by increasing L to a large enough L', we can push $E_N(L')$ into the low-energy region which is well described by a CFT. This is why we have a better agreement in Fig. 24 for a larger L.

4. Exact nonheating fixed points in more general cases

With the concrete examples illustrated in the previous discussions, now we are ready to prove the statements as mentioned in the beginning of Sec. V B, which we rewrite here:

(1) If both the driving Hamiltonians are chosen as elliptic types, one can always find *exact* fixed points in the nonheating phases.

(2) At these (nonheating) fixed points, both the entanglement entropy and the energy evolution are of period 6, i.e., $S_A(F_k) = S_A(F_{k+6})$ and $E(F_n) = E(F_{n+6})$.

(3) The envelopes of the entanglement entropy and total energy will grow logarithmically and in a power law as a function of the driving steps n, respectively.

$$M = \begin{pmatrix} -\cos\left(\frac{\mathcal{C}\pi T}{l}\right) - i\frac{\sigma^0}{\mathcal{C}}\sin\left(\frac{\mathcal{C}\pi T}{l}\right) & -i\frac{\sigma^+ + i\sigma^-}{\mathcal{C}}\sin\left(\frac{\mathcal{C}\pi T}{l}\right) \\ i\frac{\sigma^+ - i\sigma^-}{\mathcal{C}}\sin\left(\frac{\mathcal{C}\pi T}{l}\right) & -\cos\left(\frac{\mathcal{C}\pi T}{l}\right) + i\frac{\sigma^0}{\mathcal{C}}\sin\left(\frac{\mathcal{C}\pi T}{l}\right) \end{pmatrix}, \tag{143}$$

where $\mathcal{C} = \sqrt{(\sigma^0)^2 - (\sigma^+)^2 - (\sigma^-)^2}$ and $(\sigma^0)^2 - (\sigma^+)^2 - (\sigma^-)^2 > 0$ with σ^0, σ^+, $\sigma^- \in \mathbb{R}$. $l = L/q$ is the wavelength of deformation [see, e.g., Eq. (13)]. One can obtain the reflection matrix by choosing $T = \frac{1}{2}L_{\text{eff}}$ in Eq. (143), where $L_{\text{eff}} := l/\mathcal{C}$ is the effective length. Then Eq. (143) becomes

$$M = \begin{pmatrix} -i\frac{\sigma^0}{\mathcal{C}} & -i\frac{\sigma^+ + i\sigma^-}{\mathcal{C}} \\ i\frac{\sigma^+ - i\sigma^-}{\mathcal{C}} & i\frac{\sigma^0}{\mathcal{C}} \end{pmatrix}, \tag{144}$$

which is traceless obviously. That is to say, to arrive at the nonheating fixed point, we need to set $T_{A(B)} = l/2\mathcal{C}_{A(B)}$ and the corresponding reflection matrices M_A and M_B take the form of (144) with subscripts A and B. ■

Proof of claim 2. Having two reflection matrices M_A and M_B, we immediately have the following useful property:

$$M_A^2 = M_B^2 = -1\,. \tag{145}$$

Now let us use this to prove the claim 2.

To verify the periodicity of entanglement entropy $S_A(F_n)$ and energy $E(F_n)$, it is sufficient to show the periodicity of the conformal transformation matrix Π_{F_n}. Let us first examine the case for $n = 0 \ldots 6$. Following the definition, the first 3 are

$$\Pi_{F_0} = M_B, \quad \Pi_{F_1} = M_A, \quad \Pi_{F_2} = M_A M_B. \tag{146}$$

Note the $\Pi_{F_0} \neq \Pi_{F_1}$ is introduced as a convenient notation which satisfies the recurrence relation. For $n = 3, 4$, we can use the recurrence relation and find

$$\begin{aligned} \Pi_{F_3} &= \Pi_{F_2}\Pi_{F_1} = M_A M_B M_A, \\ \Pi_{F_4} &= \Pi_{F_3}\Pi_{F_2} = M_A M_B M_A M_A M_B = M_A, \end{aligned} \tag{147}$$

where in the last equation we have used the property that $M_A^2 = M_B^2 = -1$. The results for $n = 5, 6$ are also obtained analogously

$$\begin{aligned} \Pi_{F_5} &= \Pi_{F_4}\Pi_{F_3} = M_A M_A M_B M_A = -M_B M_A, \\ \Pi_{F_6} &= \Pi_{F_5}\Pi_{F_4} = -M_B M_A M_A = M_B. \end{aligned} \tag{148}$$

Note we have already verified the periodicity for $\Pi_{F_0} = \Pi_{F_6}$, further more $\Pi_{F_7} = \Pi_{F_6}\Pi_{F_5} = -M_B M_B M_A = M_A = \Pi_{F_1}$. And the recurrence relation for Π_{F_n} only depends on the previous two elements, therefore, we conclude

$$\boxed{\Pi_{F_{n+6}} = \Pi_{F_n}, \quad n \in \mathbb{Z}^{\geqslant 0}\,.} \tag{149}$$

The claim 2 follows immediately. ■

Proof of claim 1. The nonheating fixed point has initial condition $(x_{F_2}, x_{F_1}, x_{F_0}) = (a, 0, 0)$, in terms of traces, we have

$$\text{Tr}(M_A M_B) = 2a\,, \quad \text{Tr}(M_A) = \text{Tr}(M_B) = 0. \tag{142}$$

In other words, to prove claim 1, we only need to find suitable initial conditions T_A and T_B for two elliptic Hamiltonians H_A and H_B such that the SU(1, 1) matrices M_A and M_B are traceless, i.e., are reflection matrices [see (79)]. Note the condition $\text{Tr}(M_A M_B) = 2a$ does not have a content as a can be arbitrary.

Now, we explicitly find such T_A and T_B. As discussed in Appendix A 1, for a general elliptic Hamiltonian H (see Sec. II A) with driving interval T, the corresponding Möbius transformation is represented as follows:

Proof of claim 3. First, Refs. [76,77] generally prove that the norm of Π_n is polynomially bounded at $\lambda_L = 0$. Therefore, we only need to show there is at least a sequence of point that approaches infinity polynomially similar to what we showed in last section for a specific example.

Note, for any two distinct reflection matrix M_A and M_B, their product is hyperbolic. Then, we can use their product to generate a sequence of points, e.g., $\Pi_{F_6} = M_B$ and $\Pi_{F_7} = M_A$ we can generate

$$\Pi_n = \Pi_{F_{6m+1}}\Pi_{F_{6m}}\Pi_{F_{6m-5}}\Pi_{F_{6m-6}}\ldots\Pi_{F_7}\Pi_{F_6} = (M_A M_B)^m \tag{150}$$

for

$$n = F_{6m+1} + F_{6m} + F_{6m-5} + F_{6m-6} + \cdots + F_7 + F_6\,. \tag{151}$$

Since $|\text{Tr}(M_A M_B)| > 2$, we conclude that $|\text{Tr}\,\Pi_n| \sim e^{m\lambda}$ at $m \to \infty$ where

$$\lambda = \log\frac{|\text{Tr}(M_A M_B)| + \sqrt{|\text{Tr}(M_A M_B)| - 4}}{2} > 0. \tag{152}$$

Therefore, the total energy will grow exponentially with respect to m as if in the heating phase. However, remember the step index n is also exponential in m and therefore in terms of physical steps n, the energy grows in power law. Similarly, we have the entanglement entropy grow logarithmically.[22] ■

C. Entanglement and energy dynamics in the heating phases

In this section, we present the rich features in the heating phase, including the time evolution of total energy, energy-momentum density, and entanglement entropy.

[22]For the subtlety about the sign in entropy growth, one can always multiply one more matrix or move the entanglement cut to ensure the entropy is growing instead of decreasing.

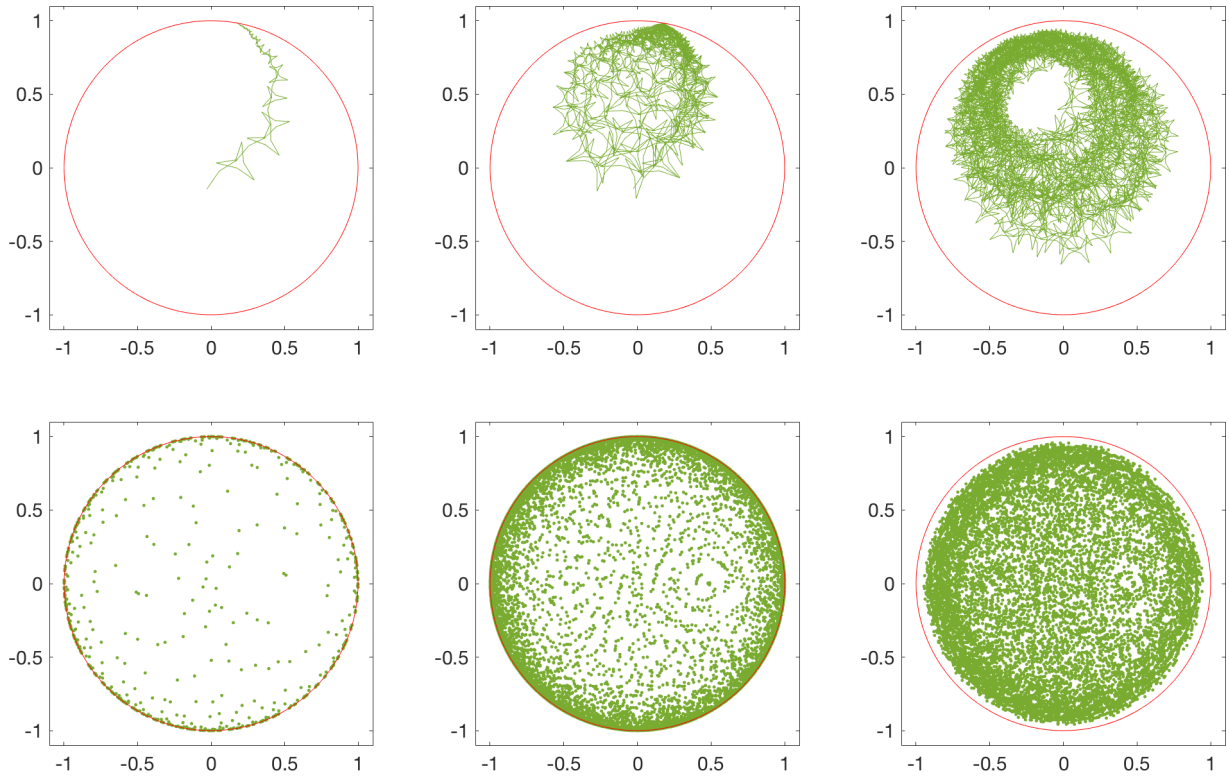

FIG. 26. Group walking of ρ (top) and $(\rho\,\zeta)$ (bottom) in the heating phase of a Fibonacci driven CFT. We consider a Fibonacci quasiperiodical driving with H_0 and $H_{\theta=0.5}$. The parameters are $T_0/L = \frac{1}{2}$, and (from left to right) $T_1/L_{\text{eff}} = 0.041$, 0.04, and 0.0401, respectively. The total number of driving steps is taken as $F_{20} = 10\,946$.

1. Group walking and entanglement and energy evolution

As discussed in Sec. III B, the group walking of ρ and $(\rho\,\zeta)$ of the SU(1, 1) matrix in (43) reflects the time-evolution properties of the total energy, energy-momentum density, and the entanglement entropy. In the following, we will study the group walking of ρ and $\rho\zeta$, as well as the energy and entanglement evolution. The detailed discussion on energy-momentum density is left to the next subsection.

First, we consider the group walking of ρ in Π_n:

$$\Pi_n = \frac{1}{\sqrt{1-|\rho|^2}}\begin{pmatrix} \sqrt{\zeta} & -\rho^*\frac{1}{\sqrt{\zeta}} \\ -\rho\sqrt{\zeta} & \frac{1}{\sqrt{\zeta}} \end{pmatrix}, \quad \rho \in \mathbb{D},\ \zeta \in \partial\mathbb{D}. \tag{153}$$

Shown in Fig. 26 is a sample plot of the group walking of ρ and $\rho\zeta$ nearby a certain point [which is $T_0/L = \frac{1}{2}$ and $T_1/L_{\text{eff}} = 0.04$ here, with $L_{\text{eff}} = L\cosh(2\theta)$] in the parameter space. See also Fig. 27 for another sample plot. The two driving Hamiltonians are H_0 and $H_{\theta=0.5}$, with H_θ given in Eq. (71). As the driving steps n increase, one can find that ρ will walk to a certain point $\rho_{n=\infty}$ on $\partial\mathbb{D}$. This is quite an interesting feature since ρ does not move around on $\partial\mathbb{D}$ in the limit $n \to \infty$.[23]

As we have discussed in Sec. III B, as ρ approaches the boundary $\partial\mathbb{D}$, both the entanglement entropy and the total energy of the system will grow accordingly, as seen from Eqs. (45) and (49). In Figs. 26 and 27, one can find that for different $(T_0,\ T_1)$, ρ approaches the boundary $\partial\mathbb{D}$ with different rates, which correspond to different Lyapunov exponents and different growth rates in the entanglement entropy and total energy. This can be intuitively seen by looking at the entanglement and energy growth in Figs. 28 and 29, respectively. Also, the patterns in $|\rho_n|$ in Figs. 26 and 27 result in the oscillating features in the entanglement and energy growth in Figs. 28 and 29.[24]

As a remark, it is noted that for the case of $T_1/L_{\text{eff}} = 0.0401$ in Figs. 26 and 28, ρ does not walk to the boundary $\partial\mathbb{D}$, and the total energy seems to simply oscillate in n. This is because the Lyapunov exponent at this point is too small. One needs to take a longer time (larger n) to observe the growth behavior.

Second, let us consider the group walking of $(\rho\zeta)$. As shown in Figs. 26 and 27, different from the behavior of ρ, which walks to a fixed ρ_∞ in the $n \to \infty$ limit, $(\rho\zeta)$ will walk around on the boundary $\partial\mathbb{D}$ even in the $n \to \infty$ limit. This will result in two interesting features:

[23] It is interesting that this phenomenon also happens in the heating phases of both the periodic and random driving CFTs, where we can prove that ρ_n converge to a fixed $\rho_{n=\infty}$ on $\partial\mathbb{D}$ [see, e.g., Eq. (63) for the case of periodical drivings]. We suspect this is generic feature as long as the Lyapunov exponent is positive, and it is interesting to prove this observation, e.g., in the Fibonacci driven CFT here.

[24] It is noted that the total energy only depends on $|\rho|$, as seen from Eq. (45). Therefore, the oscillating structures in $E(n)$ are totally due to $|\rho|$. For the entanglement entropy $S_A(n)$, however, it depends on both $|\rho|$ and $\rho\zeta$, as seen from Eq. (49). Then, the oscillating structures in $S_A(n)$ come from both $|\rho|$ and $\rho\zeta$.

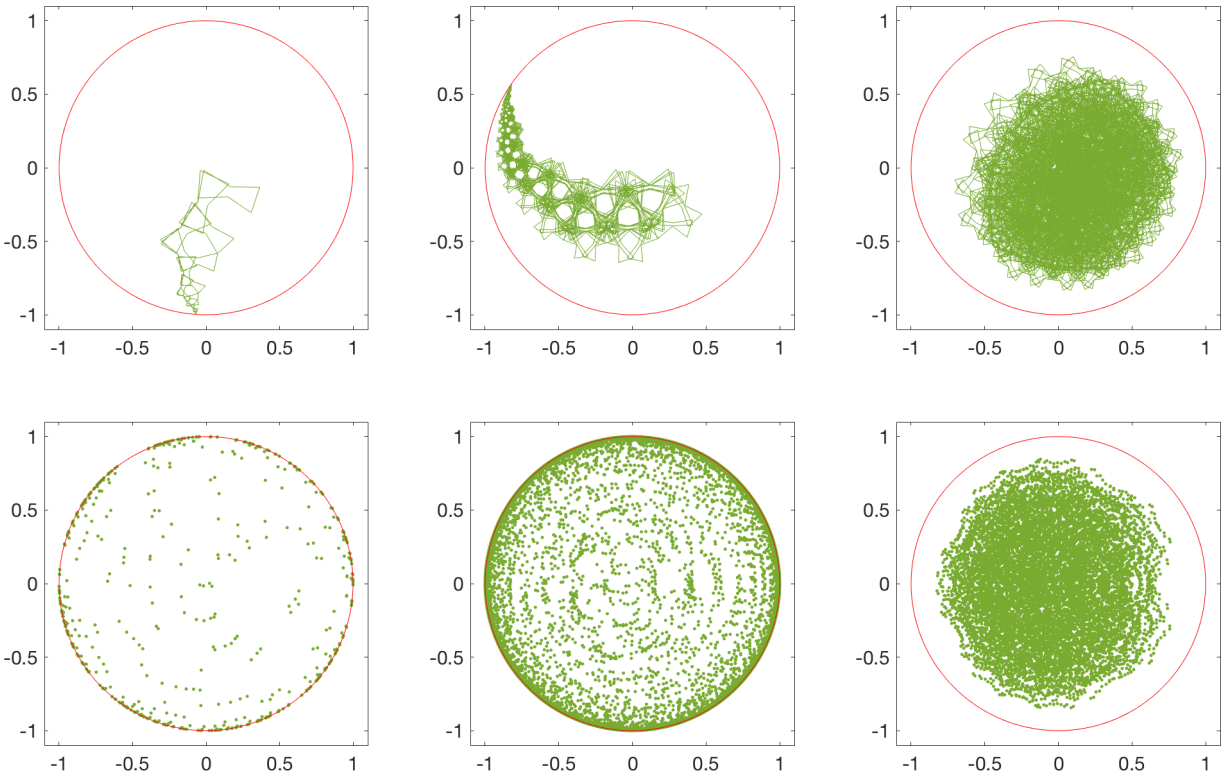

FIG. 27. Group walking of ρ (top) and $(\rho\,\zeta)$ (bottom) in the heating phase of a Fibonacci driven CFT. We consider a Fibonacci quasiperiodical driving with H_0 and $H_{\theta=0.5}$. The parameters are $T_0/L = 0.6$, and (from left to right) $T_1/L_{\text{eff}} = 0.06, 0.05$, and 0.055, respectively. The total number of driving steps is taken as $F_{20} = 10\,946$.

(1) The locations of energy-momentum density peaks will move around during the quasiperiodic driving, as seen from Eq. (48).

(2) More oscillating structures will be introduced in the time evolution of the entanglement entropy. As discussed in Sec. III B, the total energy only depends on $|\rho|$, but the entanglement entropy depends on both $|\rho|$ and $\rho\zeta$, as seen in Eq. (49). This extra oscillating structure can be found in Figs. 28 and 29, in particular for the case with large Lypunov exponents.

In a short summary, there are rich patterns in the group walking of ρ and $(\rho\zeta)$ in the heating phase of a Fibonacci quasiperiodically driven CFT. The velocity of ρ walking towards $\partial\mathbb{D}$ determines the value of Lyapunov exponents, and

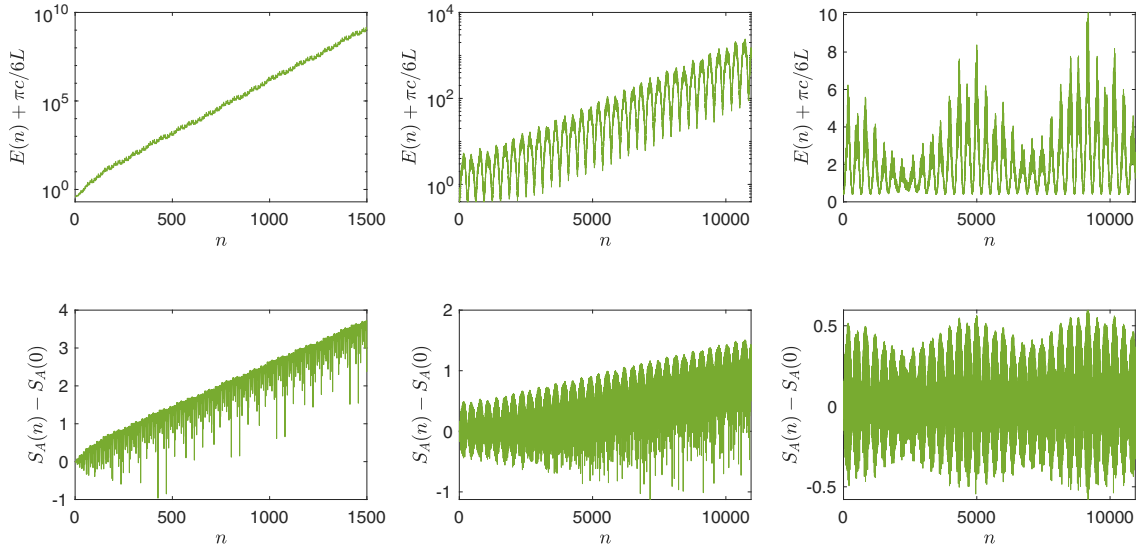

FIG. 28. Time evolution of the total energy (top) and the entanglement entropy (bottom) of $A = [0, L/2]$. The parameters are the same as those in Fig. 26. Note that the total energy and entanglement entropy (in the left plot) are plotted in a small window to see the detailed oscillating structure.

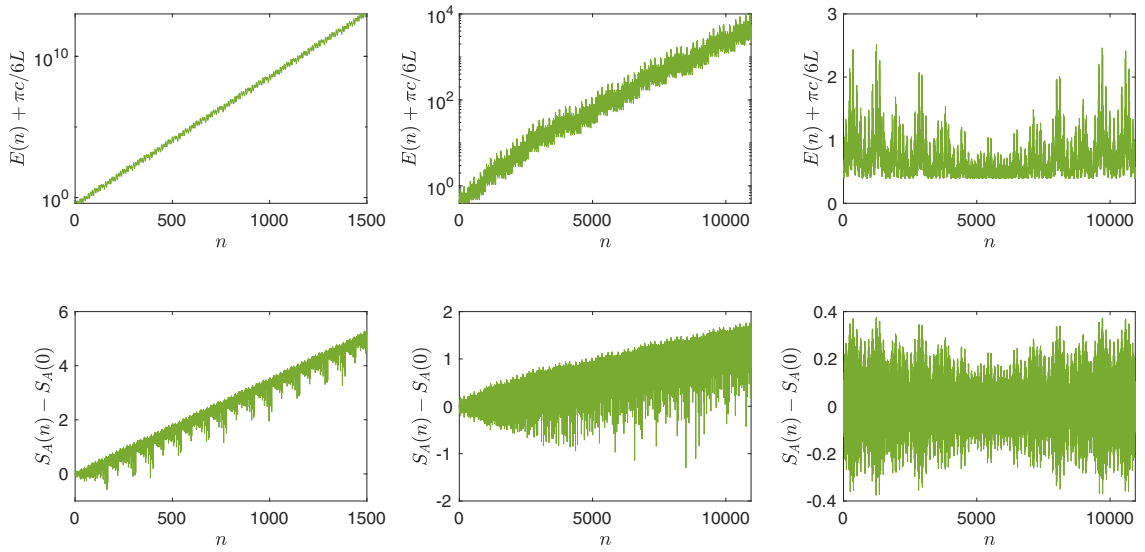

FIG. 29. Time evolution of the total energy (top) and the entanglement entropy (bottom) of $A = [0, L/2]$ of the system. The parameters are the same as those in Fig. 27. Note that the total energy and entanglement entropy (in the left plot) are plotted in a small window to see the detailed oscillating structure.

therefore the growth rate of the entanglement entropy and total energy. The behavior of $|\rho|$ determines the concrete features of the energy growth $E(n)$ through Eq. (45). In general, one can observe various oscillating features in the growth of $E(n)$. Both $|\rho|$ and $(\rho\zeta)$ determine the features of $S_A(n)$ through Eq. (49), where more patterns of oscillations can be observed comparing to $E(n)$.

2. *Locations of energy-momentum density peaks*

There are several features on the distribution of energy-momentum density we hope to point out in the heating phase of a Fibonacci driven CFT:

(1) In the heating phase, there are an array of peaks of energy-momentum density distributed in the real space. The locations of these peaks are determined by Π_n through Eq. (48). In fact, as we have shown in Sec. III A, a positive Lyapunov exponent λ_L always indicates an array of peaks in the energy-momentum density $\langle T(x, n)\rangle$ in real space.

(2) Different from the periodically driven CFT, where the peaks are located at the same positions after each period of driving [see Eq. (66)], in the quasiperiodical driving, since there is not a regular driving period, the locations of the energy-momentum density peaks will in general move around after each driving step. This can be seen based on the group walking of $(\rho\zeta)$, which determines the locations of energy-momentum density peaks [see Eq. (48)], in Figs. 26, 27, and 30.

(3) Although the locations of the energy-momentum density peaks will move around, in the long-time driving limit ($n \gg 1$), we can still find some regular patterns. In particular, we find there is an even or odd effect in the distribution of these energy-momentum density peaks when the driving steps are Fibonacci numbers. More concretely, let us denote x_{peak} as the locations of peaks of the energy-momentum density. Then we observe that

$$x_{\text{peak}}(F_n) = x_{\text{peak}}(F_{n+2}), \tag{154}$$

as shown in Fig. 30.

We find that the even-odd effect as mentioned above is closely related to the group walking of ρ as discussed in the previous subsection, i.e., in the long-time driving limit $n \to \infty$, ρ will flow to a certain point ρ_∞ on $\partial\mathbb{D}$. By taking this as an assumption, i.e., $\lim_{n\to\infty} \rho_n = \rho_\infty \in \partial\mathbb{D}$, one can prove that there are indeed even or odd effects in the locations of energy-momentum density peaks, as follows.

Let us denote the matrix elements of $\Pi_{F_{n-1}}$ and Π_{F_n} as follows:

$$\begin{aligned}
\Pi_{F_{n-1}} &= \frac{1}{\sqrt{1-|\rho|^2}}\begin{pmatrix} \sqrt{\zeta} & -\rho^* \frac{1}{\sqrt{\zeta}} \\ -\rho\sqrt{\zeta} & \frac{1}{\sqrt{\zeta}} \end{pmatrix}, \\
\Pi_{F_n} &= \frac{1}{\sqrt{1-|\rho'|^2}}\begin{pmatrix} \sqrt{\zeta'} & -\rho'^* \frac{1}{\sqrt{\zeta'}} \\ -\rho'\sqrt{\zeta'} & \frac{1}{\sqrt{\zeta'}} \end{pmatrix}.
\end{aligned} \tag{155}$$

Then, applying the recurrence relation, we have

$$\begin{aligned}
\Pi_{F_{n+1}} &= \Pi_{F_n}\Pi_{F_{n-1}} \\
&= \frac{1}{\sqrt{(1-|\rho|^2)(1-|\rho'|^2)}} \\
&\quad \times \begin{pmatrix} \sqrt{\zeta}\sqrt{\zeta'} + \rho(\rho')^* \frac{\sqrt{\zeta}}{\sqrt{\zeta'}} & -(\rho')^* \frac{1}{\sqrt{\zeta}\cdot\sqrt{\zeta'}} - \rho^* \frac{\sqrt{\zeta'}}{\sqrt{\zeta}} \\ -\rho'\sqrt{\zeta}\sqrt{\zeta'} - \rho \frac{\sqrt{\zeta}}{\sqrt{\zeta'}} & \frac{1}{\sqrt{\zeta}\cdot\sqrt{\zeta'}} + \rho^*\rho' \frac{\sqrt{\zeta'}}{\sqrt{\zeta}} \end{pmatrix} \\
&:= \frac{1}{\sqrt{1-|\rho''|^2}}\begin{pmatrix} \sqrt{\zeta''} & -\rho''^* \frac{1}{\sqrt{\zeta''}} \\ -\rho''\sqrt{\zeta''} & \frac{1}{\sqrt{\zeta''}} \end{pmatrix}.
\end{aligned} \tag{156}$$

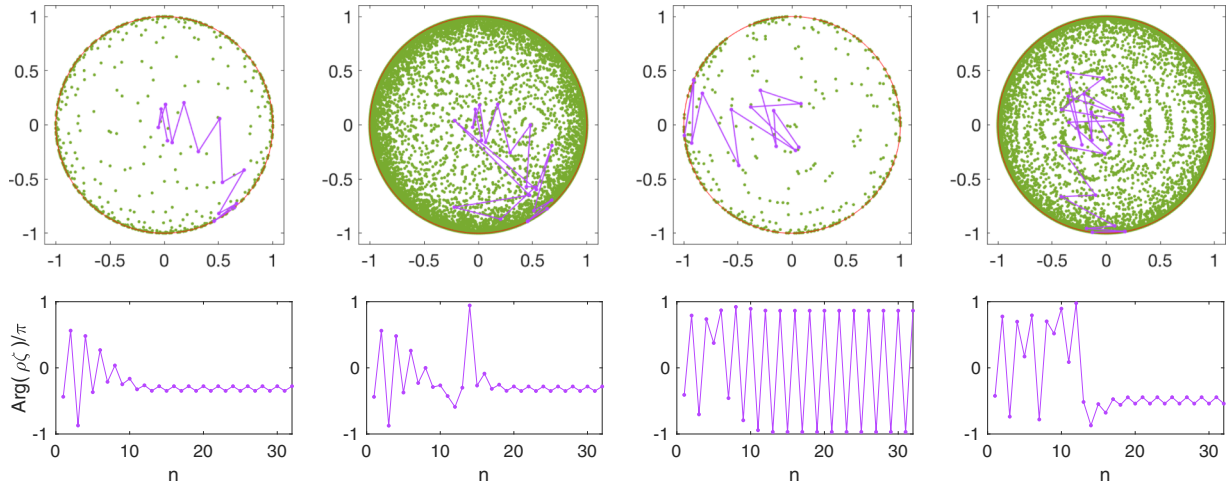

FIG. 30. (Top) Group walking of $(\rho\zeta)$ at all numbers (green dots) and at Fibonacci numbers (purple). The two driving Hamiltonians are H_0 and $H_{\theta=0.5}$. The parameters (from left to right) are $T_0/L = \frac{1}{2}$ and $T_1/L_{\text{eff}} = 0.041$, $T_0/L = \frac{1}{2}$ and $T_1/L_{\text{eff}} = 0.04$, $T_0/L = 0.6$ and $T_1/L_{\text{eff}} = 0.06$, $T_0/L = 0.6$ and $T_1/L_{\text{eff}} = 0.05$, respectively. The first (last) two plots have the same parameters as those in Fig. 26 (Fig. 27). The total number of driving steps are $F_{25} = 121\,393$. This means there are in total 25 steps of moving (purple lines) at the Fibonacci numbers. (Bottom) $\text{Arg}(\rho\zeta) \in (-\pi, \pi]$ as a function of n, where n denotes the nth Fibonacci numbers F_n. The parameters are the same as the top panel, but with a larger driving number F_{32}.

In the heating phase, assuming $\rho \approx \rho' \to \rho_\infty$ at $n \to \infty$ with $|\rho_\infty| = 1$, we have

$$\rho''\zeta'' = \frac{\rho'\zeta\zeta' + \rho\zeta}{1 + \rho^*\rho'\zeta'} = \frac{\rho\zeta(1+\zeta')}{1+\zeta'} = \rho\zeta,$$
$$\rho'' = \rho' = \rho = \rho_\infty. \tag{157}$$

The first formula in Eq. (157) indicates that

$$(\rho\zeta)_{F_n} = (\rho\zeta)_{F_{n+2}}, \quad n \in \mathbb{Z}^{>0}. \tag{158}$$

According to Eq. (48), this implies that in the long-time driving limit there is an even-odd effect in the locations of peaks of the energy-momentum density at the Fibonacci numbers [see Eq. (154)].

D. Other quasiperiodic driving: Aubry-André type

The other well-known model for the quasicrystal is the Aubry-André model [78,79], which describes free-electron hopping on a one-dimensional lattice with the following Hamiltonian:

$$H = \sum_j (c_j^\dagger c_{j+1} + c_{j+1}^\dagger c_j) + \lambda \sum_j \cos(2\pi\omega j + \delta) c_j^\dagger c_j,$$

where ω is an irrational number that is incommensurate to the lattice periodicity and thus characterizes a quasiperiodic onsite potential. It has been used for the study of localization [80] and also appears in the two-dimensional integer quantum Hall effect [61]. Given an irrational ω, this model has a localization transition at $\lambda = 2$ and the two phases are related by a duality transformation. This is rigorously proved in the mathematics literature [67,80,81] by studying the so-called almost Mathieu operator, which is equivalent to the Aubry-André model at the single-particle level.

Motivated by the Aubry-André model, here we introduce another type of quasiperiodic driving, which we call an Aubry-André (quasiperiodically) driven CFT.

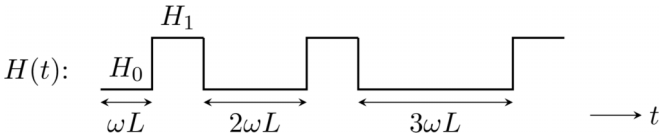

FIG. 31. Aubry-André quasiperiodic driving. In the nth cycle, H_0 is applied for time $T_0 = n\omega L$ and H_1 is applied for time T_1.

1. Setup

Let us first recall our minimal setup of the periodically driven CFT in Sec. IV D. Our protocol for the quasiperiodic driving will be a modification to that. In the minimal setup, the system takes the open boundary condition with $q = 1$. As depicted in Eq. (70), each cycle consists of two steps (H_0, T_0) and (H_1, T_1), with H_0 being $H_{\theta=0}$ and H_1 being $H_{\theta\neq 0}$. The SU(1, 1) matrices associated to the unitary evolution $e^{-iH_0T_0}$ and $e^{-iH_1T_1}$ are denoted as M_0 and M_1, respectively. The formula for M_1 is copied below for reader's convenience. Plugging in $\theta = 0$ yields M_0:

$$M_1 = \begin{pmatrix} \alpha & \beta \\ \beta^* & \alpha^* \end{pmatrix}, \begin{cases} \alpha = \cos\left(\frac{\pi T_\theta}{L_{\text{eff}}}\right) + i\,\cosh(2\theta)\sin\left(\frac{\pi T_\theta}{L_{\text{eff}}}\right), \\ \beta = -i\,\sinh(2\theta)\sin\left(\frac{\pi T_\theta}{L_{\text{eff}}}\right). \end{cases}$$

Note that T_0 and T_1 appear in M_0 and M_1 through cos and sin, which implies that $T_0 \to T_0 + L$ and $T_1 \to T_1 + L_{\text{eff}}$ yield the same set of SU(1, 1) matrices.[25]

This observation leads to the following way of introducing the quasiperiodicity. We keep T_1 fixed and let T_0 have a dependence on the number of cycles. In the nth cycle, H_0 is applied for time $T_0 = n\omega L$, where L is the system size. The whole sequence is depicted in Fig. 31. If $\omega = p/q$ is a

[25]Up to an overall minus sign that does not affect the dynamics because the actual Möbius transformation acts as $\text{SU}(1,1)/\mathbb{Z}_2$.

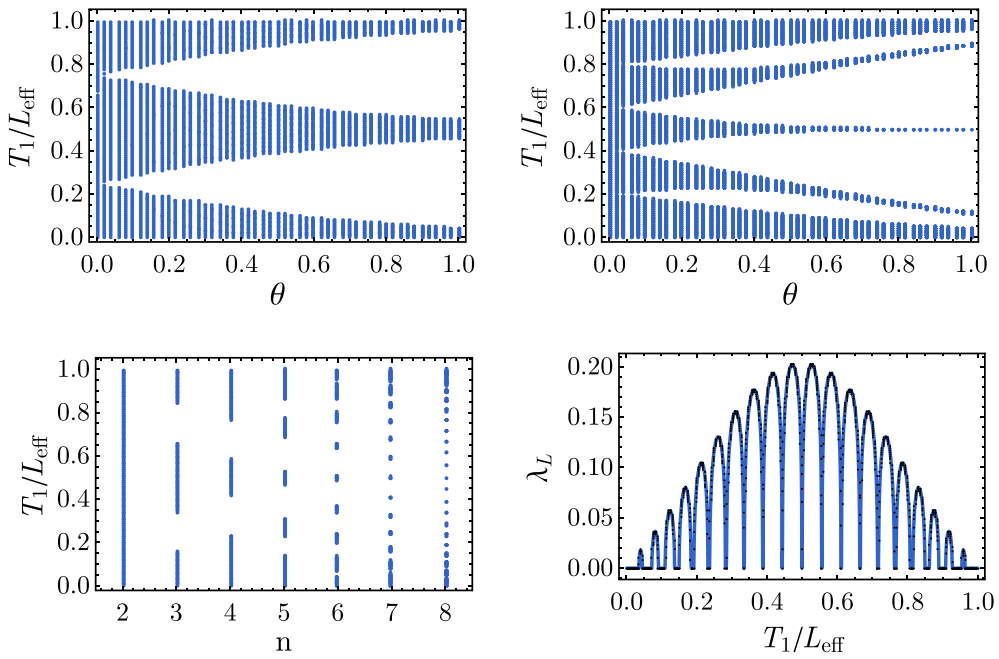

FIG. 32. Phase structure and Lyapunov exponents for the sequence of periodically driven CFT determined by $\omega_n = F_{n-1}/F_n$, with $n = 3$ (top left) and $n = 5$ (top right). In the top left and top right, the blue (white) regions are the region where the system is nonheating (heating). In the bottom left where $\theta = \frac{1}{5}$, for a given n, the blue lines (blank region) correspond to the nonheating (heating) phase. In the bottom right (where $\theta = \frac{1}{5}$ and $n = 8$) is the distribution of Lyapunov exponents.

rational number, the unitary evolution generated by $e^{-iH_0T_0}$ will repeat after every q cycles, and protocol is reduced to a periodic driving with each period consisting of q cycles. If ω is irrational, such periodicity disappears which gives rise to a quasiperiodic driving. One can also fix T_0 and vary T_1 instead, which does not change the result qualitatively and thus will not be discussed.

2. *Phase structure for a single irrational number*

It is subtle to directly access the dynamics with an irrational ω, especially when there is no analytical tool. For example, to extract the Lyapunov exponent by numerically computing the matrix product can be unstable due to numerical errors. Therefore, we will track a sequence of rational numbers to approach the physics at the irrational numbers. Each rational number corresponds to a periodic driving system and we can apply the trace classifier to identify the phase structure. This is exactly the same as our discussion for the Fibonacci driven CFT in Sec.V A 3.

To illustrate the general features, let us consider $\omega = (\sqrt{5}-1)/2$ being the inverse golden ratio as a concrete example, which can be approximated by the sequence $\omega_n = F_{n-1}/F_n, n = 1, 2, 3\ldots$. For a given n, the driving repeats after every F_n cycles. We can compute the matrix that corresponds to the evolution for one period and determine the dynamics from the trace.

The phase structures for different values of n and θ are shown in Fig. 32, which shares a lot of similarity with the Fibonacci case but also has some differences. Given n, the region for the nonheating phase gradually decreases as θ increases. Given θ, the nonheating region splits into many "bands." Notice that $T_1 = 0$ and $L_{\rm eff}$ are actually identified, the number of bands is exactly equal to F_n when F_n is even and $F_n - 1$ when F_n is odd. If one computes the Lyapunov exponent for a fixed n, it shows peaks with equal spacing, as shown in Fig. 32(d). It implies that as $\omega \to (\sqrt{5}-1)/2$, the self-similarity structure will not appear as in the Fibonacci case. The reason why the peaks have equal spacing will be explained later.

We can also check explicitly the measure of the nonheating phase as approaching the quasiperiodic limit. Following the same prescription as (114), we call $\sigma_n(\theta)$ the measure of the nonheating phase, which is a function of n and θ. The result is shown in Fig. 33(a). For a given θ, the measure is exponentially decaying at large n, similar to what we have found for the Fibonacci case. We introduce the decaying rate $\lambda(\theta)$ as $\sigma_n(\theta) \propto e^{-\lambda(\theta)n}$, and find that it does not have a strong dependence on θ.

These two features also hold for generic rational and irrational numbers and can be summarized by the following statements.

(1) If $\omega = p/q$ is a rational number with p, q being coprime, then the region for the nonheating phase splits into multiple bands. The number of bands depends on q as

$$\text{number of bands} = \begin{cases} q, & q \in 2\mathbb{Z} \\ q-1, & q \in 2\mathbb{Z}+1. \end{cases} \tag{159}$$

Note the periodic boundary condition in T_1 when we count the number of bands, namely, the first band and last band (in vertical order) are considered to be the same band.

(2) When $\omega = a_n/b_n$ approaches an irrational number as $n \to \infty$, the measure for the nonheating phase decreases exponentially with n.

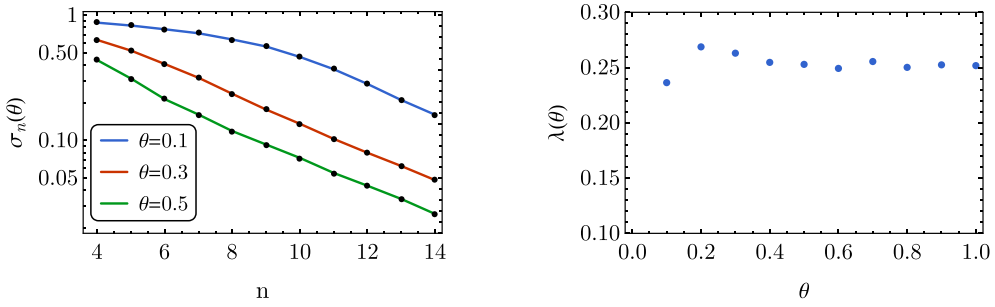

FIG. 33. (Left) The measure of the nonheating phase $\sigma_n(\theta)$. (Right) The decay rate $\lambda(\theta)$ as a function of θ. For the curve with $\theta = 0.1$, only the data for $n \geqslant 8$ are used for the fitting.

The second statement is only empirical and based on the numerical observation. The first statement can be understood by a perturbative argument as follows.

Perturbative proof of the statement 1. Let us assume $\omega = p/q$ and analyze the matrix of the unitary evolution for one period, which consists of q cycles. Notice that L and L_{eff} are merely the units for T_0 and T_1, we can set both of them to be 1 without changing the physics.

We first consider the limit $\theta = 0$, so that M_0 and M_1 are both diagonal matrices of pure phases. For the kth cycle of the period, $T_0 = k\frac{p}{q}$ and we have

$$M_{(k)}^{(0)} = M_0(T_0)M_1(T_1;\theta=0) = \begin{pmatrix} e^{i\pi(kp/q+T_1)} & \\ & e^{-i\pi(kp/q+T_1)} \end{pmatrix}. \tag{160}$$

The lower index denotes the cycle and the upper index means it is the zeroth-order term in the small-θ expansion. The matrix for the whole period $\Pi_q^{(0)} = M_{(1)}^{(0)}M_{(2)}^{(0)}\dots M_{(q)}^{(0)}$ and its trace can be easily computed, and we have

$$|\operatorname{Tr}\Pi_q^{(0)}| = \begin{cases} 2|\sin q\pi T_1| & q \in 2\mathbb{Z}, \\ 2|\cos q\pi T_1| & q \in 2\mathbb{Z}+1, \end{cases} \tag{161}$$

where we have used the condition that p and q are coprime. A typical curve for $|\operatorname{Tr}\Pi_q^{(0)}|$ is shown in Fig. 34(a). Therefore, even without adding θ, the trace can touch the critical value $|\operatorname{Tr}\Pi_q| = 2$ at the following positions:

$$\begin{aligned} q \in 2\mathbb{Z}: &\quad T_1 = \frac{1}{q}\left(r+\frac{1}{2}\right), \quad r = 0,1,\dots,q-1; \\ q \in 2\mathbb{Z}+1: &\quad T_1 = \frac{r}{q}, \quad r = 0,1,\dots,q-1. \end{aligned} \tag{162}$$

Note that T_1 has a period 1, which fixes the range of r.

Then, we turn on a tiny θ and consider its contribution to $\operatorname{Tr}\Pi_q$ perturbatively. In particular, if $|\operatorname{Tr}\Pi_q|$ exceeds 2 for a certain range of T_1, a heating phase appears there and will continue to exist for larger θ. At small θ, such thing is more likely to happen at those special positions where $|\operatorname{Tr}\Pi_q^{(0)}|$ already touches 2. A numerical calculation for all small values of q confirms that such thing does always happen. One typical example is shown in Fig. 34(b). For large q, we consider the following perturbative calculation. Each $M_{(k)}$ can be expanded to the second order in θ:

$$\begin{aligned} M_{(k)} &= M_{(k)}^{(0)} + \theta M_{(k)}^{(1)} + \theta^2 M_{(k)}^{(2)} + \mathcal{O}(\theta^3), \\ M_{(k)}^{(1)} &= 2i\,\sin\pi T_1 \begin{pmatrix} & -e^{i\pi kp/q} \\ e^{-i\pi kp/q} & \end{pmatrix}, \\ M_{(k)}^{(2)} &= 2i\,\sin\pi T_1 \begin{pmatrix} e^{i\pi kp/q} & \\ & -e^{-i\pi kp/q} \end{pmatrix}. \end{aligned} \tag{163}$$

The first nonvanishing contribution comes from the second order of θ, which has two terms. One is the cross term of $M_{(k)}^{(1)}$, the other only contains $M_{(k)}^{(2)}$. In the limit of large q, the second

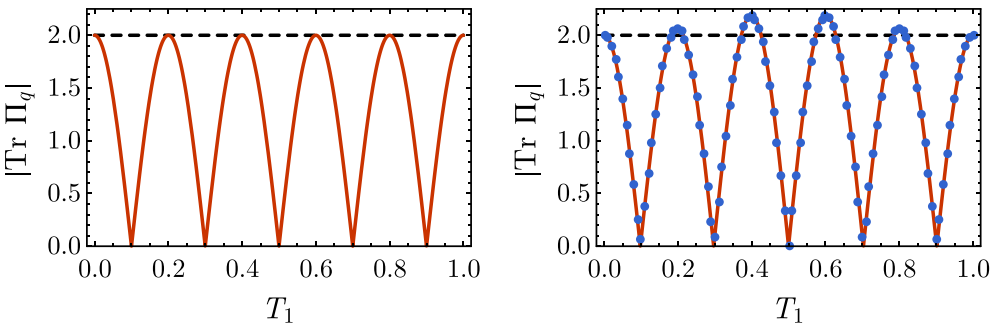

FIG. 34. The absolute value of the trace of the matrix for one period with $\theta = 0$ (left) and $\theta = 0.1$ (right). We choose $p = 2$, $q = 5$ for both plots. In (b), the blue dots are the approximated result in Eq. (164). It matches the exact value quite well.

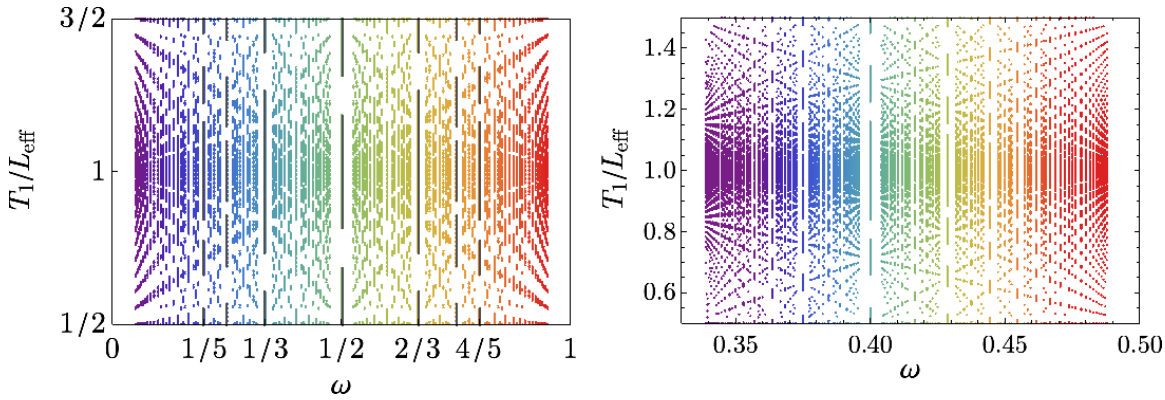

FIG. 35. The phase diagram for the Aubry-André quasiperiodic driving CFT. The plot uses $\theta = 0.2$ and includes all the rational number whose denominators are equal or less than 20. The usage of different colors is only for the purpose of presentation and has no physical meaning. We shift the origin of $T_1/L_{\rm eff}$ by $\frac{1}{2}$ when presenting the data.

term dominates and we have

$$\mathrm{Tr}\,\Pi_q \approx 2\,\cos\left(\pi q T_1 + \pi\frac{p(q+1)}{2}\right) - 4q\theta^2 \sin\pi T_1 \sin \times\left(\pi(q-1)T_1 + \pi\frac{p(q+1)}{2}\right). \tag{164}$$

Notably, this is a good approximation even for small q, the $q = 5$ case is shown in Fig. 34(b) as an illustration. If q is an odd number, one can check that at those special positions $T_1 = r/q$, we have

$$\mathrm{Tr}\,\Pi_q|_{T_1=r/q} = (-1)^{r+p(q+1)/2}\left[2+4\theta^2 q\left(\sin\frac{\pi r}{q}\right)^2\right], \tag{165}$$

from which we can see that the value of $|\mathrm{Tr}\,\Pi_q|$ indeed exceeds 2 except at $r = 0$ ($T_1 = 0$). The proof for q being even is similar and one can find that $|\mathrm{Tr}\,\Pi_q|$ exceeds 2 for all $T_1 = (r + \frac{1}{2})/q$.

So far, we have perturbatively shown that $|\mathrm{Tr}\,\Pi_q|$ will exceed 2 at some equally spaced special positions. Therefore, the heating phase will appear there as long as one turns on θ, which accordingly opens "gaps"' in the phase structure. This gives rise to the multiple bands of the nonheating phase and also explains the equally spaced peaks observed for the Lyapunov exponent. Furthermore, when q is even, gaps will appear at all those special positions which leads to q disconnected bands. When q is odd, the gap cannot appear at $T_1 = 0$ which yields $q - 1$ bands (after identifying $T_1/L_{\rm eff} = 0$ with $T_1/L_{\rm eff} = 1$). This completes the proof of our first statement. ■

3. Phase diagram and nested structure

We can also study the phase diagram for generic ω including both rational and irrational numbers. The result is shown in Fig. 35, with the colored region being the nonheating phase and blank region being the heating phase. Here are some comments on the features of the phase diagram:

(1) The whole diagram is symmetric with respect to $\omega = \frac{1}{2}$, which is a direct consequence of our analysis above. Namely, for a rational number $\omega = p/q$, the gap opening is independent of the numerator, which implies that the phase diagram should be invariant under $p/q \to 1 - p/q$. Our following discussion will focus on the part $\omega \leqslant \frac{1}{2}$.

(2) The diagram has (infinitely) many empty regions, whose center is at simple rational numbers $\omega = 1/n$, $n \geqslant 2$. Some representatives are drawn explicitly by the gray lines in Fig. 35. The reason why they all sit in the relative empty region is that one has to use a rational number with large denominator to approach one of them, the nonheating bands of which are too fragmented to read by eyes.

(3) In-between every two neighboring simple rationals, the structure of the subregion resembles the original phase diagram. This implies that the phase diagram has a nested structure, which is similar to the famous Hofstadter butterfly [61] and can be understood in the following way.

As reviewed in Appendix B, every rational and irrational number $\omega \in [0, 1]$ can be uniquely represented by a continued fraction. Here we adopt the idea and consider a generalization

$$\omega = \frac{1}{N_1 \pm \frac{1}{N_2 \pm \cdots}}, \quad N_i = 2, 3, \ldots . \tag{166}$$

We will see that it provides a useful guidance to resolve the diagram layer by layer. Those with only N_1 being nonzero are dubbed as the principal series, those with nonzero N_1, N_2 as the first descendants and so on.

The nested structure of the phase diagram exactly follows such an organization:

(1) First, the principal series $\{1/N_1\}, N_1 = 2, 3, \ldots$ form the skeleton of the phase diagram, which is shown in Fig. 36(a). They also sit in the relatively empty region in the full phase diagram.

(2) The first descendants $\{\frac{1}{N_1 \pm \frac{1}{N_2}}\}$ fill in the blank region between the principal series and serves as the skeleton for the next descendants. For example, $\frac{1}{2+1/N_2}$ and $\frac{1}{3-1/N_2}$ fill the region between $\frac{1}{3}$ and $\frac{1}{2}$, as shown in Fig. 36(b).

(3) Notice that all the descendants of $\frac{1}{2}$ that are smaller than $\frac{1}{2}$ are $\frac{1}{2+p/q}$, $1 < p < q$. Similarly all the descendants of $\frac{1}{3}$ that are larger than $\frac{1}{3}$ are $\frac{1}{3-p/q}$, $1 < p < q$, which can also be written as $\frac{1}{2+(1-p/q)}$. These two series, filling the subregion between $\omega = \frac{1}{3}$ and $\frac{1}{2}$, can be considered as the "mirror reflection" to each other with $\omega = \frac{2}{5}$ being the reflection center. This is similar to what is observed for the full diagram, with the difference that each pair $\{\frac{1}{2+p/q}, \frac{1}{2+(1-p/q)}\}$ does not have the

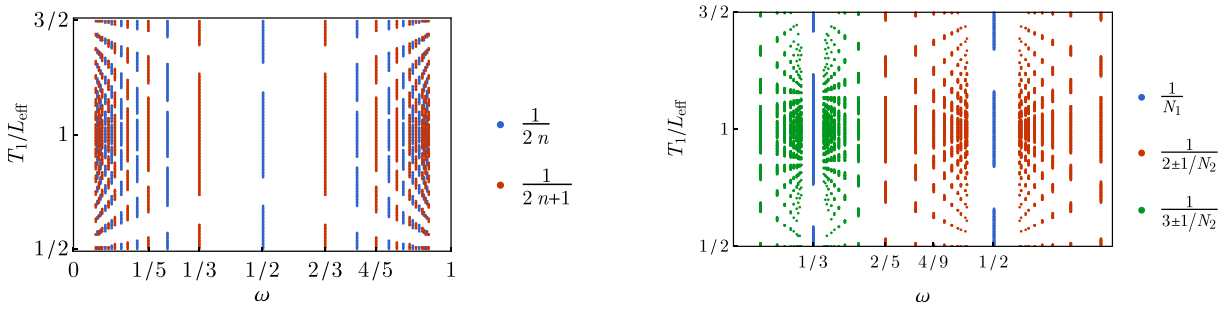

FIG. 36. The nested structure of the phase diagram for the Aubry-André quasiperiodic driving CFT, with the principal series (left) and the first descendant (right).

same number of bands. This explains the similarity and also difference between Figs. 35(a) and 35(b). The nested structure follows from continuing such kind of game.

4. Features of the group walking

So far, the results resemble what have been found for the well-known Aubry-André model or almost Mathieu operator. The unique advantage of our CFT setup is that it brings physical meaning to the group walking. As discussed in Sec. III B, the group walking of ρ and $\rho\zeta$ are related to the energy, energy-momentum density, and the entanglement. We will give a corresponding discussion in this section.

To illustrate the general feature, let us choose the inverse golden ratio $\omega = \frac{\sqrt{5}-1}{2}$ as a concrete example. The results are shown in Fig. 37. The behavior of ρ has the same qualitative feature as reported in the Fibonacci driving case. Namely, for a generic choice of T_1/L_{eff}, ρ will flow exponentially close to a certain point on $\partial\mathbb{D}$ in the long-time limit $n \to \infty$. It follows from Eqs. (49) and (45) that the entanglement entropy and total energy have a linear and exponential growth, respectively, which is consistent with our general claim for the heating phase.

The behavior of $\rho\zeta$ is quite different. In the short time, $\rho\zeta$ seems to have a random distribution in the disk. In the late time, it flows onto $\partial\mathbb{D}$, which implies the formation of energy-momentum peaks. Although $(\rho\zeta)_n$ and $(\rho\zeta)_{n+1}$ do not show a strong correlation, as shown by the background scattered dots in Fig. 37(b), the subsequence $\{(\rho\zeta)_{k+F_n}\}$, $n \geqslant 1$, for any fixed k does have a definite limit as $n \to \infty$ and the detailed value of the limit depends on k. Physically, it means that the peaks observed at the time $k + F_n$ with fixed k will appear at the same position.

Such behavior of $\rho\zeta$ is generic as long as the irrational number is $\omega = (\sqrt{r^2+4} - r)/2$, $r = 1, 2, \ldots$. For example, one will observe the same feature if choosing $\omega = \sqrt{2} - 1$, $(\sqrt{13} - 4)/2$, and so on. An intuitive reason is that the nth principal convergent for this type of irrational numbers can be written as b_{n-1}/b_n. (For the inverse golden ratio, b_n is the nth Fibonacci number.) Such a sequence b_n provides us with a natural choice of the observation time. For a generic irrational number, its nth principal convergent is p_n/q_n with $\{p_n\}, \{q_n\}$ being two different sequences and a "natural choice" of the observation time becomes less clear.

VI. DISCUSSION

In this paper, we propose a general framework to study the nonequilibrium dynamics of $(1+1)$D CFTs with SL_2 deformation. We examine the details of the dynamical phases that emerge in the periodic and quasiperiodic driving using the

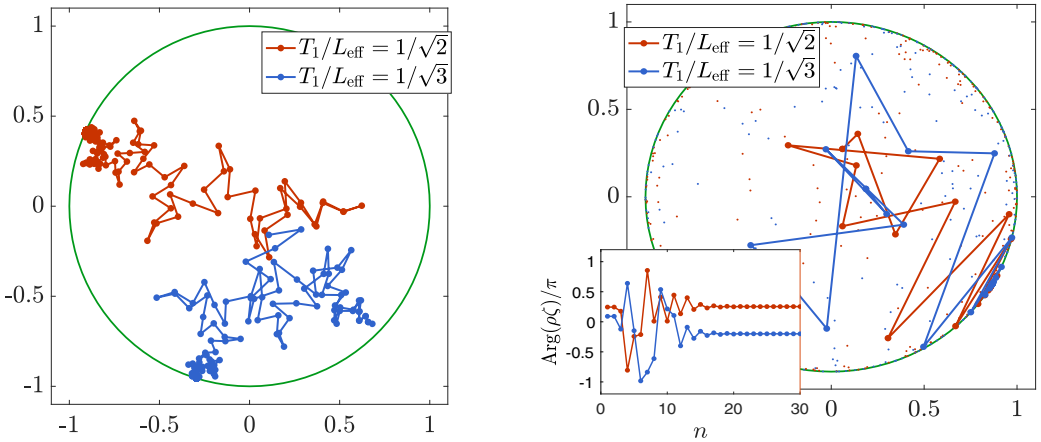

FIG. 37. The group walking of ρ (left) and $\rho\zeta$ (right). We choose ω being $(\sqrt{5}-1)/2$ and $\theta = 0.1$. The choice for T_1/L_{eff} is not special, and one can choose any other generic values. In the numerics, we choose $\omega = F_{29}/F_{30}$ as an approximation to plots (a) and (b). In (b), the scattered dots in the circle represent $(\rho\zeta)_n$ for $n \leqslant 500$. The inset of (b) is $\text{Arg}(\rho\zeta)/\pi$ as a function n, with n denoting the nth Fibonacci number F_n.

tools we propose. In the upcoming sequel of this paper [62], we will apply the framework to the random driving sequence, where the use of the Lyapunov exponent and group walking becomes a necessity rather than a convenient option.

Here we highlight some of the unexpected features that we have found:

(1) For the driving protocol that uses the SL_2 deformed Hamiltonian, when the total energy and entanglement start to grow, they always grow in a pattern where energy is concentrated in discrete points and forms peaks, while the entanglement is shared within nearest neighbors. This phenomenon was first observed in Ref. [56] and is found to persist in the more general setting here.

(2) Introducing irregularity in the driving protocol usually enlarges the heating phase, which is what we have observed in the quasiperiodic driving where the nonheating regime shrinks to a set with measure zero.[26] However, for the *Fibonacci* driving, the phase diagram is found to have a special nonheating fixed point, where the total energy and entanglement will return in a pattern following the Fibonacci sequence.

More explicitly, if we observe the system only at the steps coinciding with the Fibonacci numbers, what we see is a state returning to itself with period 6.

It is worth to mention that if we pick out the two unitaries U_A and U_B that underlie the aforementioned Fibonacci driving, and apply them in a periodic fashion $U_AU_BU_AU_BU_AU_B\ldots$, the system will end up with a heating state. This is a surprise since it implies that at this special point, the "irregularity" actually converts the heating protocol to a nonheating one. The reason is that the pattern in the Fibonacci driving sequence manages to conspire with the special unitaries in a way that they happen to cancel each other and result in a return, which is explained in Sec. V B 4.

(3) Aside from the last point, the "order" of the quasiperiodic driving manifests itself in another way. In the heating phase of the quasiperiodic driving, ordinary stroboscopic observation of the energy peaks is featureless. However, if we consider the Fibonacci driving and observe the state at the steps coinciding with the Fibonacci numbers, the energy peaks oscillate between two fixed positions rather than randomly distribute (which is what we expect for a general irregular driving). Similar feature is also observed in the Aubry-André driving, where the energy peaks return to the same positions.

In the rest of this Discussion, we would like to comment on the special setting we use and some future directions. SL_2 deformation[27] is kind of a "shortcut" in analyzing the driven systems because its effect in a single driving period can be characterized by a conformal transformation without introducing external sources to the system. The simplicity of the single driving allows us to pursue the "complexity" in the pattern of the driving sequence as we do in this paper. For future directions, note the following:

(1) Within the SL_2 deformation framework: So far we have been only probing the driven state by simple observables such as one-point function of energy-momentum tensor for energy distribution or two-point function of twist operator for the entanglement entropy, both of which only depend on the central charge. To explore more CFT data such as the operator content and the OPE coefficients, we need to consider more complicated observables. For example, we may consider measuring multipoint functions during the driving and ask how could a carefully designed driving protocol help us extract more CFT data.

(2) Beyond the SL_2 deformation framework: The deformation of driving Hamiltonians considered in this work is generated by SL_2 algebra. Most recently, the periodically driven CFTs are generalized to the cases where the driving Hamiltonians are deformed by arbitrary smooth functions [82,83]. The underlying algebra is the infinite-dimensional Virasoro algebra. It is found that both the heating and nonheating phases can still be observed in general. In particular, the phase diagrams are determined by whether there are emergent spatial fixed points in the operator evolution. If there exist spatial fixed points, then the driven system is in the heating phase; otherwise, the system is in the nonheating phase.

However, it is not obvious what will happen when we perturb the driving Hamiltonian by introducing operators other than energy momentum in the driving Hamiltonian. In general, if the driving Hamiltonians break the conformal symmetry, we expect that the system will finally be thermalized.

Another related question is that if we treat the CFT we have as a low-energy effective theory, then in the heating phase we will finally drive the system to an energy scale where we need to consider its UV completion, i.e., we need to include some irrelevant operators in the driving Hamiltonian. We could ask what will happen at that point? For example, how does the energy peak and entanglement pattern get modified? These questions are relevant in explaining the data from lattice simulation beyond the conformal regime.

(3) It is also desirable to consider the possible experimental realization of our setup. Since our driving Hamiltonians are inhomogeneous in space, we expect it is natural to study the physics here in the cold-atom experiments, where the interactions among cold atoms can be optically controlled [84,85]. In experiments, the dissipation effects caused by environments need to be considered [86]. It is expected that the physics studied in this work can be observed if the timescale is shorter than the decoherence time.

Note added. Recently, we learned that the Fibonacci quasiperiodically driven CFT is also studied in [87]. We thank the authors for sending us their manuscript before posting.

ACKNOWLEDGMENTS

We thank for helpful discussions with B. Han, D. Jafferis, E. Khalaf, I. Martin, S. Ryu, H. Shapourian, T. Tada, M. Widom, J.-Q. Wu, Y. Zhang, and D. Zhou. In particular, we thank Y. Zhang for suggestions on the study of the quasiperiodic driving CFTs, and thank M. Widom for pointing out Ref. [68], which stimulated our interest in considering the Fibonacci sequence in quasiperiodically driven CFTs. X.W. is supported by the Gordon and Betty Moore Foundations EPiQS initiative through Grant No.GBMF4303 at MIT. Y.G. is supported by the Gordon and Betty Moore Foundation

[26]For Fibonacci driving with SSD Hamiltonian, we prove it is a Cantor set by mapping to the quasicrystal.

[27]Or, more generally "Virasoro deformation" which involves modulation with multiple wavelengths.

EPiQS Initiative through Grant No. GBMF-4306 and DOE Grant No. de-sc0019030. A.V. and R.F. are supported by the DARPA DRINQS program (Award No. D18AC00033) and by a Simons Investigator Award.

APPENDIX A: MORE ON TIME-DEPENDENT DRIVEN CFTs

In this Appendix, we give more details on some formulas and results as used in the main text.

1. Operator evolution with arbitrary SL_2 deformations

In this Appendix, we introduce the procedures of obtaining the concrete form of Möbius transformation in Eq. (21) in the main text. Some related details can be found in Refs. [41,48,56,65,66]. Let us illustrate the calculation with a simple example, and then give results for an arbitrary SL_2 deformation.

The illustrative example we consider has the following deformed Hamiltonian:

$$H_{\text{deform}} = \int_0^L f(x)\, T_{00}(x) dx, \quad \text{with } f(x) = 1 - \tanh(2\theta)\cos\frac{2\pi q x}{L}, \quad \theta > 0,\ q \in \mathbb{Z}, \tag{A1}$$

where $T_{00}(x)$ is the Hamiltonian density with $T_{00}(x) = \frac{1}{2\pi}[T(x) + \overline{T}(x)]$. For $q = 1$ with open boundary conditions, this corresponds to the example we considered in Secs. IV D, V A, and V D. To study the Möbius transformation in Eq. (21), our derivations below apply to both periodic and open boundary conditions. First, it is noted that H_{deform} can be written in terms of the Virasoro generators in Eq. (10) as

$$H_{\text{deform}} = \frac{2\pi}{L}\left[L_0 - \tanh(2\theta)\frac{L_q + L_{-q}}{2} - \frac{c}{24}\right] + \text{antichiral parts}. \tag{A2}$$

As a remark, for $\theta = 0$, H_{deform} corresponds to a uniform one without any deformation; for $\theta = \infty$, H_{deform} corresponds to a SSD Hamiltonian, whose energy spectrum has been recently studied in detail in Refs. [45–47,49].

To evaluate the correlation function, such as the simplest one $\langle\Psi(t)|\mathcal{O}(x)|\Psi(t)\rangle$, where $|\Psi(t)\rangle = e^{-iH_{\text{deform}}t}|\Psi_0\rangle$, one can study the operator evolution $\mathcal{O}(x,t) = e^{iH_{\text{deform}}t}\mathcal{O}(x)e^{-iH_{\text{deform}}t}$, as follows.

The correlation function $\langle\Psi(t)|\mathcal{O}(x)|\Psi(t)\rangle$ can be considered as the path integral on a w cylinder with the operator $\mathcal{O}$ inserted, as depicted in Fig. 4, where $w = \tau + ix$. This cylinder can be mapped to a q-sheet Riemann surface with a conformal map $z = e^{\frac{2\pi q w}{L}}$ (see Fig. 4). The energy-momentum tensor transforms as $T_{\text{cyl}}(w) = (\frac{dw}{dz})^{-2}[T(z) - \frac{c}{12}\{w,z\}]$, with $\{w,z\} = \frac{d^3w/dz^3}{dw/dz} - \frac{3}{2}(\frac{d^2w/dz^2}{dw/dz})^2$. Then, one can find that $T_{\text{cyl}}(w) = (\frac{2\pi z}{l})^2[T(z) - \frac{c}{24}\frac{1}{z^2}]$, where we have defined $l := L/q$. Then, the Hamiltonian in Eq. (A1) can be written as $H = H^{(z)} + H^{(\bar{z})}$, where

$$H^{(z)} = \frac{2\pi}{l\,\cosh(2\theta)}\oint\frac{1}{2\pi i}\left[\cosh(2\theta)z - \frac{\sinh(2\theta)}{2}(z^2+1)\right]T(z)dz - \frac{\pi c}{12l}. \tag{A3}$$

A further Möbius transformation $\widetilde{z} = \frac{-\cosh(\theta)z + \sinh(\theta)}{\sinh(\theta)z - \cosh(\theta)}$ will transform $H^{(z)}$ to the following simple form:

$$H^{(\widetilde{z})} = \frac{2\pi}{l_{\text{eff}}}\oint\frac{1}{2\pi i}\widetilde{z}\,T(\widetilde{z})\,d\widetilde{z} - \frac{\pi c}{12l}, \quad l_{\text{eff}} = l\,\cosh(2\theta), \tag{A4}$$

and similarly for the antiholomorphic part. On this $\widetilde{z}$ Riemann surface, the operator evolution becomes a dilatation: $e^{H^{(\widetilde{z})}\tau}\mathcal{O}(\widetilde{z},\overline{\widetilde{z}})e^{-H^{(\widetilde{z})}\tau} = \lambda^h\bar{\lambda}^{\bar{h}}\mathcal{O}(\lambda\widetilde{z},\bar{\lambda}\overline{\widetilde{z}})$, where $\lambda = e^{\frac{2\pi\tau}{l_{\text{eff}}}}$. Then by mapping back to the z surface, one can find the operator evolves as

$$e^{H^{(z)}\tau}\mathcal{O}(z,\bar{z})e^{-H^{(z)}\tau} = \left(\frac{\partial z'}{\partial z}\right)^h\left(\frac{\partial\bar{z}'}{\partial\bar{z}}\right)^{\bar{h}}\mathcal{O}(z',\bar{z}'), \quad \text{where} \quad z' = \frac{az+b}{cz+d}. \tag{A5}$$

By imposing the normalization condition $ad - bc = 1$, and doing an analytical continuation $\tau = it$, one has

$$z' = \frac{\alpha z + \beta}{\beta^* z + \alpha^*}, \tag{A6}$$

where $\alpha = \cos(\frac{\pi t}{l_{\text{eff}}}) + i\,\cosh(2\theta)\sin(\frac{\pi t}{l_{\text{eff}}})$ and $\beta = -i\,\sinh(2\theta)\sin(\frac{\pi t}{l_{\text{eff}}})$. When $q = 1$ such that $l = L$, we get the result as presented in Eq. (72) in the main text.

It is straightforward to generalize the above approach to the cases with arbitrary SL_2 deformations. A general result was recently calculated in Refs. [65,66]. Let us cite and briefly summarize the results here. First, for arbitrary SL_2 deformations in Eq. (13), the deformed Hamiltonian can be written as $H_{\text{deform}} = H^{\text{chiral}}_{\text{deform}} + H^{\text{antichiral}}_{\text{deform}}$, with $H^{\text{chiral}}_{\text{deform}}$ given in Eq. (14), which we rewrite here:

$$H^{\text{chiral}}_{\text{deform}} = \frac{2\pi}{L}(\sigma^0 L_0 + \sigma^+ L_{q,+} + \sigma^- L_{q,-}) - \frac{\pi c}{12L}, \tag{A7}$$

and similarly for the antichiral part. Here we have defined $L_{q,+} = \frac{1}{2}(L_q + L_{-q})$, and $L_{q,-} = \frac{1}{2i}(L_q - L_{-q})$. One can further define the quadratic Casimir element: $c^{(2)} := -(\sigma^0)^2 + (\sigma^+)^2 + (\sigma^-)^2$ [45,46,65,66], based on which one can classify the deformed

Hamiltonians in Eq. (A7) into three types:

$$\begin{aligned} c^{(2)} < 0: &\quad \text{elliptic Hamiltonian,} \\ c^{(2)} = 0: &\quad \text{parabolic Hamiltonian,} \\ c^{(2)} > 0: &\quad \text{hyperbolic Hamiltonian.} \end{aligned} \tag{A8}$$

Second, we consider the operator evolution $e^{iH_{\text{deform}}T}\mathcal{O}(z,\bar{z})e^{-iH_{\text{deform}}T}$ with the Hamiltonian in Eq. (A7) for a time interval T. Then, one can obtain the general form of operator evolution in Eqs. (A5) and (A6). The corresponding SU(1, 1) matrix $M = \left(\begin{smallmatrix}\alpha & \beta \\ \beta^* & \alpha^*\end{smallmatrix}\right)$ depends on the types of Hamiltonian in Eq. (A8) as follows [65,66]:

$$\begin{aligned} &\text{Elliptic:} \quad \alpha = -\cos\left(\frac{\mathcal{C}\pi T}{l}\right) - i\frac{\sigma^0}{\mathcal{C}}\sin\left(\frac{\mathcal{C}\pi T}{l}\right), \quad \beta = -i\frac{\sigma^+ + i\sigma^-}{\mathcal{C}}\sin\left(\frac{\mathcal{C}\pi T}{l}\right), \\ &\text{Parabolic:} \quad \alpha = -1 - i\frac{\sigma^0\pi T}{l}, \quad \beta = -i\frac{(\sigma^+ + i\sigma^-)\pi T}{l}, \\ &\text{Hyperbolic:} \quad \alpha = -\cosh\left(\frac{\mathcal{C}\pi T}{l}\right) - i\frac{\sigma^0}{\mathcal{C}}\sinh\left(\frac{\mathcal{C}\pi T}{l}\right), \quad \beta = -i\frac{\sigma^+ + i\sigma^-}{\mathcal{C}}\sin\left(\frac{\mathcal{C}\pi T}{l}\right), \end{aligned} \tag{A9}$$

where $\mathcal{C} = \sqrt{|-(\sigma^0)^2 + (\sigma^+)^2 + (\sigma^-)^2|}$ and $l = L/q$. One can check explicitly that for elliptic, parabolic, and hyperbolic Hamiltonians in Eqs. (A7) and (A8), the corresponding SU(1, 1) matrices in Eq. (A9) have the properties $|\text{Tr}(M)| < 2$, $|\text{Tr}(M)| = 2$, and $|\text{Tr}(M)| > 2$, respectively, as expected.

As a remark, the specific example in Eqs. (A1) and (A2) is always elliptic for finite θ, and parabolic for $\theta \to \infty$.

For the elliptic case in Eq. (A9), by choosing $T = \frac{l}{2\mathcal{C}}$, one has $M = \left(\begin{smallmatrix} -i\frac{\sigma^0}{\mathcal{C}} & -i\frac{\sigma^+ + i\sigma^-}{\mathcal{C}} \\ i\frac{\sigma^+ - i\sigma^-}{\mathcal{C}} & i\frac{\sigma^0}{\mathcal{C}} \end{smallmatrix}\right)$. This is a reflection matrix of the form in Eq. (79), with the property $\text{Tr}(M) = 0$ and $M^2 = (M^{-1})^2 = -\mathbb{I}$. Given two arbitrary reflection matrices M_A and M_B ($M_B \neq \pm M_A$), as discussed in Ref. [88], there exists a SU(1, 1) matrix V such that $VM_AV^{-1} = \left(\begin{smallmatrix}-i & 0 \\ 0 & i\end{smallmatrix}\right)$, and $VM_BV^{-1} = \left(\begin{smallmatrix}\alpha & \beta \\ \beta^* & \alpha^*\end{smallmatrix}\right)$, where $|\alpha|^2 - |\beta|^2 = 1$ and $\alpha, \beta \in \mathbb{C}$. Since M_B is a reflection matrix and $M_B \neq \pm M_A$, then we have $\text{Tr}(VM_BV^{-1}) = \text{Tr}(M_B) = 0$, which indicates that $VM_BV^{-1} = \left(\begin{smallmatrix} ia & \beta \\ \beta^* & -ia \end{smallmatrix}\right)$, where $a \in \mathbb{R}$, $a^2 - |\beta|^2 = 1$, and $\beta \neq 0$. Then one can check $\text{Tr}(M_AM_B) = \text{Tr}(VM_AV^{-1}VM_BV^{-1}) = 2a$. Since $a^2 = 1 + |\beta|^2 > 1$, we always have $|\text{Tr}(M_AM_B)| > 2$, i.e., M_AM_B is a hyperbolic matrix. These properties will be useful in the study of the nonheating fixed point in a Fibonacci driven CFT in Sec. V B 4.

2. Time evolution of two-point correlation functions

In this Appendix, we study the time evolution of equal-time two-point correlation functions. Aside from the time evolution of entanglement entropy and energy, this quantity can also be used to detect different phases of the dynamics.

We consider the two-point correlation function $\langle\Psi_n|\mathcal{O}(x_1)\mathcal{O}(x_2)|\Psi_n\rangle$, where $|\Psi_n\rangle$ is the wave function after n steps of driving and $\mathcal{O}(x)$ is a general primary field with conformal dimension $(h, \bar{h})$. One can further obtain the correlation functions for descendants of $\mathcal{O}$. Here, $\mathcal{O}(x_i)$ is defined on the space-time cylinder. We do the computation in the imaginary time and thus use the coordinate $w = \tau + ix$. Let us consider a conformal mapping $z = e^{\frac{2\pi q w}{L}} = e^{\frac{2\pi w}{l}}$ to map the w cylinder to the q-sheet z-Riemann surface (see Fig. 4), on which the operator evolution of $\mathcal{O}(z_1)$ and $\mathcal{O}(z_2)$ is determined by Eqs. (24), (A6), and (A9). Next, we map the q-sheet z-Riemann surface to the complex ζ plane via a conformal mapping $\zeta = z^{1/q}$, and one can obtain

$$\langle\Psi_n|\mathcal{O}(w_1,\overline{w}_1)\mathcal{O}(w_2,\overline{w}_2)|\Psi_n\rangle = \prod_{i=1,2}\left(\frac{\partial\zeta_i}{\partial w_i}\right)^h \prod_{i=1,2}\left(\frac{\partial\overline{\zeta}_i}{\partial\overline{w}_i}\right)^{\overline{h}} \langle\mathcal{O}(\zeta_1,\overline{\zeta}_1)\mathcal{O}(\zeta_2,\overline{\zeta}_2)\rangle_\zeta, \tag{A10}$$

where $w_j = 0 + ix_j$, and $(h, \bar{h})$ are the conformal dimensions of the operator $\mathcal{O}$. More explicitly, the contribution of the holomorphic part in Eq. (A10) can be expressed in terms of the SU(1, 1) matrix elements in Eq. (25) as follows:

$$\left(\frac{2\pi}{L}\right)^{2h} \frac{z_1^h}{(\beta_n^* z_1 + \alpha_n^*)^{2h}} \frac{z_2^h}{(\beta_n^* z_2 + \alpha_n^*)^{2h}} \left(\frac{\alpha_n z_1 + \beta_n}{\beta_n^* z_1 + \alpha_n^*}\right)^{(\frac{1}{q}-1)h} \left(\frac{\alpha_n z_2 + \beta_n}{\beta_n^* z_2 + \alpha_n^*}\right)^{(\frac{1}{q}-1)h} \left[\left(\frac{\alpha_n z_1 + \beta}{\beta_n^* z_1 + \alpha_n^*}\right)^{\frac{1}{q}} - \left(\frac{\alpha_n z_2 + \beta}{\beta_n^* z_2 + \alpha_n^*}\right)^{\frac{1}{q}}\right]^{-2h}, \tag{A11}$$

where $z_i = e^{\frac{2\pi w_i}{l}}$. The contribution of the antiholomorphic part can be obtained by replacing $\alpha_n \to \alpha_n'$, $\beta_n \to \beta_n'$, and $z_i \to \overline{z}_i$ in the above equation. Noting that z lives on a q-sheet Riemann surface (see Fig. 4), one should be careful when evaluating Eq. (A11), by tracking if z_i cross the branch cuts and move from one layer to another. This is subtle but important especially when the system is in a heating phase. The relative distance between z_1 and z_2 will depend on whether there are energy-momentum density peaks between them [56].

As an illustration, we study the two-point correlation functions in the heating and nonheating phases of a periodically driven CFT, respectively. For simplicity, we only drive the holomorphic part, and keep the antiholomorphic parts untouched. In the nonheating phase, as discussed in Sec. IV, α_N and β_N are periodic functions of n [see Eq. (50)], and so are the correlation functions. In the heating phase, the Lyapunov exponent is positive, i.e., $\lambda_L > 0$. In this case, peaks of energy density will form in the real space. In particular, when there are energy density peaks between x_1 and x_2 (and x_1 and x_2 are not located at the centers of the energy density peaks), one can find that in the long-time limit $\lambda_L N \gg 1$ (recall that the total number of driving steps is $N = np$, where p is the period of driving steps),

$$\frac{\langle\Psi_n|\mathcal{O}(x_1)\mathcal{O}(x_2)|\Psi_n\rangle}{\langle\Psi_0|\mathcal{O}(x_1)\mathcal{O}(x_2)|\Psi_0\rangle} \simeq e^{-2\lambda_L h N}\left(\frac{L}{\pi}\sin\frac{\pi(x_1-x_2)}{L}\right)^{-2h}. \tag{A12}$$

That is, the correlation function decays exponentially as a function of the driving time. Recently, this result is generalized in the heating phase of more general cases where the driving Hamiltonians are deformed by an arbitrary smooth function. See Ref. [82] for more details.

3. Entanglement entropy evolution

In this Appendix, we give some details on the time evolution of the entanglement entropy in a time-dependent driven CFT.

a. General formula

We give a derivation of Eq. (27) in the main text. The mth Renyi entropy of $A = [x_1, x_2]$ can be obtained by studying the correlation function of twist operators:

$$S_A^{(m)}(n) = \frac{1}{1-m}\log\langle\Psi_n|\mathcal{T}_m(x_1)\overline{\mathcal{T}}_m(x_2)|\Psi_n\rangle, \tag{A13}$$

where $|\Psi_n\rangle$ denotes the wave function after n steps of drivings, and $\mathcal{T}_m$ ($\overline{\mathcal{T}}_m$) are primary operators with conformal dimensions $h = \bar{h} = \frac{c}{24}(m - \frac{1}{m})$. The evaluation of Eq. (A13) follows the previous Appendix A 2 directly and we have

$$\langle\Psi_n|\mathcal{T}_m(w_1,\overline{w}_1)\overline{\mathcal{T}}_m(w_2,\overline{w}_2)|\Psi_n\rangle = \prod_{i=1,2}\left(\frac{\partial\zeta_i}{\partial w_i}\right)^h\prod_{i=1,2}\left(\frac{\partial\overline{\zeta}_i}{\partial\overline{w}_i}\right)^{\bar{h}}\langle\mathcal{T}_m(\zeta_1,\overline{\zeta}_1)\overline{\mathcal{T}}_m(\zeta_2,\overline{\zeta}_2)\rangle_\zeta, \tag{A14}$$

where $w_i = 0 + ix_i$ are the coordinates in the imaginary time and $z_i = e^{2\pi q w/l}$, $\zeta_j = z_j^{1/q}$. We choose the subsystem within one deformation wavelength as $A = [(k-1/2)l, (k+j-1/2)l]$ or $A = [kl, (k+j)l]$ where $k,\ j \in \mathbb{Z}$, $j < q$, and $l = L/q$. In this case, z_1 ($\bar{z}_1$) and z_2 ($\bar{z}_2$) always live on different layers labeled by j. Let us take $A = [(k-1/2)l, (k+j-1/2)l]$ for example. Based on Eqs. (A11) and (A14), one can check explicitly that

$$\langle\Psi_n|\mathcal{T}_m(w_1,\overline{w}_1)\overline{\mathcal{T}}_m(w_2,\overline{w}_2)|\Psi_n\rangle = \left(\frac{2\pi}{L}\right)^{4h}\frac{1}{|\alpha_n-\beta_n|^{4h}}\frac{1}{|\alpha_n'-\beta_n'|^{4h}}\frac{1}{\left(2\sin\frac{\pi j}{q}\right)^{4h}}. \tag{A15}$$

Using $h = \bar{h} = \frac{c}{24}(m - \frac{1}{m})$ and Eq. (A13), we can obtain

$$S_A^{(m)}(n) - S_A^{(m)}(0) = \frac{c}{6}\frac{1+m}{m}(\log|\alpha_n-\beta_n| + \log|\alpha_n'-\beta_n'|), \tag{A16}$$

which reduces to Eq. (27) for $m \to 1$.

With the same procedure, if one chooses the subsystem as $A = [kl, (k+j)l]$ where $k,\ j \in \mathbb{Z}$ and $j < q$, then one can obtain $S_A^{(m)}(n) - S_A^{(m)}(0) = \frac{c}{6}\frac{1+m}{m}(\log|\alpha_n+\beta_n| + \log|\alpha_n'+\beta_n'|)$. The difference between this result and Eq. (A16) reflects the nonuniform property of the driven CFT.

b. Linear decrease of the entanglement entropy

In this Appendix, we show that if the subsystem is chosen in such a way that the two entanglement cuts lie on the centers of two chiral (antichiral) energy-momentum density peaks, and at the same time we keep the antichiral (chiral) part *undriven*, then the entanglement entropy may decrease in time. The choice of subsystem A can be understood as follows:

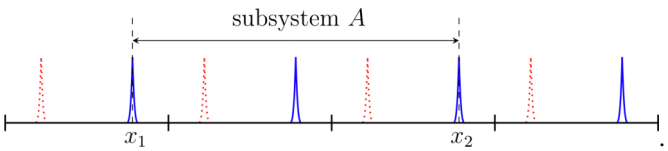

(A17)

Let us consider the setup of periodically driven CFT in Sec. IV, such that the locations of peaks are fixed in the long-time driving limit. Without loss of generality, we drive the chiral modes in time, but keep the antichiral modes undriven. As seen

from Eq. (66), the distance between two chiral energy-momentum density peaks is $x_{\text{peak},2} - x_{\text{peak},1} = jl$, where $j \in \mathbb{Z}$, $j < q$, and $l = L/q$. In addition, since the locations of peaks correspond to the fixed point γ_2 (i.e., $z_{\text{peak}} = \gamma_2$, where we have assumed $0 < \eta < 1$) in Eq. (54), this means $x_{\text{peak},1}$ and $x_{\text{peak},2}$ will not move around in the stroboscopic sense. Then, based on Eqs. (A14) and (A11), one can find that

$$\langle \Psi_n | \mathcal{T}(w_1, \overline{w}_1) \overline{\mathcal{T}}(w_2, \overline{w}_2) | \Psi_n \rangle = \left(\frac{2\pi}{L}\right)^{4h} \frac{1}{(\alpha_{np}\gamma_2 + \beta_n)^{2h} (\beta^*_{np}\gamma_2 + \alpha^*_n)^{2h}} \frac{1}{\left(2 \sin \frac{\pi j}{q}\right)^{4h}} \frac{1}{(\gamma_2^*)^{2h}}. \tag{A18}$$

Now, by considering the expressions of α_{np} and β_{np} in Eq. (58), one can find that

$$\alpha_{np}\gamma_2 + \beta_n = \eta^{\frac{n}{2}}\gamma_2, \quad \beta^*_{np}\gamma_2 + \alpha^*_n = \eta^{\frac{n}{2}} \tag{A19}$$

and, therefore, $\langle \Psi_n | \mathcal{T}_m(w_1, \overline{w}_1) \overline{\mathcal{T}}_m(w_2, \overline{w}_2) | \Psi_n \rangle = (\frac{2\pi}{L})^{4h} \frac{1}{\eta^{2nh}} \frac{1}{(2 \sin \frac{\pi j}{q})^{4h}}$, based on which one can find that

$$\begin{aligned} S_A^{(m)}(n) - S_A^{(m)}(0) &= -\frac{c}{12} \frac{1+m}{m} n \log \frac{1}{\eta}, \\ S_A(n) - S_A(0) &= -\frac{c}{6} n \log \frac{1}{\eta}, \end{aligned} \tag{A20}$$

where $0 < \eta < 1$. Recalling that the total driving step number is $N = np$, we can write the entanglement entropy evolution in terms of the Lyapunov exponent in Eq. (60) as follows:

$$S_A(n) - S_A(0) = -\frac{c}{3} \lambda_L N. \tag{A21}$$

It is interesting to compare this formula with the result in Eq. (68). Here the linearly decreasing entanglement entropy is due to the coincidence of the entanglement cuts with the centers of the chiral energy-momentum density peaks (while keeping the antichiral modes undriven). During the driving, the degrees of freedom that entangle A and $\overline{A}$ will flow and accumulate at the energy-momentum density peaks, which are located at the entanglement cut. Intuitively, the Bell pairs that are nonlocal in space now become local, which results in a decrease in the entanglement entropy evolution.

It is emphasized that although the entanglement entropy decreases in time, which is due to the choice of entanglement cuts, the total energy of the system still grows in time (in the heating phase) in a periodically driven CFT.

c. Comparison of CFT and lattice calculations

To confirm the linearly decreasing feature of the entanglement entropy evolution in the previous subsections, we compare the CFT and lattice calculations in this Appendix. The results here are also related to the entanglement evolution at the nonheating fixed point in a Fibonacci driven CFT in Sec. V B 2 (see Fig. 22).

As an example, let us consider the minimal setup of periodically driven CFTs in Sec. IV D. We drive the CFT periodically with $H_{\theta=0}$ and H_θ in Eq. (71), with open boundary conditions. Now we consider two driving protocols:

$$\begin{aligned} &\text{Protocol I:} \quad \text{Driving with } H_0 \text{ first, and then } H_1 = H_\theta, \\ &\text{Protocol II:} \quad \text{Driving with } H_1 = H_\theta \text{ first, and then } H_0. \end{aligned} \tag{A22}$$

The driving time intervals are chosen as $T_0 = L/2$ for H_0, and $T_1 = L_{\text{eff}}/2$ for H_1, respectively. The resulting Möbius transformations in one driving period correspond to the following SU(1, 1) matrices:

$$\begin{aligned} \text{Protocol I:} \quad M &= M_0 M_\theta = \begin{pmatrix} -\cosh(2\theta) & \sinh(2\theta) \\ \sinh(2\theta) & -\cosh(2\theta) \end{pmatrix}, \\ \text{Protocol II:} \quad M' &= M_\theta M_0 = \begin{pmatrix} -\cosh(2\theta) & -\sinh(2\theta) \\ -\sinh(2\theta) & -\cosh(2\theta) \end{pmatrix}. \end{aligned} \tag{A23}$$

One can find $|\text{Tr}(M)| = |\text{Tr}(M')| = |2\cosh(2\theta)| > 2$, i.e., both M and M' are hyperbolic. Therefore, in both protocols, the CFT is in a heating phase. The difference is that, the chiral and antichiral energy-momentum density peaks are located separately at $x = 0$ and L in protocol I, but are located at the same position $x = L/2$ in protocol II, as pictorially shown as follows:

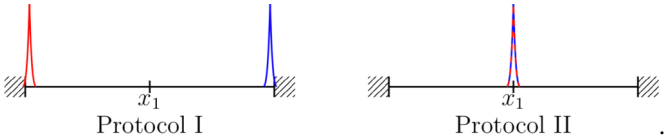

. (A24)

By choosing the subsystem $A = [0, x_1]$ with $x_1 = L/2$, the entanglement cut will not cut any peaks in protocol I, but will cut both the chiral and antichiral peaks in protocol II. Intuitively, one can unfold the CFT with open boundary conditions to a single copy of chiral CFT with a periodic boundary condition. After the unfolding, the entanglement cut in protocol II lies on the

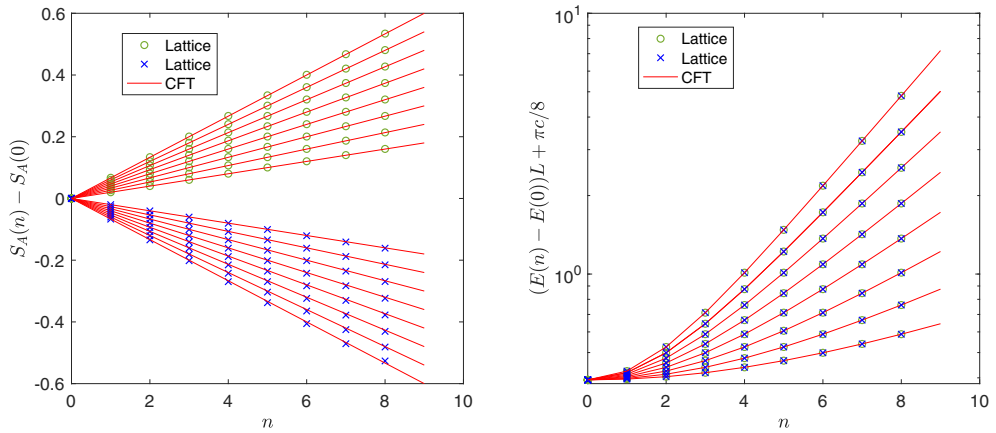

FIG. 38. Comparison of the CFT and lattice calculations on the entanglement entropy (left) and the total energy (right) evolution in the heating phase of a periodically driven CFT. The numerical data in ∘ (×) correspond to protocol I (II) in Eq. (A22). The CFT is periodically driven with H_0 and H_θ with time intervals $T_0 = L/2$ and $T_1 = L_{\text{eff}}/2$, respectively. From bottom to top (in the right plot), we choose $\theta = 0.03$, 0.04, 0.05, 0.06, 0.07, 0.08, 0.09, and 0.1. The CFT results are plotted according to Eqs. (A25) and (A26).

centers of two chiral energy-momentum density peaks. Based on our study in the previous subsection, the entanglement entropy will decrease linearly in this case. Next, we show this is indeed the case rigorously.

Based on Eqs. (31) and (33), one can obtain the entanglement entropy and total energy evolution as follows:

$$S_A(n) = \begin{cases} \frac{2nc}{3}\theta, & \text{protocol I} \\ -\frac{2nc}{3}\theta, & \text{protocol II} \end{cases} \tag{A25}$$

where $A = [0, L/2]$. One can find that the entanglement entropy grows (decreases) linearly as a function of n in protocol I (II). On the other hand, the total energy of the system grows in both protocols:

$$E(n) - E(0) + \frac{\pi c}{8L} = \frac{\pi c}{8L}\cosh(4n\theta), \quad \text{for both protocols I and II.} \tag{A26}$$

Now we compare the CFT and lattice calculations on the entanglement entropy and total energy evolution. The lattice model we consider is the same as that in Sec. IV D 2. That is, the two lattice Hamiltonians under consideration are $H_0 = \frac{1}{2}\sum_{i=1}^{L-1} c_i^\dagger c_{i+1} + \text{H.c.}$, and $H_\theta = \frac{1}{2}\sum_{i=1}^{L-1} f(i) c_i^\dagger c_{i+1} + \text{H.c.}$ where L is the total length of the lattice and $f(i) = 1 - \tanh(2\theta)\cos\frac{2\pi i}{L}$, with the initial state chosen as the ground state of H_0. The comparison is shown in Fig. 38. The agreement between CFT and lattice calculations is remarkable.

4. Phase diagrams from periodic to quasiperiodical driving

In this section, we present one more group of results on the evolution of phase diagrams as we use a periodical driving to approach the Fibonacci quasiperiodical driving limit, as shown in Figs. 39 and 40.

In Fig. 39, we consider a periodic driving with the sequence generated by finitely truncated Fibonacci bit string, i.e., $\{X_j\}$ with $\omega_n = F_{n-1}/F_n$. The two driving Hamiltonians are $H_{\theta=0}$ and $H_{\theta=0.2}$ (see Sec.V A 2 for more details).

In Fig. 40, we replot the phase diagrams in Fig. 39 with the new variables as defined in Eq. (116). Based on Fig. 40, we obtain the measure of nonheating phases in Fig. 17.

APPENDIX B: FIBONACCI BIT STRING AND WORD AND RECURRENCE RELATION

In this Appendix, we review some basics of the Fibonacci bit string or word (in this paper, we will call it Fibonacci bit string instead of Fibonacci word)[28] for the readers' convenience. In particular, we explain the equivalence of two ways to generate the Fibonacci bit string: (1) the quasiperiodic potential and (2) the substitution rule. Based on the substitution rule, we explain the recurrence relation of the traces and the constant of motion that are used in the main text.

1. Substitution rule for Fibonacci bit string

In the main text, we generate the Fibonacci quasiperiodic driving using the following bit string ("Fibonacci bit string"):

$$X_j = \chi((j-1)\omega), \quad j = 1, 2, 3 \ldots \tag{B1}$$

[28]The term "Fibonacci word" was used in combinatorics, whose definition is off by an overall bit flipping $0 \leftrightarrow 1$ comparing to the one commonly used in the Fibonacci quasicrystal literature. We adopt the latter convention, and rename it as Fibonacci bit string to avoid confusion.

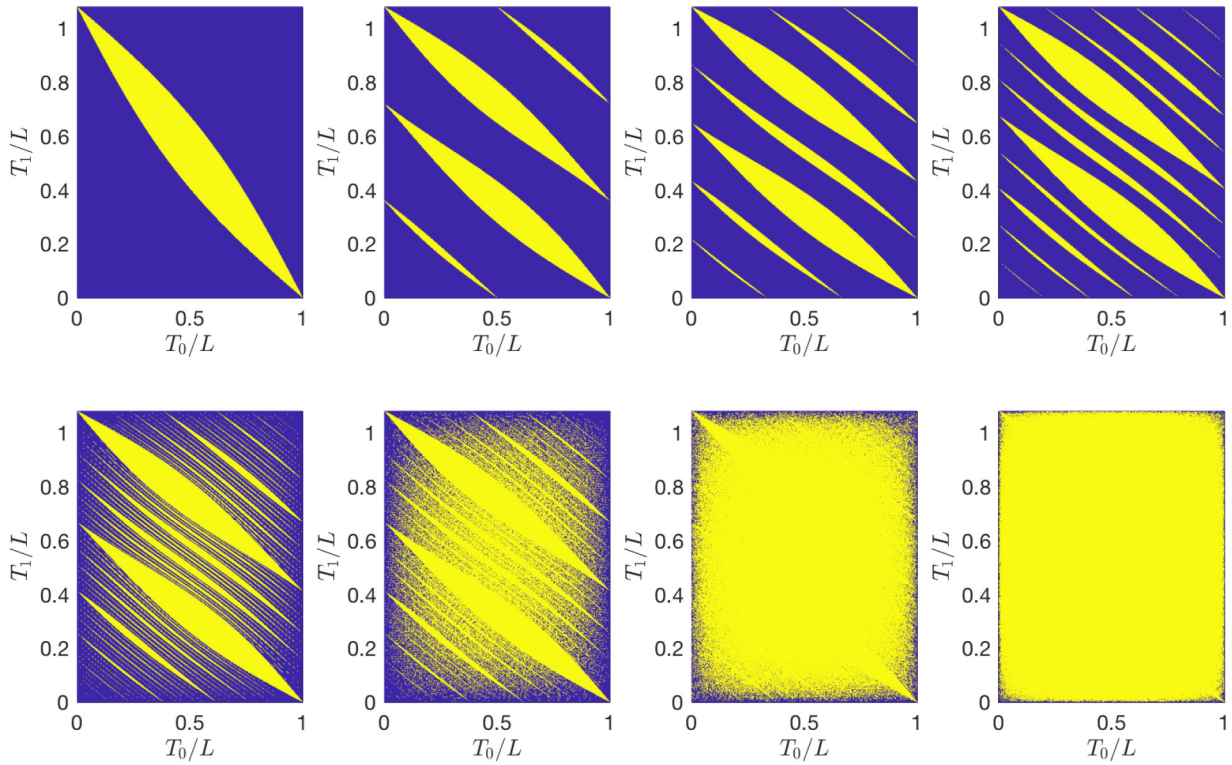

FIG. 39. Phase diagrams in a periodically driven CFT with the sequence generated by finitely truncated Fibonacci bit string, i.e., $\{X_j\}$ with $\omega_n = F_{n-1}/F_n$. Here we choose $n = 2$, 4, 5, 6, 10, 20, 100, and 1000, respectively. The two Hamiltonians we use are $H_0(\theta = 0)$ and $H_1(\theta = 0.2)$ in (71). The phase diagram is periodic in T_0 direction with period L and in T_1 direction with period $L\ \cosh(2\theta) \simeq 1.08L$. The blue (yellow) regions correspond to the heating (nonheating) phases.

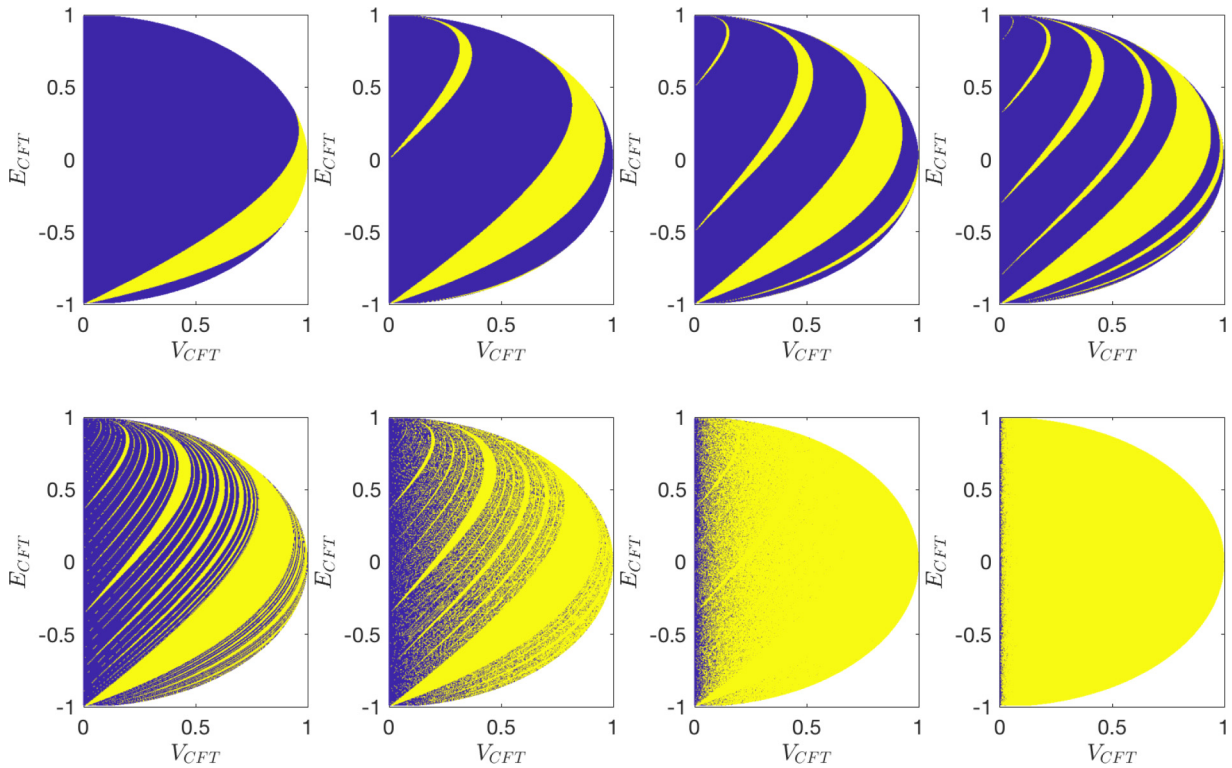

FIG. 40. Phase diagrams in a periodically driven CFT with the sequence generated by finitely truncated Fibonacci bit string, i.e., $\{X_j\}$ with $\omega_n = F_{n-1}/F_n$. Here we choose $n = 2$, 4, 5, 6, 10, 20, 100, and 1000, respectively. The two Hamiltonians we use are $H_0(\theta = 0)$ and $H_1(\theta = 0.2)$ in (71). The phase diagram is periodic in T_0 direction with period L and in T_1 direction with period $L\ \cosh(2\theta) \simeq 1.08L$. The blue (yellow) regions correspond to the heating (nonheating) phases.

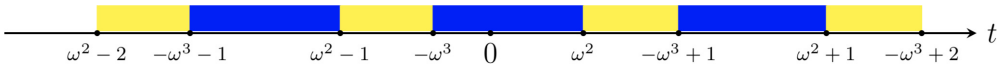

FIG. 41. An illustration for the characteristic function $\chi(t)$ for the Fibonacci sequence. The blue regime stands for value 1 and the yellow for 0.

where $\chi(t) = \chi(t+1)$ is a period-1 characteristic function

$$\chi(t) = \begin{cases} 1, & -\omega^3 \leqslant t < \omega^2 \\ 0, & \omega^2 \leqslant t < 1-\omega^3 \end{cases} \tag{B2}$$

and $\omega = \frac{\sqrt{5}-1}{2}$ is the inverse of golden ratio [see Fig. 41 for an illustration of function $\chi(t)$]. For instance, the first few bits of $\{X_j\}$ are given as follows:

$$X_{j=1,2,3\ldots} = 10110101\ldots. \tag{B3}$$

This definition is straightforward but not useful in our application. Instead, we will follow the presentation in Ref. [89] to show that the above bit string can be generated by a substitution rule. The equivalence is based on the following two properties of $\{X_j\}$:

(1) Let us use the notation "$\lfloor x \rfloor := \max\{m \in \mathbb{Z} | m \leqslant x\}$" for the floor function, and we have

$$X_j = \lfloor (j+1)\omega \rfloor - \lfloor j\omega \rfloor. \tag{B4}$$

To prove this statement, let us first use the relation $\omega^2 + \omega - 1 = 0$ to rewrite $\omega^2 = 1-\omega$ and $-\omega^3 = 1-2\omega$. Then, according to the rule (B2) we have

$$X_j = 1 \Leftrightarrow \exists m \in \mathbb{Z} \ : \ m - 2\omega \leqslant (j-1)\omega < m - \omega \Leftrightarrow \exists m \in \mathbb{Z} \ : \ j\omega < m \leqslant (j+1)\omega. \tag{B5}$$

(2) Let us use F_n to denote the nth Fibonacci number, namely, $F_n = F_{n-1} + F_{n-2}$ with $F_0 = F_1 = 1$, then we have

$$X_{j+F_n} = X_j\,, \quad \text{for } n \geqslant 2\,,\ 1 \leqslant j < F_n. \tag{B6}$$

To prove this statement, it is sufficient to show that for $n \geqslant 2$, the difference of two parts in $X_j = \lfloor (j+1)\omega \rfloor - \lfloor j\omega \rfloor$ is unchanged while shifting the argument of the floor function $\lfloor \cdot \rfloor$ by $F_n\omega$ for $1 \leqslant j < F_n$: we can write $F_n\omega = m + r$ where m is the integer that is closest to $F_n\omega$ and $|r| = \mathrm{dist}(F_n\omega, \mathbb{Z})$ denotes the distance (with sign) between $F_n\omega$ and the nearest integer m. Obviously, shifting by an integer will not affect the difference, so we only need to check the effect of shifting by r. From the fact that the convergent[29] F_{n-1}/F_n is a best Diophantine approximation[30] of the irrational number ω, we have the following inequality:

$$|r| = \mathrm{dist}(F_n\omega, \mathbb{Z}) < \mathrm{dist}(j\omega, \mathbb{Z}) \quad \text{for} \quad 1 \leqslant j < F_n, \tag{B7}$$

in other words, for $j\omega$ with $1 \leqslant j < F_n$, adding r will not be able to fill the gap between $j\omega$ and a nearby integer. This statement further holds for $j = F_n$ since ω is irrational, $F_n\omega + r$ can not be an integer. To summarize, neither $\lfloor (j+1)\omega \rfloor$ nor $\lfloor j\omega \rfloor$ will change its value after a shift of r for $1 \leqslant j < F_n$ and therefore we have proved (B6).

The second property (B6) provides an efficient algorithm to generator the 0,1 bit string for $\{X_j\}$. For instance, let us denote the first F_n bits as string A_nB_n where A_n stands for the first F_{n-1} bits and B_n stands for the next F_{n-2}, and they together have length $F_n = F_{n-1} + F_{n-2}$ as required, here are examples for first few n:

$$F_3 = 3: \ \underbrace{10}_{A_3}\underbrace{1}_{B_3}, \quad F_4 = 5: \ \underbrace{101}_{A_4}\underbrace{10}_{B_4}, \quad F_5 = 8: \ \underbrace{10110}_{A_5}\underbrace{101}_{B_5}. \tag{B8}$$

[29] For irrational real number x, we always have an infinite continued fraction representation

$$x = a_0 + \cfrac{1}{a_1 + \cfrac{1}{a_2 + \ldots \cfrac{1}{a_n + \ldots}}}, \quad a_0 \in \mathbb{Z}\,, \quad a_{j\geqslant 1} \in \mathbb{Z}^{>0}.$$

The nth *principal convergent* is the rational number p_n/q_n obtained by a truncation at a_n. The irrational number $\omega = \frac{\sqrt{5}-1}{2}$ has a particularly simple continued fraction representation $a_0 = 0$, $a_1 = a_2 = \cdots = 1$, and its finite truncation is the ratio of two nearby Fibonacci numbers F_{n-1}/F_n as one can easily check.

[30] For a real number x, a rational number p/q is a best approximation (of second kind) if

$$|qx - p| < |q'x - p'|, \quad \forall\, q > q' > 0\,.$$

For the proof that the best approximations are given by the convergent, see, e.g.. Ref. [90].

Then, we group the string A_nB_n, rename it as $A_{n+1} = A_nB_n$, and according to (B6), the B_{n+1} is obtained by copying the first F_{n-1} bits of A_{n+1} which is exactly A_n, i.e., we have the following recurrence relation:

$$A_{n+1} = A_nB_n, \quad B_{n+1} = A_n. \tag{B9}$$

One may be concerned that (B6) actually produces a longer bit string than the above recurrence relation since it also generates an additional segment B_n after $A_{n+1}B_{n+1}$ which will overlap the first F_{n-2} bits of B_{n+2}. One can check that the overlapping part is consistent with the rule here because the first F_{n-2} bits of B_{n+2} are indeed $A_{n-1} = B_n$.

A final comment is that the above recurrence relation can be recast into a "local" substitution rule that is closer to the rabbit populations problem Fibonacci originally considered. Let us start with a single bit 1, and apply the following substitution rule:

$$1 \to 10\,, \quad 0 \to 1 \tag{B10}$$

at each step, then we will generate the sequence

$$1 \to 10 \to 101 \to 10110 \to 10110101 \to \cdots \tag{B11}$$

which approaches to the Fibonacci bit string after infinite steps.

2. Recurrence relation and constant of motion

In the main text, we are interested in the product Π_n of n SU(1, 1) matrices

$$\Pi_n = M_1M_2 \ldots M_n, \tag{B12}$$

where matrix M_j depends on X_j in the Fibonacci bit string. The substitution rule (B9) directly leads to the following recurrence relation for Π_n:

$$\Pi_{F_k} = \Pi_{F_{k-1}}\Pi_{F_{k-2}},, \quad \forall\, k \geqslant 3. \tag{B13}$$

The relation can be extended to $k = 2$ by defining an auxiliary $\Pi_{F_0} = M_2$ that is distinct from $\Pi_{F_1} = M_1$, although strictly speaking $F_0 = F_1 = 1$. A key observation made in Ref. [68] is that their traces obey the following recurrence relation:

$$\boxed{x_{F_{k+1}} = 2x_{F_k}x_{F_{k-1}} - x_{F_{k-2}}, \quad \text{where} \quad x_{F_k} = \tfrac{1}{2}\,\mathrm{Tr}(\Pi_{F_k}) = \tfrac{1}{2}\,\mathrm{Tr}\left(\Pi_{F_k}^{-1}\right).} \tag{B14}$$

To derive this relation, we start with (B13) and find

$$\Pi_{F_{k+1}} + \Pi_{F_{k-2}}^{-1} = \Pi_{F_k}\Pi_{F_{k-1}} + \Pi_{F_k}^{-1}\Pi_{F_{k-1}}. \tag{B15}$$

Then, we insert identity $\Pi_{F_k} + \Pi_{F_k}^{-1} = \mathrm{Tr}(\Pi_{F_k})\mathbb{I}$ for the unideterminant 2×2 matrix Π_{F_k}, and obtain

$$\Pi_{F_{k+1}} + \Pi_{F_{k-2}}^{-1} = \mathrm{Tr}(\Pi_{F_k})\Pi_{F_{k-1}}, \tag{B16}$$

whose trace gives (B14).

Using the trace relation, Ref. [68] further notes a constant of motion

$$\boxed{I = -1 + x_{F_k}^2 + x_{F_{k-1}}^2 + x_{F_{k-2}}^2 - 2x_{F_k}x_{F_{k-1}}x_{F_{k-2}}.} \tag{B17}$$

Indeed, one can check that the change of the right-hand side (r.h.s.) under the shifting $k \to k + 1$ is zero:

$$\begin{aligned} \Delta\text{r.h.s.} &= x_{F_{k+1}}^2 - x_{F_{k-2}}^2 - 2\left(x_{F_{k+1}} - x_{F_{k-2}}\right)x_{F_k}x_{F_{k-1}} \\ &= \left(x_{F_{k+1}} - x_{F_{k-2}}\right)\left(x_{F_{k+1}} + x_{F_{k-2}} - 2x_{F_k}x_{F_{k-1}}\right) = 0. \end{aligned} \tag{B18}$$

[1] L. Jiang, T. Kitagawa, J. Alicea, A. R. Akhmerov, D. Pekker, G. Refael, J. I. Cirac, E. Demler, M. D. Lukin, and P. Zoller, Majorana Fermions in Equilibrium and Driven Cold Atom Quantum Wires, Phys. Rev. Lett. **106**, 220402 (2011).

[2] T. Oka and H. Aoki, Photovoltaic hall effect in graphene, Phys. Rev. B **79**, 081406(R) (2009).

[3] T. Kitagawa, E. Berg, M. Rudner, and E. Demler, Topological characterization of periodically driven quantum systems, Phys. Rev. B **82**, 235114 (2010).

[4] M. S. Rudner, N. H. Lindner, E. Berg, and M. Levin, Anomalous Edge States and the Bulk-Edge Correspondence for Periodically Driven Two-Dimensional Systems, Phys. Rev. X **3**, 031005 (2013).

[5] D. V. Else and C. Nayak, Classification of topological phases in periodically driven interacting systems, Phys. Rev. B **93**, 201103(R) (2016).

[6] A. C. Potter, T. Morimoto, and A. Vishwanath, Classification of Interacting Topological Floquet Phases in One Dimension, Phys. Rev. X **6**, 041001 (2016).

[7] R. Roy and F. Harper, Abelian floquet symmetry-protected topological phases in one dimension, Phys. Rev. B **94**, 125105 (2016).

[8] H. C. Po, L. Fidkowski, T. Morimoto, A. C. Potter, and A. Vishwanath, Chiral Floquet Phases of Many-Body Localized Bosons, Phys. Rev. X **6**, 041070 (2016).

[9] R. Roy and F. Harper, Periodic table for floquet topological insulators, Phys. Rev. B **96**, 155118 (2017).

[10] F. Harper and R. Roy, Floquet Topological Order in Interacting Systems of Bosons and Fermions, Phys. Rev. Lett. **118**, 115301 (2017).

[11] H. C. Po, L. Fidkowski, A. Vishwanath, and A. C. Potter, Radical chiral floquet phases in a periodically

driven kitaev model and beyond, Phys. Rev. B **96**, 245116 (2017).
[12] I.-D. Potirniche, A. C. Potter, M. Schleier-Smith, A. Vishwanath, and N. Y. Yao, Floquet Symmetry-Protected Topological Phases in Cold-Atom Systems, Phys. Rev. Lett. **119**, 123601 (2017).
[13] T. Morimoto, H. C. Po, and A. Vishwanath, Floquet topological phases protected by time glide symmetry, Phys. Rev. B **95**, 195155 (2017).
[14] L. Fidkowski, H. C. Po, A. C. Potter, and A. Vishwanath, Interacting invariants for floquet phases of fermions in two dimensions, Phys. Rev. B **99**, 085115 (2019).
[15] V. Khemani, A. Lazarides, R. Moessner, and S. L. Sondhi, Phase Structure of Driven Quantum Systems, Phys. Rev. Lett. **116**, 250401 (2016).
[16] D. V. Else, B. Bauer, and C. Nayak, Floquet Time Crystals, Phys. Rev. Lett. **117**, 090402 (2016).
[17] C. W. von Keyserlingk and S. L. Sondhi, Phase structure of one-dimensional interacting floquet systems. i. abelian symmetry-protected topological phases, Phys. Rev. B **93**, 245145 (2016).
[18] C. W. von Keyserlingk and S. L. Sondhi, Phase structure of one-dimensional interacting floquet systems. ii. symmetry-broken phases, Phys. Rev. B **93**, 245146 (2016).
[19] D. V. Else, B. Bauer, and C. Nayak, Prethermal Phases of Matter Protected by Time-Translation Symmetry, Phys. Rev. X **7**, 011026 (2017).
[20] N. Y. Yao, A. C. Potter, I.-D. Potirniche, and A. Vishwanath, Discrete Time Crystals: Rigidity, Criticality, and Realizations, Phys. Rev. Lett. **118**, 030401 (2017).
[21] S. Choi, J. Choi, R. Landig, G. Kucsko, H. Zhou, J. Isoya, F. Jelezko, S. Onoda, H. Sumiya, V. Khemani *et al.*, Observation of discrete time-crystalline order in a disordered dipolar many-body system, Nature (London) **543**, 221 (2017).
[22] J. Zhang, P. W. Hess, A. Kyprianidis, P. Becker, A. Lee, J. Smith, G. Pagano, I.-D. Potirniche, A. C. Potter, A. Vishwanath *et al.*, Observation of a discrete time crystal, Nature (London) **543**, 217 (2017).
[23] N. Y. Yao, C. Nayak, L. Balents, and M. P. Zaletel, Classical Discrete Time Crystals, Nat. Phys. **16**, 438 (2020).
[24] L. D'Alessio and M. Rigol, Long-time Behavior of Isolated Periodically Driven Interacting Lattice Systems, Phys. Rev. X **4**, 041048 (2014).
[25] P. Ponte, Z. Papić, F. Huveneers, and D. A. Abanin, Many-Body Localization in Periodically Driven Systems, Phys. Rev. Lett. **114**, 140401 (2015).
[26] D. A. Abanin, W. De Roeck, and F. Huveneers, Theory of many-body localization in periodically driven systems, Ann. Phys. **372**, 1 (2016).
[27] D. A. Abanin, W. De Roeck, and F. Huveneers, Exponentially Slow Heating in Periodically Driven Many-Body Systems, Phys. Rev. Lett. **115**, 256803 (2015).
[28] D. Abanin, W. De Roeck, W. W. Ho, and F. Huveneers, A Rigorous Theory of Many-Body Prethermalization for Periodically Driven and Closed Quantum Systems, Commun. Math. Phys. **354**, 809 (2017).
[29] D. A. Abanin, W. De Roeck, W. W. Ho, and F. Huveneers, Effective Hamiltonians, prethermalization, and slow energy absorption in periodically driven many-body systems, Phys. Rev. B **95**, 014112 (2017).
[30] M. Sato, S. Takayoshi, and T. Oka, Laser-Driven Multiferroics and Ultrafast Spin Current Generation, Phys. Rev. Lett. **117**, 147202 (2016).
[31] D. H. Dunlap and V. M. Kenkre, Dynamic localization of a charged particle moving under the influence of an electric field, Phys. Rev. B **34**, 3625 (1986).
[32] F. Grossmann, T. Dittrich, P. Jung, and P. Hänggi, Coherent Destruction of Tunneling, Phys. Rev. Lett. **67**, 516 (1991).
[33] C. K. Law, Resonance Response of the Quantum Vacuum to an Oscillating Boundary, Phys. Rev. Lett. **73**, 1931 (1994).
[34] V. V. Dodonov and A. B. Klimov, Generation and detection of photons in a cavity with a resonantly oscillating boundary, Phys. Rev. A **53**, 2664 (1996).
[35] I. Martin, Floquet dynamics of classical and quantum cavity fields, Ann. Phys. **405**, 101 (2019).
[36] A. Eckardt, Colloquium: Atomic quantum gases in periodically driven optical lattices, Rev. Mod. Phys. **89**, 011004 (2017).
[37] A. A. Belavin, A. M. Polyakov, and A. B. Zamolodchikov, Infinite conformal symmetry in two-dimensional quantum field theory, Nucl. Phys. B **241**, 333 (1984).
[38] P. Francesco, P. Mathieu, and D. Sénéchal, *Conformal Field Theory* (Springer, Berlin, 2012).
[39] P. Calabrese and J. Cardy, Evolution of entanglement entropy in one-dimensional systems, J. Stat. Mech. (2005) P04010.
[40] P. Calabrese and J. Cardy, Time Dependence of Correlation Functions Following a Quantum Quench, Phys. Rev. Lett. **96**, 136801 (2006).
[41] X. Wen and J.-Q. Wu, Floquet conformal field theory, arXiv:1805.00031.
[42] T. Hikihara and T. Nishino, Connecting distant ends of one-dimensional critical systems by a sine-square deformation, Phys. Rev. B **83**, 060414(R) (2011).
[43] I. Maruyama, H. Katsura, and T. Hikihara, Sine-square deformation of free fermion systems in one and higher dimensions, Phys. Rev. B **84**, 165132 (2011).
[44] H. Katsura, Sine-square deformation of solvable spin chains and conformal field theories, J. Phys. A: Math. Theor. **45**, 115003 (2012).
[45] N. Ishibashi and T. Tada, Infinite circumference limit of conformal field theory, J. Phys. A: Math. Theor. **48**, 315402 (2015).
[46] N. Ishibashi and T. Tada, Dipolar quantization and the infinite circumference limit of two-dimensional conformal field theories, Int. J. Mod. Phys. A **31**, 1650170 (2016).
[47] K. Okunishi, Sine-square deformation and Möbius quantization of 2D conformal field theory, Prog. Theor. Exp. Phys. **2016**, 063A02 (2016).
[48] X. Wen and J.-Q. Wu, Quantum dynamics in sine-square deformed conformal field theory: Quench from uniform to nonuniform conformal field theory, Phys. Rev. B **97**, 184309 (2018).
[49] X. Wen, S. Ryu, and A. W. W. Ludwig, Evolution operators in conformal field theories and conformal mappings: Entanglement Hamiltonian, the sine-square deformation, and others, Phys. Rev. B **93**, 235119 (2016).
[50] S. Tamura and H. Katsura, Zero-energy states in conformal field theory with sine-square deformation, Prog. Theor. Exp. Phys. **2017**, 113A01 (2017).
[51] T. Tada, Conformal Quantum Mechanics and Sine-Square Deformation, Prog. Theor. Exp. Phys. **2018**, 061B01 (2018).

[52] I. MacCormack, A. Liu, M. Nozaki, and S. Ryu, Holographic duals of inhomogeneous systems: the rainbow chain and the sine-square deformation model, J. Phys. A: Math. Theor. **52**, 505401 (2019).

[53] T. Tada, Time development of conformal field theories associated with l_1 and l_{-1} operators, J. Phys. A: Math. Theor. **53**, 25540 (2021).

[54] P. Caputa and I. MacCormack, Geometry and complexity of path integrals in inhomogeneous cfts, J. High Energ. Phys. 01 (2021) 027.

[55] X. Liu and T. Tada, Analysis for Lorentzian conformal field theories through sine-square deformation, Prog. Theor. Exp. Phys. **2020**, 061B01 (2020).

[56] R. Fan, Y. Gu, A. Vishwanath, and X. Wen, Emergent Spatial Structure and Entanglement Localization in Floquet Conformal Field Theory, Phys. Rev. X **10**, 031036 (2020).

[57] B. Lapierre, K. Choo, C. Tauber, A. Tiwari, T. Neupert, and R. Chitra, Emergent black hole dynamics in critical floquet systems, Phys. Rev. Res. **2**, 023085 (2020).

[58] P. T. Dumitrescu, R. Vasseur, and A. C. Potter, Logarithmically Slow Relaxation in Quasiperiodically Driven Random Spin Chains, Phys. Rev. Lett. **120**, 070602 (2018).

[59] H. Zhao, F. Mintert, and J. Knolle, Floquet time spirals and stable discrete-time quasicrystals in quasiperiodically driven quantum many-body systems, Phys. Rev. B **100**, 134302 (2019).

[60] D. V. Else, W. W. Ho, and P. T. Dumitrescu, Long-Lived Interacting Phases of Matter Protected by Multiple Time-Translation Symmetries in Quasiperiodically Driven Systems, Phys. Rev. X **10**, 021032 (2020).

[61] D. R. Hofstadter, Energy levels and wave functions of Bloch electrons in rational and irrational magnetic fields, Phys. Rev. B **14**, 2239 (1976).

[62] X. Wen, R. Fan, Y. Gu, and A. Vishwanath (unpublished).

[63] R. Fan, X. Wen, Y. Gu, and A. Vishwanath (unpublished).

[64] E. Witten, Coadjoint orbits of the virasoro group, Commun. Math. Phys. **114**, 1 (1988).

[65] B. Han (unpublished).

[66] B. Han and X. Wen, Classification of sl_2 deformed floquet conformal field theories, Phys. Rev. B **102**, 205125 (2020).

[67] D. Damanik, Schrödinger operators with dynamically defined potentials, Ergodic Theory Dynam. Syst. **37**, 1681 (2017).

[68] M. Kohmoto, L. P. Kadanoff, and C. Tang, Localization Problem in One Dimension: Mapping and Escape, Phys. Rev. Lett. **50**, 1870 (1983).

[69] S. Ostlund, R. Pandit, D. Rand, H. J. Schellnhuber, and E. D. Siggia, One-Dimensional Schrödinger Equation with an Almost Periodic Potential, Phys. Rev. Lett. **50**, 1873 (1983).

[70] A. Sütő, Singular continuous spectrum on a cantor set of zero lebesgue measure for the fibonacci hamiltonian, J. Stat. Phys. **56**, 525 (1989).

[71] M. Viana, *Lectures on Lyapunov Exponents*, Vol. 145 (Cambridge University Press, Cambridge, 2014).

[72] D. Damanik, A. Gorodetski, and W. Yessen, The fibonacci Hamiltonian, Inventiones Mathematicae **206**, 629 (2016).

[73] M. Casdagli, Symbolic dynamics for the renormalization map of a quasiperiodic schrödinger equation, Commun. Math. Phys. **107**, 295 (1986).

[74] M. Kohmoto, B. Sutherland, and C. Tang, Critical wave functions and a cantor-set spectrum of a one-dimensional quasicrystal model, Phys. Rev. B **35**, 1020 (1987).

[75] B. Sutherland and M. Kohmoto, Resistance of a one-dimensional quasicrystal: Power-law growth, Phys. Rev. B **36**, 5877 (1987).

[76] B. Iochum and D. Testard, Power law growth for the resistance in the fibonacci model, J. Stat. Phys. **65**, 715 (1991).

[77] B. Iochum, L. Raymond, and D. Testard, Resistance of one-dimensional quasicrystals, Phys. A (Amsterdam) **187**, 353 (1992).

[78] P. G. Harper, Single Band Motion of Conduction Electrons in a Uniform Magnetic Field, Proc. Phys. Soc. London, Sect. A **68**, 874 (1955).

[79] S. Aubry and G. André, Analyticity breaking and anderson localization in incommensurate lattices, Ann. Isr. Phys. Soc. **3**, 18 (1980).

[80] C. M. Soukoulis and E. N. Economou, Localization in One-Dimensional Lattices in the Presence of Incommensurate Potentials, Phys. Rev. Lett. **48**, 1043 (1982).

[81] B. Simon, Almost periodic Schrödinger operators: A review, Adv. Appl. Math. **3**, 463 (1982).

[82] R. Fan, Y. Gu, A. Vishwanath, and X. Wen, Floquet conformal field theories with generally deformed Hamiltonians, Sci. Post Phys. **10**, 049 (2021).

[83] B. Lapierre and P. Moosavi, A geometric approach to inhomogeneous floquet systems, arXiv:2010.11268.

[84] W. S. Bakr, J. I. Gillen, A. Peng, S. Fölling, and M. Greiner, A quantum gas microscope for detecting single atoms in a hubbard-regime optical lattice, Nature (London) **462**, 74 (2009).

[85] V. Borish, O. MarkoviÄ, J. Hines, S. Rajagopal, and M. Schleier-Smith, Transverse-Field Ising Dynamics in a Rydberg-Dressed Atomic Gas, Phys. Rev. Lett. **124**, 063601 (2020).

[86] H.-P. Breuer, F. Petruccione *et al.*, *The Theory of Open Quantum Systems* (Oxford University Press, Oxford, 2002).

[87] B. Lapierre, K. Choo, A. Tiwari, C. Tauber, T. Neupert, and R. Chitra, The fine structure of heating in a quasiperiodically driven critical quantum system, Phys. Rev. Res. **2**, 03346 (2020).

[88] B. Simon, *Orthogonal Polynomials on the Unit Circle* (American Mathematical Society, Providence, RI, 2005).

[89] A. Sütő, The spectrum of a quasiperiodic Schrödinger operator, Commun. Math. Phys. **111**, 409 (1987).

[90] S. Lang, *Introduction to Diophantine Approximations* (Springer, New York, 1995).